NTNU – Trondheim
Norwegian University of
Science and Technology

Ferroelectric Transitions in $Sr_xBa_{(1-x)}Nb_2O_6$

Effect of Thermal History on the Functional Properties

Trond Brandvik

Chemical Engineering and Biotechnology
Submission date: June 2015
Supervisor: Tor Grande, IMTE
Co-supervisor: Sverre Magnus Selbach, IMTE
Gerhard Henning Olsen, IMTE

Norwegian University of Science and Technology
Department of Materials Science and Engineering

Preface

This master thesis is written as a part of the Master program Chemical Engineering and Biotechnology at the Norwegian University of Science and Technology, NTNU. The work presented in this thesis has been carried out at the Department of Materials Science and Engineering, within the Inorganic Materials and Ceramic research group. Professor Tor Grande has been my supervisor, and associate professor Sverre Magnus Selbach and Ph.D. candidate Gerhard Henning Olsen have served as my co-supervisors. This thesis is a continuation of the specialization project *«Ferroelectric oxides with tetragonal tungsten bronze structure»* submitted by the author in December 2014 [1].

I would like to thank my supervisors for the help and guidance they have provided during this work. My main supervisor, Tor Grande, deserves thanks for giving me the opportunity to explore the subject of ferroelectric ceramics, and for always being a great motivation at our weekly meetings. Further, I would like to thank Gerhard Henning Olsen for useful discussions and input on ceramics in general and niobates in particular. Sverre Maguns Selbach deserves thanks for helping me with the simulations in Topas. I also owe a great thank you to the technical staff at the department for helping me with my experiments during this semester. Lastly, I would thank Ph.D. candidate Espen T. Wefring for helping me with the dielectric measurements in a rather busy period in the end of the semester.

Abbreviations has been introduced for convenient reasons throughout this text. Especially strontium barium niobate (SBN) and the tetragonal tungsten bronze (TTB) structure have been shortened on many occasions. The chemical formula for SBN, $\mathrm{Sr_xBa_{1-x}Nb_2O_6}$, is not the easiest one to neither write nor pronounce. It has therefore been shortened to SBNX, where the X-value gives the strontium content in percent.

Trondheim, June 8th 2015

Trond Brandvik

Abstract

Many functional materials used in today's electronic equipment have a high content lead [2]. Due to the environmental challenges related to production and usage of such materials, extensive research has been performed on lead-free alternatives [2,3]. Strontium barium niobate ($Sr_xBa_{1-x}Nb_2O_6$, SBNX) is one of many material systems suitable for replacing the lead-based materials. Functional properties and crystal structure of SBN has been investigated with respect to variations in thermal history. Samples of SBN30, SBN40 and SBN50 have been synthesized through the solid state route. Each composition has been heat treated for at least 12 hours at various temperatures, and subsequently characterized by powder X-ray diffraction (all compositions) and dielectric spectroscopy (only SBN40 and SBN50). The peak in dielectric permittivity is observed to shift towards lower temperatures for increased sintering temperature. For SBN40, the peak in dielectric permittivity shifted 100°C due to an increase in sintering temperature from 1300°C to 1400°C. A transition from normal ferroelectric to relaxor behavior has been observed as a result of increasing sintering temperature. For samples sintered at 1350°C and 1400°C, increasing frequency caused both a dispersion of measured permittivities and a shift towards higher temperatures for the peak in dielectric permittivity. The increasing sintering temperature also affected the crystal structure. Both unit cell parameters show temperature dependent behavior, causing the unit cell volume to decrease as the sintering temperature increases. The effect on the crystal structure from variations in thermal history is observed to be larger for samples with lower strontium content.

Sammendrag

Mange funksjonelle materialer som brukes i dagens elektronikk har et veldig høyt innhold av bly [2]. Av hensyn til miljøet er det blitt forsket mye på blyfrie alternativer som kan erstatte disse materialene [2, 3]. Strontium barium niobat ($Sr_xBa_{1-x}Nb_2O_6$, SBNX) er et av mange materialsystemer som har potensiale til å erstatte blyholdige materialer i slike applikasjoner. Funksjonelle egenskaper og krystallstruktur for SBN er blitt undersøkt som funksjon av økende varmebehandlingstemperatur. Prøver av SBN30, SBN40 og SBN50 har blitt syntetisert med fast stoff-metoden. Hver prøve har blitt varmebehandlet i minst 12 timer ved ulike temperaturer, og gjennomgått påfølgende karakterisering ved pulver røntgen diffraksjon (alle sammensetninger) og dielektrisk spektroskopi (kun SBN40 og SBN50). Toppen i dielektrisk permittivitet forflyttes mot lavere temperaturer for økende varmebehandlingstemperatur. For prøver av SBN40 ble det observert et skift for denne toppen på 100°C for en økning i varmebehandlingstemperatur fra 1300°C til 1400°C. For prøvene som ble varmebehandlet ved 1350°C og 1400°C ble det også observert relaxor-oppførsel. Økende frekvens forårsaket en spredning i den målte permittiviteten, samt at toppen flyttet seg mot høyere temperaturer. Økningen i varmebehandlingstemperatur påvirket også krystallstrukturen. Begge enhentscelleparametere viste temperaturavhengig oppførsel som resulterte i en reduksjon i enhentscellevolum som funksjon av økende varmebehandlingstemperatur. De observerte endringene i krystallstruktur er større for prøver med høyere barium-innhold.

Contents

Chapter 1

Introduction

1.1 Background

Ferroelectric materials have given rise to a wide range of applications within various industries, ever since the discovery of ferroelectricity in 1921 [4]. During the last century, the research on ferroelectric materials has steadily resulted in new materials and applications, e.g. high-dielectric-constant capacitors, piezoelectric sonars, ultrasonic transducers, thin-film capacitors and ferroelectric thin-film memories [4]. One of the leading choices of materials within commercial applications, like the production of transducers, are lead zirconate titanate (PZT) and lanthanum-modified lead zirconate titanate (PLZT) [4]. This is due to their superior properties regarding electrochemical coupling-coefficient, T_c-values and the wide range of dielectric constants, to name a few.

The main challenge with these materials is the high content of lead. The issues related to toxic emissions of lead both during production and waste handling, promote that some measures has to be taken. This is why the European Union has given directives imposing restrictions on the usage of lead-based materials in electronic equipment [2, 3]. However, some materials have been excluded from these directives, due to the lack of suitable replacement materials. PZT and other lead-containing ferroelectrics are some these materials. Research on lead-free replacements with adequate properties has therefore been given a lot of attention. There are several promising alternatives to the lead-based materials, where tetragonal tungsten bronzes in general and SBN in particular are good examples. There has been a significant research effort on the SBN over the last 50 years, resulting in a lot of different applications, including pyroelectric detectors and photorefractive devices [5–9]. However, despite all the research done on the tungsten bronzes, there are still aspects with these materials that are not sufficiently investigated yet. Especially the details related to the polarization mechanism are still not fully understood [10].

Lead metaniobate, ($Pb_5Nb_{10}O_{30}$ or PN), is another compound with TTB structure structure. Both SBN and PN are quite similar with respect to crystal structure and dielectric properties, but do have some fundamental differences. PN is build up by lead cations at the interstitial sites, while SBN has both strontium and barium at the same sites. As a result of the cationic differences, the polar direction of the two materials is different. The polar direction of PN is in-plane and perpendicular to the tetragonal axis, while the polar direction of SBN is parallel to the tetragonal axis [11]. Why there is such a significant difference between the two materials is not described adequately, but the 6*s* lone-pair of Pb^{2+} is suggested to have a central role [10, 11]. Details related to how the polarization in SBN occurs is therefore highly interesting in order to understand why the lead-based materials possess the good properties they do. In the present study the cation distribution in SBN has been investigated as a function of thermal history. The effect of increased disorder on functional properties has been studied in order to gain a greater understanding of the mechanisms related to cation movement in the structure.

1.2 Aim of this work

The aim of this Master's thesis has been to investigate the effect of the thermal history on functional properties of SBN. This has been done by studying the dielectric and crystallographic response, through dielectric spectroscopy and X-ray diffraction, as a function of composition and sintering temperature.

Chapter 2

Literature review

2.1 Definitions and concepts

2.1.1 Piezo- and ferroelectricity

The piezoelectric effect occurs when a material is exposed to external mechanical stress, causing surface charges to appear on both sides of the material [12, 13]. The surface charges are of opposite polarization, hence an electric field occurs across the material. The opposite effect occurs when the material is exposed to an electric field. The electric field causes the material to either expand or contract, depending on the field's direction [12, 13]. The former relation is referred to as the *direct piezoelectric effect*, while the latter is called the *converse piezoelectric effect* [12, 13]. The piezoelectric effect can arise in materials with a non-centrosymmetric unit cell, i.e. a unit cell without a center of inversion. Both effects are illustrated in Figure 2.1.

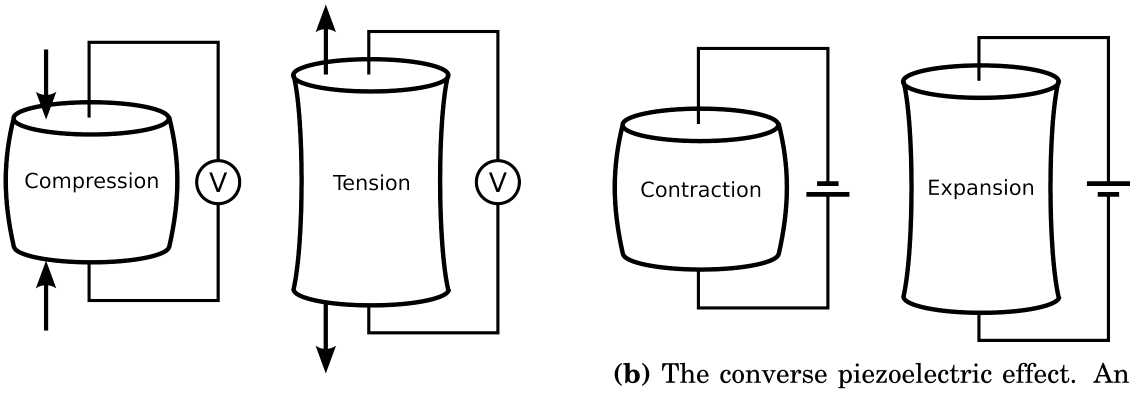

(a) The direct piezoelectric effect. When a piezoelectric material is subjected to compressive or tensile stress, an electric field occurs across the material.

(b) The converse piezoelectric effect. An applied electric field causes the piezoelectric material to contract or expand, depending on the fields direction.

Figure 2.1: A schematic illustration of the direct and converse piezoelectric effect.

A requirement for a unit cell to be able to accommodate piezoelectric properties, is to have a non-centrosymmetric symmetry. There are 32 crystallographic point groups, where 11 are centrosymmetric, leaving 21 non-centrosymmetric point groups. One of the 21 groups does however have an inversion center, causing it to lose its non-centrosymmetric nature. This leaves, in total, 20 non-centrosymmetric point groups possible to accommodate piezoelectric properties. A piezoelectric material is, in essence, a *dielectric* material showing piezoelectric behavior, as explained above. Dielectric materials are often characterized by their dielectric permittivity, which describes the material's resistance against polarization by an external electric field [12, 13]. As the dielectric permittivity of a material increases, the stronger electric fields is it able to withstand. If the external electric field becomes too high, the material will loose its dielectric properties. The dielectric permittivity is thus a measure of the strength of the dielectric material. The dielectric property is utilized in capacitors, where materials with high dielectric permittivity are used to increase the resistance against polarization [12]. An important feature with the dielectric permittivity is its behavior close to the ferro- to paraelectric phase transition temperature. The dielectric permittivity rises to a sharp peak in the vicinity of the Curie temperature [12]. As a result, the materials have very high dielectric permittivity close to the Curie temperature, often utilized in capacitors.

If a piezoelectric material also shows spontaneous polarization upon a change in temperature, it is said to be *pyroelectric* [12, 13]. A pyroelectric material changes its unit cell dimensions upon temperature change. This causes the unit cell to either expand or contract, inducing a temperature dependent polarization, hence the prefix *pyro*. The pyroelectric materials is a subgroup of the piezoelectric materials. This is due to the fact that, out of the 20 piezoelectric point groups, only 10 show spontaneous polarization upon temperature change [12]. A third class of materials, being a subgroup of dielectric, piezoelectric and pyroelectric materials, are the ferroelectric materials. A ferroelectric material is a material with spontaneous polarization, combined with the ability to switch the polarization's direction [12]. From an energy point of view is the ability to change the polarization's direction a result of a double energy well. The energy landscape has two local minimas corresponding to the two polar orientations, where the size of the energy barrier between the local minimas influences the robustness of the material. The higher the energy barrier is, the more energy must be applied to switch between the two orientations. For the material to lose its ferroelectric properties the ions must be able to overcome the energy barrier. If the temperature is raised to a level where the thermal energy approaches the size of the energy barrier, the ferroelectric material loses its ferroelectric property and becomes paraelectric. This temperature is called the *Curie temperature, T_c,* and is an important parameter of ferroelectric materials. The ability to customize the polarization's orientation is utilized in a variety of applications, e.g. high-dielectric constant capacitors, piezoelectric sonars and ferroelectric thin-film memories [4]. The relationship between dielectric, piezoelectric, pyroelectric and ferroelectric can be visualized as in Figure 2.2.

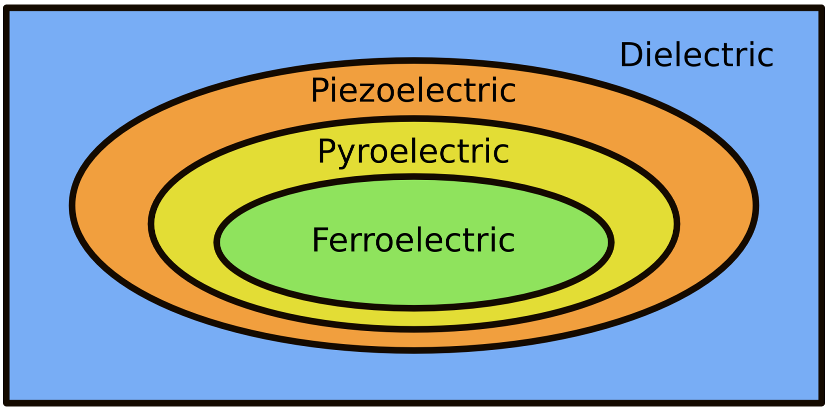

Figure 2.2: A Venn diagram illustrating the relationship between various types of dielectric materials. All ferroelectric materials are pyroelectric, but not all pyroelectric materials are ferroelectric. In the same way could the relationship between pyro-, piezo- and dielectric materials also be described based on this figure.

Features concerning the spontaneous polarization of a ferroelectric material are not constant, but dependent of both temperature and composition. The temperature dependency is related to the Curie temperature, while the compositional dependency will be discussed later. The Curie temperature is, as mentioned above, the temperature limit where the material undergoes a ferroelectric to paraelectric phase transition. At temperatures below T_c, the material is in its ferroelectric state, being able to retain the orientation of the ferroelectric domains. By increasing the temperature the thermal energy of the ions increase correspondingly, leading to a more randomized cation displacement. When the temperature approaches the Curie temperature, the net spontaneous polarization will decrease due to the increase of ionic thermal motion. When the Curie temperature is reached, the spontaneous polarization is abruptly lost. This is the point where thermal energy of the ions in the crystal overcomes the energy barrier separating the two polarization directions. The result is a net spontaneous polarization of zero, and thus the paraelectric temperature regime.

2.1.2 Ferroelectric domains

The dipoles in a ferroelectric material do not need to point in the same direction throughout the whole volume of the bulk material. There are normally smaller volumes within the material where all dipoles are parallel to each other, while possibly being non-parallel to the others. Such a volume is called a *ferroelectric domain*. Inside the domain, all dipoles are pointing in the same direction creating a local polarization across the domain volume. The domains are separated from each other by *domain walls*. These domain walls are not abrupt transitions from one polarization direction to another, but rather a gradual transition occurring over 0.5 – 1.0 nm [12]. Figure 2.3 schematically illustrates the change in polarization direction across a domain wall.

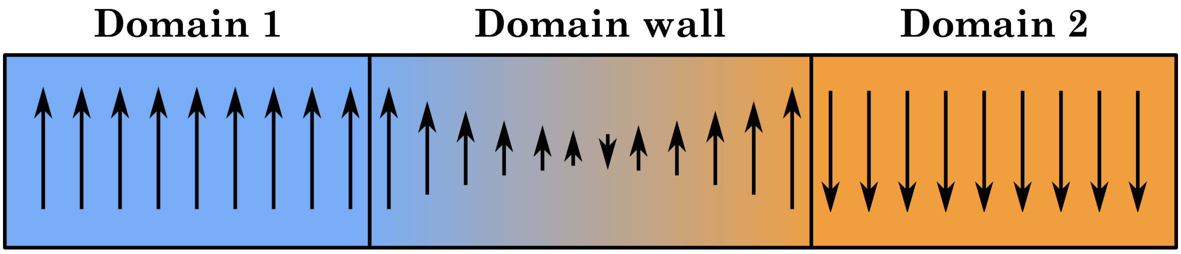

Figure 2.3: Illustration of the change in dipole direction in a domain wall between two adjoining domains with polar direction opposite of each other. The arrows indicate the direction and magnitude of the dipoles. There is no abrupt change between the two domains, but rather a gradually change over 0.5 – 1.0 nm [12].

If no precautions are taken the polar axes of the domains in a ceramic material will be randomly distributed in all directions. This causes the domains to cancel out each other's polarization, leaving the material with no net polarization. To be able to utilize the polarization in a ferroelectric material, the direction of the polarization must be aligned. The process of aligning ferroelectric domains is called *poling*. The ceramic material is heated to a temperature above the Curie temperature, making the local polarization susceptible for directional change. The material is now in its paraelectric state, where the thermal energy of the ions overcomes the energy barrier separating the polar directions. Subsequently, an electric field is applied across the material, forcing the polarization to shift in accordance to the field. To make sure the polarization remain in this arrangement, the electric field is kept constant while the material is cooled down below the Curie temperature. This causes the ordered polarization to freeze in, leaving a net polarization across the material. Figure 2.4 illustrates the difference between an unpoled and poled ceramic materials The unpoled materials in Figure 2.4a, has local polarization within domains that are more or less randomly oriented. After poling the domains will be in a more ordered state as visualized in Figure 2.4b.

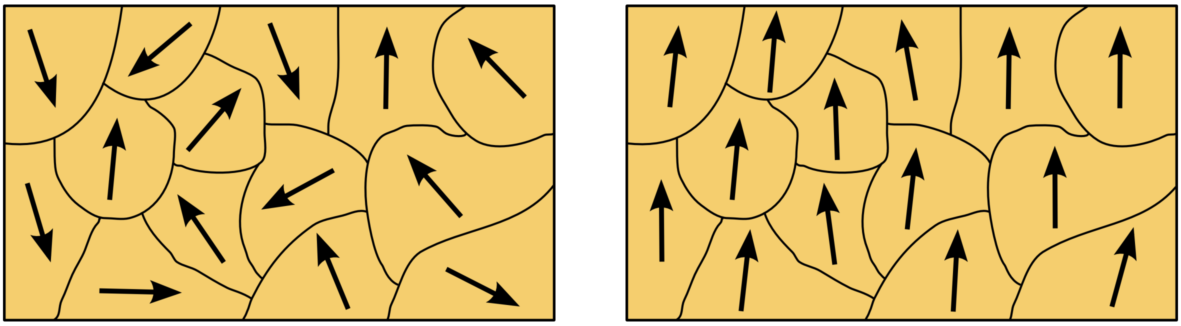

(a) Domains in an unpoled ceramic material. **(b)** Domains in a poled ceramic material.

Figure 2.4: Domain polarization in a ceramic material before and after poling. During poling, the polarization in each domain aligns with the applied electric field and is frozen in when the sample is cooled below T_c. The sum of the polarization for all domains makes up a measurable polarization across the ceramic sample.

2.1.3 Polarization mechanism

The spontaneous polarization in ferroelectric materials is usually a result of atom displacement from a symmetrical to a non-symmetrical environment. This displacement creates an internal dipole within the unit cell, summing to a net polarization in the bulk material [12]. The process of displacement can easily be illustrated by a two-dimensional model consisting of an array of anions with cations located in the center, as shown in Figure 2.5. When the cation is located in the center of the anionic array, the centrosymmetric arrangement prevents ferroelectric properties from occurring. Often, if relatively small cations are found in such anionic cages, the overall stability of the structure is increased by a small displacement of the cation towards one of the sides [12]. This displacement induces a distortion in the charge balance between the anions and the cation, thus creating a dipole. If the cation displacement takes place in all unit cells in the material, the sum of all dipole contributions could be measured as a net polarization in the bulk material.

2.1.4 Relaxor ferroelectrics

A subset of ferroelectric materials is relaxor ferroelectrics, henceforth denoted as relaxors. Relaxors is a class of disordered materials with interesting crystal structure

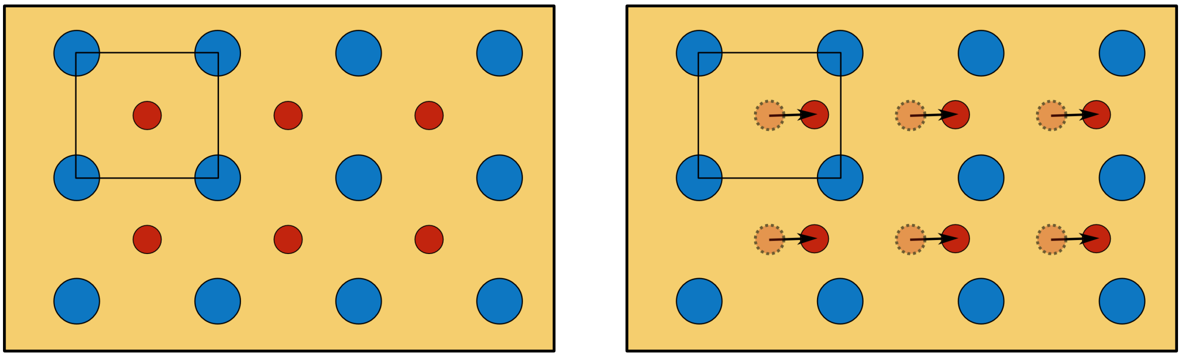

(a) An unpolar unit cell where the cations are positioned in the center of the anionic array.

(b) A polar unit cell where the cations are displaced from the center of the anionic array.

Figure 2.5: A schematic illustration of unit cell polarization by cation displacement. The unit cell is indicated by a black rectangle, with blue anions and red cations.

and properties. One of the main features of the relaxor materials is the broadened maximum peak in dielectric permittivity. The broadening indicates that the phase transition occurs over a temperature interval. As the peak increases in width, the transition is described as more and more diffuse, occurring over a temperature range referred to as the Curie range [14]. In contrast to the normal ferroelectrics where the peak is located at T_c, the relaxor peak is found at T_m. The nature of T_m differs from T_c due to its frequency dependency. The temperature limit for relaxors is decreasing as the frequency of the applied electric field decreases [15]. This is shown for SBN in Figure 2.6. Compared to normal ferroelectrics, relaxors are able to operate over a larger range of temperatures. This is due to the broadened peak in dielectric permittivity, and is utilized in applications like capacitors [16].

An essential structural characteristic of relaxors is the ability to introduce structural disorder in the crystal lattice. For this to occur, at least two ions must be able to occupy the same lattice site in the structure [15]. The bond length between a given cation and the surrounding anions would change as the cation is substituted. This will introduce disorder in the neighboring anion positions, and thus also distortions in the local structure close to the sites [15, 17]. This is well established for relaxor materials with perovskite structure [18]. For materials with tetragonal tungsten bronze structure, there is an additional condition which must be fulfilled in order for relaxor properties to occur [19]. According to results reported by Hornebecq *et al.* [19], the relaxor properties of TTBs are also dependent on the overall cation ratio of the A site cations. The choice between normal ferroelectric versus relaxor properties in a material with TTB structure could thus be made through the choice of overall sample composition. This is also the case for SBN. Lukasiewicz *et al.* [20] report a shift from normal ferroelectric to relaxor properties at 60% strontium content. The relaxor properties for SBN will be more thoroughly treated later.

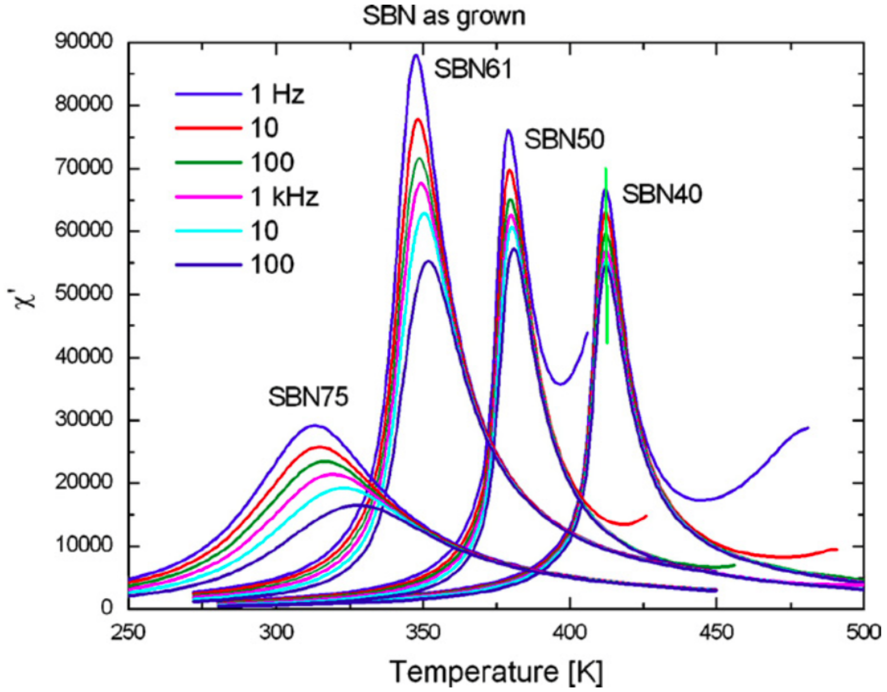

Figure 2.6: The dielectric susceptibility for SBN as a function of composition, temperature and frequency. The figure shows the pronounced relaxor properties for SBN at compositions above 60% strontium content. The figure is as reported by Lukasiewicz *et al.* [20].

Polar nanoregions

In conventional ferroelectrics, the maximum in dielectric permittivity corresponds to the phase transition between a non-polar paraelectric state and a long-range-ordered ferroelectric state. The polarization in the ferroelectric phase is homogeneous inside the macroscopic micrometer-sized domains. In relaxors, the long-range ordering are locally broken throughout the material due to nanometer sized domains, often called polar nanoregions [15].

Above T_c, in the paraelectric regime, there is no observable polarization for normal ferroelectrics. For relaxors, when cooled from the paraelectric regime, is it found that the dielectric permittivity begins to develop above T_m [21]. This development is found to be originating from the nanometer-sized regions arising during cooling. These polar nanoregions are ordered and give thus rise to a net polarization within the nanoregion. The size difference between the polar regions in normal ferroelectrics and relaxors are shown in Figure 2.7. The Burns temperature, T_d, lying far above T_c, is defined as the temperature limit for formation of the polar nanoregions. Upon cooling the polar nanoregions arising in the material break the paraelectric spatial symmetry of the overall structure [15]. The overall higher symmetry is however retained by the surrounding paraelectric phase [15]. In the absence of an external electric field, a random distribution of the nanoregions' polar orientation, hence also their dipole moment, occur. This causes the net polarization of the material to remain zero. Further cooling causes the polar nanoregions to grow and the overall dielectric permittivity to increase. Close to T_m, the polar nanoregions have become large enough to cause normal ferroelectric effect.

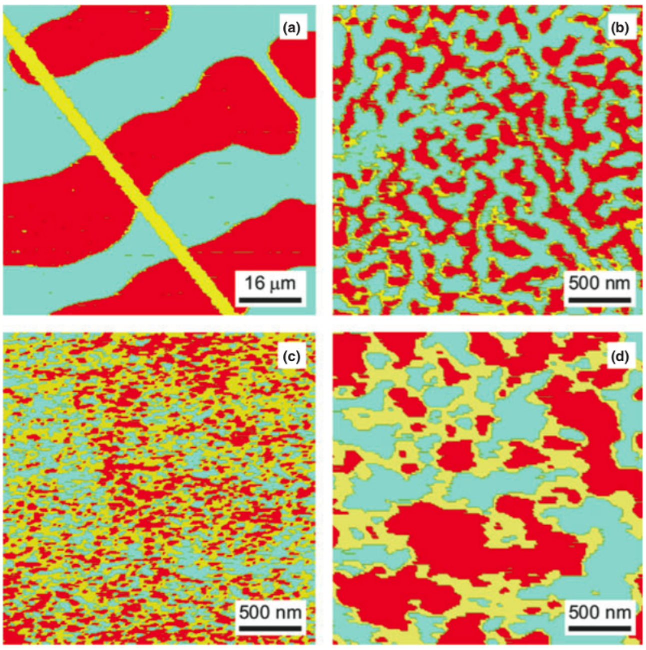

Figure 2.7: a) Ferroelectric domains in a single crystal of $PbTiO_3$ at room temperature. b) Polar structures in a relaxor ceramic below the transition temperature. c) Polar nanoregions in SBN single crystal above the transition temperature. d) Polar nanoregions in $BaTi_{0.85}Sn_{0.15}O_3$ ceramic above the transition temperature. The figure is shown as reported by Shvartsman and Lupascu [15].

Experimental evidence of the existence of polar nanoregions were first demonstrated by Burns and Dacol [21] in 1983. They showed that the refractive index of relaxors behaved differently compared to normal ferroelectrics. The refractive index was shown to be dependent on the square value of the dipole moments, and will not sum up to zero, even if the sum of all dipole moments does. As long as there are no dipoles present in the material the refractive index changes linearly with the temperature [15]. The presence of polar nanoregions will however create a deviation from linearity. In the paraelectric temperature regime above T_d, the refractive index show a linear temperature dependency for both normal ferroelectrics and relaxors. For normal ferroelectrics the linearity is retained down to the Curie temperature before deviations occur. For relaxors, however, these deviations occur at the Burns temperature, far above T_m, indicating that some polar regions exist in the structure, even above T_m [15, 18, 21].

2.2 Tungsten bronze materials

2.2.1 The tungsten bronze structure

The tungsten bronze structures are found in many different compounds, where niobates and tantalates have been throughly studied. Tungsten bronzes have the general structure A_xWO_3, with x being below 1 and with a great number of cations being able to enter the A and W sites. The introduction of niobium or tantalum at the tungsten sites maintain the bronze-like character of the compound, while the empty d orbitals of Nb^{5+} or Ta^{5+} introduce insulating properties. For this reason, compounds crystallizing in this structure are called bronzoïds or tungsten-bronze-type materials [11]. There are a few various tungsten bronze structures, and the type of structure being adopted depends largely on the cations entering the A site. The three most common structures are the perovskite, tetragonal and hexagonal tungsten bronze structures. Small cations like Li, Na or rare earth metals will cause the compound to crystallize into the perovskite tungsten bronze. Heavier elements like Pb, Sr and Ba cause the tetragonal structure to occur. The hexagonal tungsten bronze is formed by even heavier elements like K, Rb, Cs, In or Tl [11]. In addition to niobate and tantalum, there are a number of transition metals, like Ti or V, which can replace tungsten at its site.

The perovskite tungsten bronze structure resembles the pure perovskite structure in many ways, but differs by having only partial filling at the interstitial site. The perovskite tungsten bronze structure is built up by a regular network of corner-sharing WO_6-octahedra, where the octahedra are connected in all three crystallographic directions. Four corner-sharing octahedra constitute the perovskite cage where the A cation is found. Unlike the pure perovskite structure, the perovskite tungsten bronze structure only have partial occupancy at the interstitial sites. A complete filling of these perovskite cages is rarely observed [11].

The tetragonal tungsten bronze (TTB) structure is, compared to the perovskite tungsten bronze, a bit more complex. The structure is built up by two perovskite cages in addition to two WO_6-octahedra, where the octahedra are connected as shown in Figure 2.8. The structure has three types of interstitial positions; trigonal, quadratic and pentagonal, with a substantial difference in size. If the unit cell is tilted and examined along the [001] direction, the interstitial positions will reveal themselves as tunnels going through the crystal structure along the *c* axis. Due to the geometric difficulties arising from the way the octahedra are connected, distortions are introduced in some of the W-O bonds. This causes the pentagonal sites to deviate from ideality [11].

The common building block for all three tungsten bronze structures is the corner-sharing WO_6-octahedra. This is also the case for the hexagonal tungsten bronze structure. The octahedra are however connected in a different manner, giving a structure with three and six-membered rings. This arrangement does not require any distortion of the bonds, as for the tetragonal structure [11].

2.2.2 Strontium barium niobate

Strontium barium niobate (SBN) is a compound that exists in the solid solution area in the system of barium niobate and strontium niobate. SBN adopt the TTB structure and is ferroelectric at ambient temperatures with polar axis parallel to the *c* axis [5]. The compound is described by the formula $Sr_xBa_{1-x}Nb_2O_6$, where the x indicates the strontium content in the solid solution. Both in the literature and throughout this text strontium content is presented in the manner mentioned above. The strontium content can either be given as a decimal number, as in the formula, but most often in percentage. Hypothetically, it is possible for the strontium content to range from 0 to 1. This is however not possible if the TTB structure is to be maintained. The reported solubility limits vary from around 25-32% strontium content up to around 75-87% depending on the temperature [22, 23]. Beyond these limits there is a two-phase region where both SBN and one of the end phases co-exist.

Unit cell and unit cell parameters

SBN crystallizes in the tetragonal tungsten bronze structure. The crystal structure is visualized along the [001] direction in Figure 2.8 where the unit cell is delimited by a black square. The unit cell consists of five formula units yielding the total formula $Sr_{5x}Ba_{5(1-x)}Nb_{10}O_{30}$ [5]. From Figure 2.8 it can be seen that the unit cell has three types of interstitial sites, which are differentiated from each other by their geometric form and size. The sites are named as shown in Figure 2.8, and can be described by the formula $(A1)_2(A2)_4(C)_4(B)_{10}O_{30}$. In the center of the unit cell there is a quadratic A1 site surrounded by four NbO_6-octahedra, i.e. the perovskite cage. In addition there are 1/8 of a quadratic site at each corner of the three-dimensional unit cell, yielding a total of two A1 sites in the unit cell. The pentagonal sites are named A2 and the trigonal sites C, counting four sites in total of each type. The C site is however not large enough to accommodate either of the strontium or barium cations, and will remain empty for all compositions [11]. The size difference between A1 and A2 has a great influence on the cation distribution in the structure [24]. As mentioned above, several works report that barium cations are too big to fit into the A1 sites, leaving only strontium cations at these positions [24–27]. The A2 sites are filled with a mix of both strontium and barium. The strontium to barium ratio at the A2 sites is dependent of the overall composition of the material [24]. The constrains with respect to size leave the cations unequally distributed within the unit cell. There are six interstitial A sites in the unit cell, but only five A cations to allocate to these sites. As a result, there is a vacancy being distributed among the cations, creating partial vacancy at the sites. The compositional dependency of the cation distribution is illustrated in Figure 2.9. The figure shows a clear linear relationship between the sample composition, and the strontium and barium content at the A2 site. The strontium occupancy of the A1 site is however not showing any pronounced compositional dependency.

The tetragonal unit cell of SBN has equal values for the a and b parameter, while the c parameter is significantly smaller. Due to the equality of the a and b parameter the b parameter are often omitted when tetragonal unit cells are addressed. This is also the case for the tetragonal unit cell of SBN. Unit cell parameters have been reported by several works during the last 50 years, and some of them are presented in Figure 2.10. Podlozhenov *et al.* [24] report unit cell parameters for a range of compositions. These are highlighted by a trend line in the Figure 2.10. The rest of the values originate from a variety of sources where variations in synthesis routes may influence the final product and thus also the unit cell parameters. Jamieson, Ballmann & Brown,

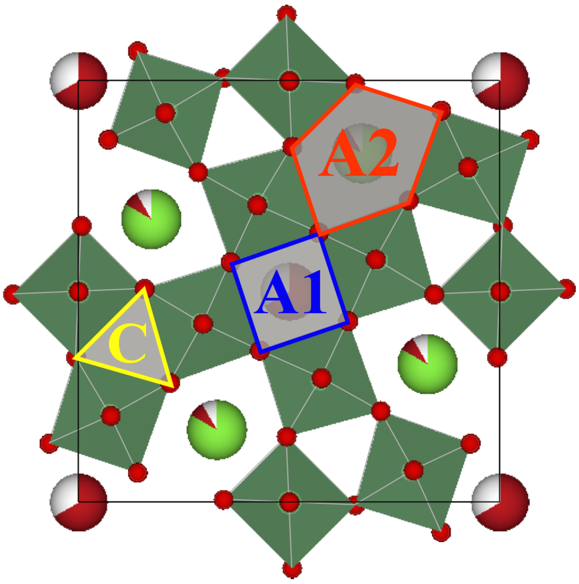

Figure 2.8: Interstitial sites in the tetragonal tungsten bronze structure for strontium barium niobate. The crystal structure is visualized along the *c* axis. The blue A1 sites are only filled with strontium ions. The orange, pentagonal A2 sites are accommodated by both strontium and barium ions, while the yellow, trigonal C sites are empty.

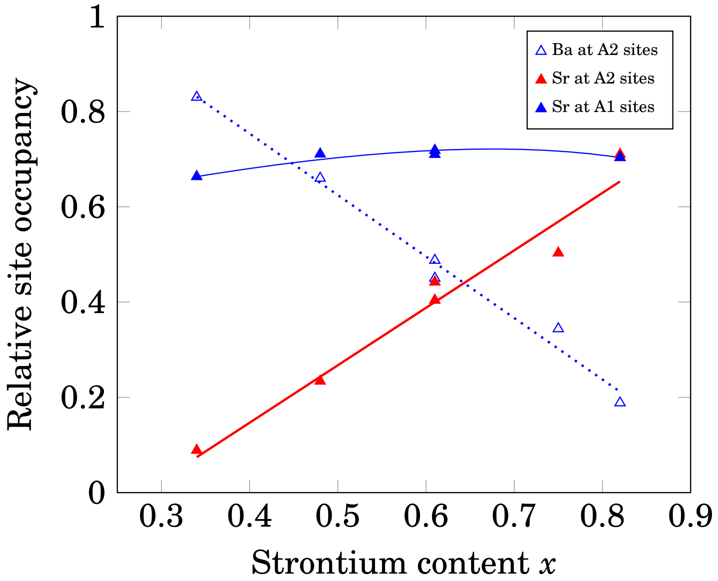

Figure 2.9: Relative site occupancies of strontium and barium at the A sites. The data is reported by Podlozhenov *et al.* [24], Jamieson *et al.* [5] and Woike *et al.* [27]. Linear trend lines are added for the strontium and barium occupancies at the A2 site, illustrating the pronounced linear relationship with the overall composition. The strontium occupancy at the A1 site is fitted with quadratic expression, and does not change significantly with the sample composition.

Podlozhenov *et al.*, Schefer *et al.* and Oliver & Neurgaonkar [5,24,26,28,29] have all used single crystals annealed at temperatures in the range of 1300-1400°C. Nikasch & Gobbels and Aamlid [30,31] have used samples produced by powder synthesis with sintering temperatures ranging from 1200°C to 1450°C. Despite the variations in both sample preparation and thermal history the data shows a clear consistency in size of the unit cell parameters with respect to the overall sample composition. Both unit cell parameters decrease in size with increasing strontium content in the samples.

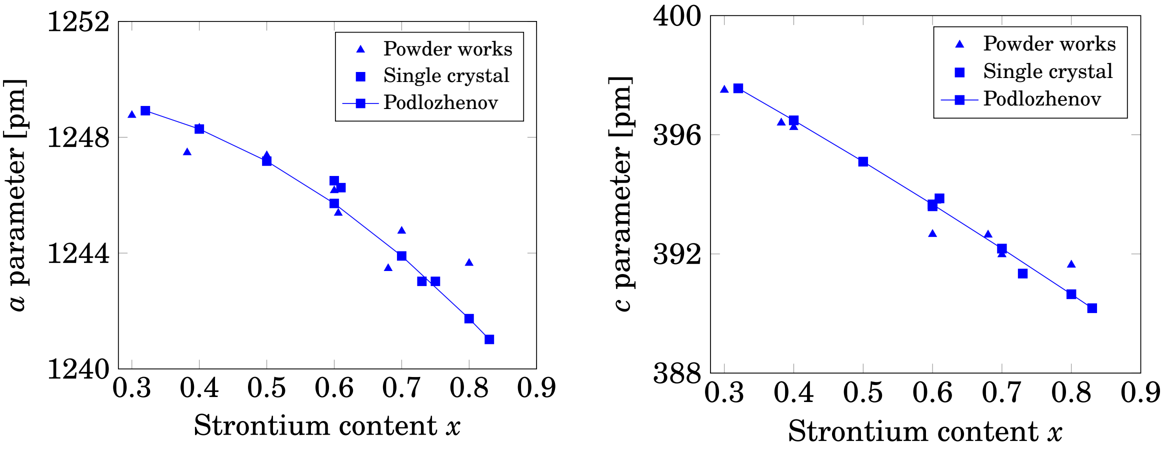

Figure 2.10: Unit cell parameters for SBN as a function of composition. There are some variations in sample preparation and thermal history for the samples where the values originate. Jamieson, Ballmann & Brown, Podlozhenov *et al.*, Schefer *et al.* and Oliver & Neurgaonkar [5, 24, 26, 28, 29] have used single crystals annealed at 1300-1400°C (marked with squares), while Nikasch & Gobbels and Aamlid [30, 31] have used powder samples sintered at 1200°C to 1450°C (marked with triangles). Quadratic trend lines are added for the data produced by Podlozhenov *et al.* [24].

The unit cell parameters of solid solutions at constant temperature are expected to have a linear relationship with the concentration of the constituent elements in the solution [32,33]. This relation is called Vegard's law [32]. The a parameters presented in Figure 2.10 show a deviation from linearity, and it is shown that a quadratic polynomial fit is better suited to describe the measured data. The same deviation is present for the c parameter, however not as pronounced, but still yielding a quadratic term in the polynomial fit [24]. With increasing strontium content the value of the unit cell parameters is decreasing. The decrease in unit cell parameters, hence also in unit cell volume, could be related to the difference in ionic radii between barium and strontium cations. The distribution of cations between the A1 and A2 sites in the TTB structure is changing with the composition of the solid solution. Increasing strontium content will lead to a corresponding decrease in barium content. This increase in strontium to barium ratio at the A2 sites is as shown in Figure 2.9. The strontium ions (1.18 Å) are significantly smaller than the barium ions (1.35 Å) [34]. An increase in strontium to barium ratio at the A2 sites could thus be a possible reason for the reduction in unit cell dimensions [9].

Relaxor properties

The relaxor properties of SBN are highly dependent on the strontium content. Lukasiewicz *et al.* [20] report dielectric measurements for single crystals of SBN, where SBN40 and SBN50 show rather narrow peaks in relative permittivity as function of temperature. The positions of the peaks are not changing with increasing frequency of the applied electric field. This illustrates the frequency independent nature of the transition temperature and hence normal ferroelectric behavior. As the strontium content increases there is a shift from normal ferroelectric to relaxor behavior. Single crystals with 61% strontium show a broadening of the peak in dielectric permittivity, compared to both SBN40 and SBN50 [20]. This is illustrated in Figure 2.6. The peak is also shifted towards higher temperatures for increasing frequency. The single crystals of SBN75 show relaxor behavior with significantly broadened peaks with a clear shift in peak position with increasing frequency [20]. The phase transition becomes more diffuse as the strontium content increases. The diffuse phase transition happens over a temperature interval, often referred to as the Curie range [14]. This shift from normal ferroelectric to relaxor behavior is reported to occur at 60% strontium content [20].

The relaxor features of SBN can be attributed to the increased structural disorder introduced by increased strontium content. At 20% strontium, the overall barium to strontium ratio is 4 to 1. As discussed earlier, by assuming that most of the barium cations are located at the A2 sites, all four A2 sites are filled with barium cations. The structure has now all barium cations in the A2 sites while strontium and the vacancy are located at the A1 sites. This structural configuration causes a high degree of order. An increase in strontium would result in a corresponding decrease in barium, creating room for strontium at the A2 sites. This allows for both strontium and barium to be located at the same crystallographic sites, reducing the structural order. The bond lengths from the cation at the A2 site to the surrounding anions would change with the cation [17]. This causes local distortions in the structures. In addition to the variation between strontium and barium, the vacancies distributed among the A sites results in some A sites being empty. The charge deficiency at these sites will create distortions to the neighboring niobium, which causes even larger distortions to the local surroundings [15, 17]. As shown in Figure 2.9, the increased strontium content in the overall structure is causing a corresponding decrease in barium content at the A2 sites. The possibility of structural disorder is thus increased by higher strontium content in the overall composition.

Phase transition

SBN undergoes an order-disorder phase transition from ferroelectric to paraelectric symmetry upon a temperature raise from ambient conditions [15]. The polarity of the ferroelectric structure is considered to originate from niobium cations being displaced along the *c* axis [35]. For strontium content below 60%, SBN is reported to have normal ferroelectric behavior. The phase transition occurring for samples in this composition range is reported to have a clear first order nature [36]. As the strontium content increases and relaxor behavior is introduced, the phase transition becomes more diffuse [36]. The phase transition temperature is also highly dependent on the overall composition of the sample. The Curie temperature ranges from above 200°C for samples with low strontium content, to below 50°C for samples with higher strontium content [7]. As the strontium content increases there is a corresponding decrease in the Curie temperature. This linear relationship is illustrated in Figure 2.11. The figure shows data as reported by Glass [23] and Lukasiewicz *et al.* [20]. A linear trend line is added to emphasize the pronounced compositional dependency of the phase transition temperature.

The difference in ionic radii between strontium and barium could be related to the decrease in Curie temperature. The effect of variance in ionic radii on functional features is also found in strontium doped barium titanate, $Ba_{1-x}Sr_xTiO_3$ [14]. A pure barium titanate structure has fully elongated Ti-O-Ti bond lengths due to the large barium cations. As the structure is doped with strontium, the Ti-O-Ti bond lengths contract along the tetragonal axis. This results in reduced polarizability of the structure, hence also a lowering of the transition temperature [37]. The same argument can be used for SBN where the presence of barium maintains elongated Nb-O-Nb bonds. The addition of strontium would reduce the Nb-O-Nb bond lengths, lowering the polarizability of the unit cell, hence also the Curie temperature [37].

Figure 2.12 shows the unit cell parameters for SBN61 as reported by Schefer *et al.* [26]. The reported Curie temperature for the investigated sample is indicated by a dotted

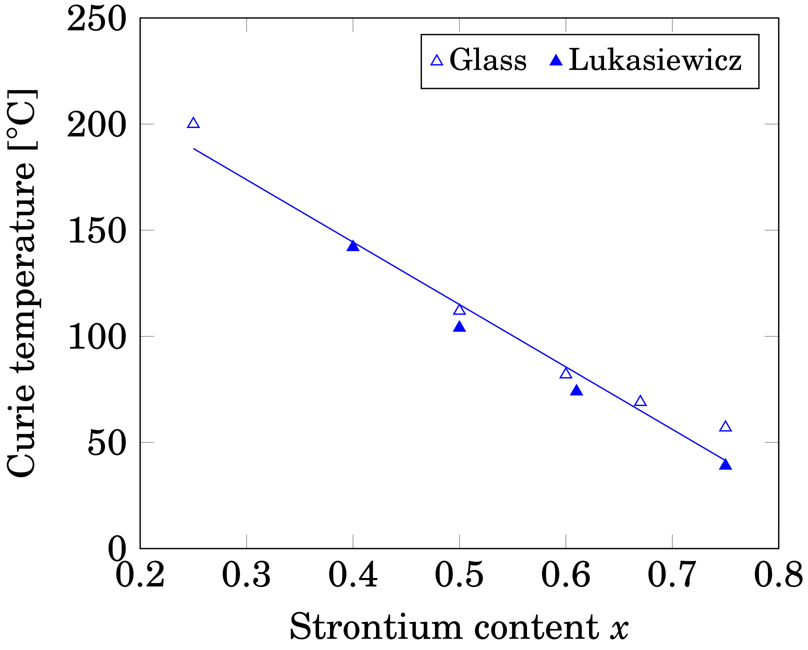

Figure 2.11: Reported Curie temperatures for various composition of strontium barium niobate. Lukasiewicz *et al.* [20] report data marked with empty triangles, while Glass [23] reports data marked with filled triangles. A linear trend line is indicated to illustrate the linear relationship between strontium content and phase transition temperature.

line. During heating the a parameter increases quite linearly due to thermal expansion. At the phase transition there is a small, almost unnoticeable change in slope, caused by the change in crystal structure. The c parameter shows however no sign of linear behavior with respect to temperature change. In addition to the thermal expansion, which is also experienced by the c parameter, there is another effect occurring when approaching the Curie temperature. The polarization in SBN occurs along the c axis, and when the polarization is lost, the c axis contracts. Hence there are two effects working to expand (thermal expansion) and contract (loss of polarization) the c axis. Close to the Curie temperature the contraction will overcome the thermal expansion, resulting in a significant decrease in the c parameter. When the phase transition is complete and the structure is throughout paraelectric, the thermal expansion will again be the only working effect on the unit cell parameters, thus increasing the c parameter. This is a typical behavior in ferroelectric materials in relation to the phase transition.

One of the attractive features of ferroelectric materials is the peak in dielectric permittivity close to the Curie temperature. In many applications where high dielectric

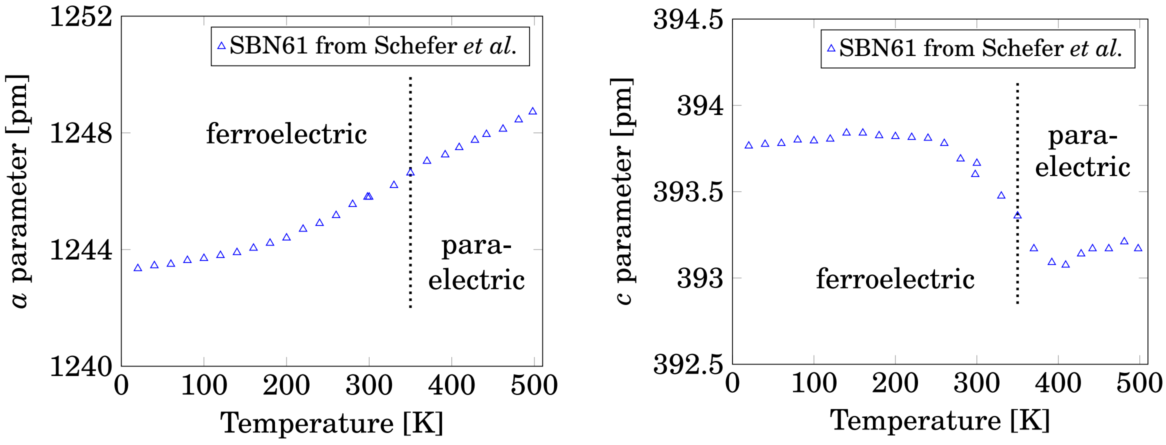

Figure 2.12: Unit cell parameters for SBN61 as reported by Schefer *et al.* [26]. The Curie temperature at 350 K is indicated with a dotted line, in addition to the ferroelectric and paraelectric regions. The phase transition from a ferro- to paraelectric structure is especially evident for the c parameter, due to the contraction along the c axis.

permittivities are important it is crucial to have a Curie temperature close to the materials's operating temperature. By utilizing the wide range of Curie temperatures for SBN, the composition could be chosen to customize the Curie temperature in accordance to the operating conditions. This makes SBN a versatile material system with respect to operation conditions, making it very suitable for ambient operating conditions [7].

2.2.3 Other ferroelectric materials with tungsten bronze structure

There are other material systems with tungsten bronze structure that are worth some attention when studying SBN. Especially in relation to the symmetry considerations of the high temperature paraelectric phase of SBN. The materials presented in this part are barium sodium niobate (BNN), potassium lithium niobate (KLN) and lead niobate (PN). The aristotype symmetry of these tungsten bronze materials is the $P4/mbm$ space group which is found in most of the paraelectric structures below [11].

Barium sodium niobate (BNN)

Barium sodium niobate, $Ba_4Na_2Nb_{10}O_{30}$, is a ferroelectric material crystallizing in the TTB structure. The material shows pronounced electro-optical and nonlinear-optical properties, making it e.g. an effective second harmonic generator [38]. The six A cations of BNN are distributed between the six A sites, where barium mostly occupies the A2 sites and sodium occupies the A1 sites. This is in accordance with the geometric considerations done for the tetragonal tungsten bronze structure of SBN. There are found indications of barium being able to occupy the A1 sites to a very small extend [11]. The six A cations in the BNN structure cause all A sites to be filled, in contrast to the partial vacancy found at the A sites in SBN. Above the Curie temperature, BNN is stable in the aristotype space group $P4/mbm$, while the orthorhombic symmetry of $Bbm2$ is most favorable below. The deviation from tetragonal symmetry is however not very pronounced [38]. The polarization in the BNN structure is along the c axis, the same as for SBN.

Potassium lithium niobate (KLN)

Potassium lithium niobate, $K_{6\text{-}x}Li_{4+x}Nb_{10}O_{30}$, is another ferroelectric compound with TTB structure. In contrast to both SBN and BNN are the cations in KLN somewhat differently distributed over the interstitial sites. The lithium ions are small enough to fit into the trigonal C sites, resulting in almost full occupancy of lithium at the trigonal sites. The A sites are filled with a mix of lithium and potassium [11]. Below the Curie temperature, KLN stabilizes with tetragonal symmetry and the space group $P4bm$. In the high temperature, paraelectric state, the $P4/mbm$ space group is most favorable [11].

Lead metaniobate (PN)

The third material described in this section is lead niobate, $Pb_5Nb_{10}O_{30}$. PN is, together with SBN, one of the most studied ferroelectric compounds with TTB structure [39]. The low temperature ferroelectric polymorph is orthorhombic with space group $Bb2_1m$, while the paraelectric tetragonal tungsten bronze has the aristotype $P4/mbm$ symmetry. The phase transition occurring at 570°C is one of the highest Curie temperatures among compounds with similar structure [11]. Both polymorphs are thermodynamically metastable with respect to the stable rhombohedral polymorph [11, 39, 40].

The metastable structures could however be stabilized by quenching from 1250°C [40]. The metastable orthorhombic structure resembles the room temperature structure of BNN with lead cations completely filling the pentagonal A2 sites [11]. The additional lead is distributed between the quadratic A1 sites. A peculiar feature of PN is the polar direction being perpendicular to the tetragonal axis, rather than along the tetragonal axis as for SBN [11,39,40]. The polarization mechanism of TTB structures is in general not fully understood [10], and it is difficult to explain the difference in polar direction between SBN and PN. It is however assumed that the 6*s* lone pair of the Pb^{2+} cation is interfering with the polarization mechanism, and thus could be a reason for the difference [10, 11]. The orthorhombic distortion from tetragonal symmetry is also attributed to the in-plane interactions between the 6*s* lone pair of Pb^{2+} and the niobium in the large, pentagonal sites [10, 11]

2.2.4 Symmetry considerations

Table 2.1 lists the four abovementioned ferroelectric compounds with tungsten bronze structure. Similarities with respect to crystal structure and behavior indicate that BNN, KLN and PN are worth using as a basis for comparison when examining SBN. As observed in Table 2.1, the compounds BNN, KLN and PN are reported to have $P4/mbm$ as their high temperature, paraelectric space group. Ever since Jamieson *et al.* [5] treated SBN in 1968, it has been discussed whether the paraelectric space group of SBN should be equal to the other corresponding compounds. Jamieson *et al.* proposed two potential space groups for the paraelectric phase; $P4/mbm$ and $P\bar{4}b2$. Since several similar compounds with TTB structure adopt the $P4/mbm$ space group in the paraelectric state, $P4/mbm$ is also a realistic suggestion for the paraelectric state of SBN. The suggestion is strengthen by the group-supergroup relation between the ferroelectric space group $P4bm$, and $P4/mbm$. The lower group, $P4bm$, transforms to the supergroup by addition of an inversion center to the symmetry operators [5]. $P4bm$ is a polar space group giving rise to the ferroelectric property of SBN. The addition of an inversion center causes the structure to become unpolar and paraelectric. The same group-supergroup relationship is not found between $P4bm$ and $P\bar{4}b2$. Jamieson *et al.* [5] report that $P\bar{4}b2$ gives the best fit to the crystallographic data, disregarding $P4/mbm$ as the paraelectric space group. Due to the lack of group-supergroup relation between $P4bm$ and $P\bar{4}b2$, strong discontinuities in physical properties are expected at the phase transition [11]. Such discontinuities are however not observed [11], weakening the possibility of $P\bar{4}b2$ being the right space group for the paraelectric phase.

Table 2.1: The ferroelectric and paraelectric space group symmetry of SBN, BNN, KLN and PN.

Composition	Abbreviation	Polar axis	Symmetry	
			Below T$_c$	Above T$_c$
$Sr_{5x}Ba_{5(1-x)}Nb_{10}O_{30}$	SBN	[001]	$P4bm$	$P\bar{4}b2$
$Ba_4Na_2Nb_{10}O_{30}$	BNN	[001]	$Bbm2$	$P4/mbm$
$K_{6\text{-}x}Li_{4+x}Nb_{10}O_{30}$	KLN	[001]	$P4bm$	$P4/mbm$
$Pb_5Nb_{10}O_{30}$	PN	[010]	$Bb2_1m$	$P4/mbm$

The symmetry of the ferroelectric phase is however established with greater certainty. Jamieson *et al.* [5] treated SBN in 1968 and proposed three space groups for the ferroelectric phase; $P4bm$, $P4/mbm$ and $P\bar{4}b2$. However, only one of these space groups can give rise to ferroelectric properties. The centrosymmetric nature of $P4/mbm$, and the fact that $P\bar{4}b2$ has no polar axis, discard them both as possible space groups for a ferroelectric structure. This leaves $P4bm$ as the most probable space group for the ferroelectric phase [5], which has later been established by refinement of X-ray measurements [24].

2.3 Cation ordering in functional oxides

2.3.1 Spinels

Oxides containing more than one type of cations could be subjected to cation ordering. This is easily visualized by examining the spinel structure. A spinel has the generic formula of AB_2O_4, where the cations normally are either A^{2+} and B^{3+} (2-3 spinels) or A^{4+} and B^{2+} (4-2 spinels) [12,41]. The spinel structure is built up by oxygen anions in an cubic close-packed structure with cations in 1/2 of the octahedral sites and 1/8 of the tetrahedral sites. In a cubic close-packed oxygen structure, there are twice as many tetrahedral sites than octahedral [12,41]. Combined with the spinel cation occupancy, this leaves twice as many cations in octahedral compared tetrahedral sites. Thus, the B cations fit in the octahedral sites, while the A cations fit in the tetrahedral sites. This is the case for a normal spinel, denoted (A)[B_2]O_4. The parentheses indicate tetragonal sites, while the square brackets indicate octahedral sites. The opposite extrema is the inverse spinel, where the A cations are located in the octahedral sites, and the B cations are distributed between the remaining octahedral sites and the tetrahedral sites. The inverse spinel is denoted (B)[AB]O_4. The degree of inversion could thus be defined as the fraction of tetrahedral sites occupied by B cations [42]. The configurational entropy of the structure is changing with the degree of inversion [41, 43]. The value of the configurational entropy for spinels are increasing for increasing inversion, with a maximum at $x = 2/3$ [41, 43]. The degree of inversion is dependent on the temperature, causing the configurational entropy to increase with increasing temperature [43].

A raise in temperature would increase the thermal energy of the ions in the structure, allowing them to oscillate more intensely at their sites. The increase in ionic oscillations will also increase the probability for the ions to move between the sites. This will in turn increase the degree of inversion and hence also the configurational entropy of the spinel. At elevated temperatures it would be expected that the spinel structure would favor more disorder and inversion compared to ambient conditions.

2.3.2 A hypothesis for the tetragonal tungsten bronze structure

Both strontium and barium could in principle be located at the two types of interstitial A sites in the SBN structure. However, there is a pronounced agreement in literature that barium is too large to fit into both positions, leaving it fixed to the largest, pentagonal site [24–27]. As long as the barium cation is fixed to the largest site, the only cation distribution possible is that of strontium. The combination of strontium and a vacancy at the A1 site allows for some degree of disorder, even though barium is fixed to the A2 site. The argument of barium being fixed to the pentagonal site due to its larger ionic size, is however not necessarily obvious. In 4-2 spinel structures, the larger cations have preference towards the larger, octahedral positions. In 2-3 spinels, it is found that the opposite is the case, where the larger cation have a preference towards the tetragonal sites, contradicting the argument of ionic radii [44]. In the orthorhombic structure of BNN, barium is reported to be present in both the pentagonal and quadratic sites [38]. The orthorhombic distortion from tetragonal symmetry is not very pronounced, and the BNN structure is thus very similar to the TTB structure of SBN [11]. Based on these observations, and if one were to disregard reported trends for one second, it is not unthinkable that barium is able to occupy the smaller, quadratic site in SBN.

As described for the spinel structure, an increase in temperature will increase the thermal energy of the ions, hence also increase their ability to oscillate. At increased temperatures, the spinel structure tend to change its degree of inversion towards the point of maximum configurational entropy [43]. In the TTB structure, such behavior is assumed to be constrained by the difference in ionic radii of the barium cation and the size of the smaller A1 sites. However, if barium actually is able to occupy the smaller sites, the tendency for such occupation is suggested to increase with increasing temperature. The cation rearrangements associated with barium entering the smaller A1 site is illustrated in Figure 2.13. The top figure shows the unit cell of SBN20 with all four A2 sites filled with barium cations. If a barium cation moves into to the A1 site, it would happen at the expense of either the strontium cation or the vacancy. These two possible rearrangement processes are illustrated by arrows in Figure 2.13. Both processes are for simplicity referred to as barium inversion in the coming discussion. Additional rearrangement where the strontium and vacancy move between the A1 sites could also occur for increasing sintering temperature. The process of barium moving from A2 to A1, i.e. the process of barium inversion, is however emphasized in the coming discussion.

The energetics related to the process of barium moving from A2 to A1 could be described by the Gibbs energy, $\Delta G = \Delta H - T\Delta S$. Since barium disfavor occupation at the A1 sites, it would be natural to assign an energy cost of moving the barium cation from the A2 to the A1 site. This cost could be related to the enthalpy term in the expression for Gibbs energy. As the barium cation moves from A2 to A1 the structural disorder is assumed to increase, related to the entropy term in the Gibbs expression. At elevated temperatures, the term $-T\Delta S$ in the expression for ΔG becomes increasingly negative. The enthalpy cost of barium inversion is thus compensated for by the temperature and entropy term.

Another variable that could influence the driving force for barium inversion, is the barium to strontium ratio in the overall composition. As discussed earlier, samples with 20% strontium gives a 4 to 1 cation ratio and all four A2 sites presumptively filled with barium cations. SBN20 is thus the theoretical lower limit for SBN in the TTB structure assuming only barium occupancy at the A2 sites. However, at this lower limit the statistical probability of barium moving from a A2 to A1 site is at its greatest. As the overall barium content is reduced, the amount of barium at the A2 sites decreases correspondingly, as shown in Figure 2.9. This would thus cause a reduction in the compositional driving force for barium to move from the A2 to the A1

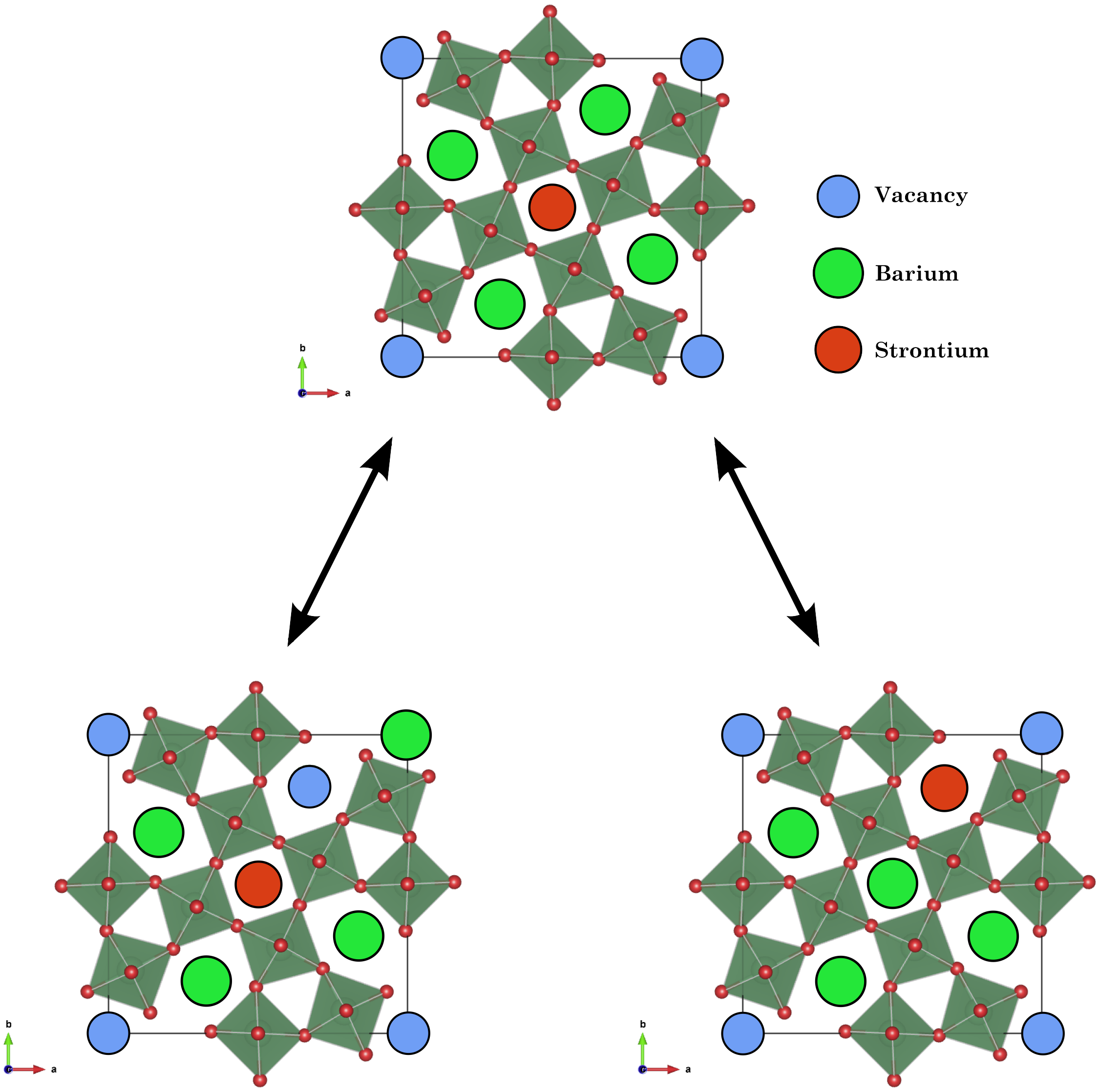

Figure 2.13: Cation arrangement for SBN20 i association with barium inversion. The unit cell of SBN20 contains four barium cations, one strontium cation and one vacancy. When investigating a single unit cell it is for simplicity assumed that the A2 positions are filled with barium cation, as shown in the top figure. Cation rearrangement could occur if barium switches place with either the strontium cation or the vacancy. Both processes are illustrated with an individual arrow and are referred to as the process of barium inversion in the coming discussion.

sites.

The aim of this thesis is to investigate how the cation distribution is affected by variations in thermal history. The hypothesis is that the cation disorder within the crystal structure is increasing as the sintering temperature is increased. The possibility for barium to move from A2 to A1 is especially emphasized when investigating the cation disorder. If present, the tendency for barium inversion should be governed by two main factors, the degree of strontium content and the thermal history. Based on the presented arguments, the barium inversion is assumed to be increasing with decreasing strontium content and increasing sintering temperature.

Chapter 3

Methods

3.1 Synthesis

3.1.1 Powder preparation

Samples of SBN with three compositions were synthesized through the solid state route. The three compositions chosen are listed in Table 3.1.

Table 3.1: The compositions of SBN investigated in this work. Abbreviations used later in this text are also included.

Chemical formula	Abbreviation
$Sr_{0.30}Ba_{0.70}Nb_2O_6$	SBN30
$Sr_{0.40}Ba_{0.60}Nb_2O_6$	SBN40
$Sr_{0.50}Ba_{0.50}Nb_2O_6$	SBN50

The three precursors used in the synthesis, $SrCO_3$ (>98%), $BaCO_3$ (99%) and Nb_2O_5 (99,99%) were all delivered by Aldrich. Prior to mixing, the precursors were dried (200°C for 8 hours) to remove water from the powders. The precursors were weighted and mixed in stoichiometric ratios, according to the compositions listed in Table 3.1. Ethanol was added to create a slurry out of the precursors. Mortar and pistil were used to mix the slurry, before it was set to dry in a fume cupboard. After all ethanol was evaporated, the dry powder was pressed into pellets (25 mm diameter) using a uniaxial pressing tool with a pressure of 30 MPa. Subsequently, the pellets were heat treated (1100°C for 3 hours), with $300°\mathrm{C\,h^{-1}}$ heating rate in an atmospheric environment.

After the initial heat treatment, mortar and pistil were used to crush the pellets into powder. The powder was then added to a 100 mL polyethylene bottle, together with yttria-stabilized zirconia milling balls and ethanol. Wet ball milling was performed for 20 hours with a milling ball angle of 60°. To subsequently remove the ethanol from the slurry, a rotational vacuum evaporator was used. The powder was sieved (250 μm), and then pressed into pellets (10 mm) using a uniaxial pressing tool with a pressure of 90 MPa. The samples studied by dielectric spectroscopy were also pressed in a cold isostatic press with a pressure of 2 kbar.

3.1.2 Sintering conditions

The samples were heat treated with a sintering program comprising five temperatures, where the same oven was used for all samples. This was to ensure any deviations from the oven's temperature set point, was introduced as a constant offset for all samples, and not as a varying error from sample to sample. An alumina crucible was used to protect the samples from any potential contaminations from the oven during heat treatment. The samples were placed on a bed of sacrificial powder (heat treated powder with the same composition as the sample) on the lid of the crucible. The crucible was then placed upside down on top of the sample. By this setup, the samples were protected from potential contaminations, and at the same time not being totally sealed of from the atmospheric environment

The sintering program included five set temperatures, 1200°C, 1300°C, 1350°C, 1375°C and 1400°C. All samples were heated with a heating rate of 300°C h^{-1} followed by an extended period of time at the set temperature. The samples at 1200°C were held for 48 hours, and the rest for 12 hours. This was to give the samples enough time to reach equilibrium at the given temperature. The sample sintered at the lowest temperature was held significantly longer than the rest due to potentially reduced cation movement. After the holding time was concluded, the samples were quenched with a cooling rate of 600°C h^{-1} to freeze in the cation distribution within the crystal structure.

3.1.3 Density measurements

Density measurements by Archimedes' method [45] were conducted for samples prepared for dielectric measurements. The pellets were gently polished by SiC polishing paper to remove any sacrificial powder left from the sintering. The pellets were then put in a vacuum chamber at 25 mbar for 15 minutes to evacuate the open pores. The samples were then covered with isopropanol, and the low pressure was maintained for 30 minutes to ensure all pores being filled with liquid. The system was then pressurized to ambient conditions and held for another 30 minutes. This was to give the isopropanol time to reach thermal equilibrium with the surroundings after the pressure increase. The pellets were then weighted in three ways. First, the pellets were weighted submersed in isopropanol (m_{sub}). Then in air (m_{wet}) after being lightly wiped off with a moist tissue. Finally, the dry weight (m_{dry}) was measured after drying in a heating cabinet.

To determine the actual porosity of the samples, the theoretical density was calculated from X-ray data. The bulk density of the samples was calculated from the measured weights and the following equation

$$\rho_{\text{bulk}} = \frac{m_{\text{dry}}}{m_{\text{wet}} - m_{\text{sub}}} \cdot \rho_{\text{isop}}, \tag{3.1}$$

where ρ_{bulk} is the bulk density, m_{dry}, m_{wet} and m_{sub} is the weight of the dry, wet and submerged samples respectively, and ρ_{isop} is the density of isopropanol. The true density of the samples were then calculated from the theoretical and bulk densities using

$$\rho_{\text{true}} = \left(1 - \frac{\rho_{\text{th}} - \rho_{\text{bulk}}}{\rho_{\text{th}}}\right) \cdot 100\%, \tag{3.2}$$

where ρ_{true} and ρ_{th} are the true and theoretical densities respectively.

3.2 Characterization

The heat treated samples were crushed into powder by mortar and pistil, before characterization by powder X-ray diffraction. Two types of X-ray setups were used in this work; high-temperature X-ray diffraction (HT-XRD), and X-ray diffraction with monochromatic radiation.

3.2.1 Temperature calibration

Prior to each HT-XRD experiment, a temperature calibration scan was performed. A sample of alumina powder was scanned with the same setup as used for the SBN samples. Pawley fitting with the Bruker AXS Topas 4.2 software was used to find the unit cell parameters of the alumina sample. Thermal expansion causes the unit cell parameters to expand during the experiment, and can be used to determine the actual temperature in the sample. The procedure was conducted as described by Stinton & Evans [46]. Based on the unit cell parameters found in Topas, corresponding temperatures were calculated for both a and c parameters. This resulted in two corresponding temperatures for each set temperature, and an average value was used as the actual temperature in the sample. The set temperatures, the actual sample temperatures and the offset for both series are presented in Appendix C. The measured temperature data was then adjusted according to the calibration values.

3.2.2 High-temperature X-ray diffraction

Two HT-XRD experiments were performed in air using a Bruker D8-Advance. The setup consisted of a Cu Kα_1 and Kα_2 radiation source, and a resistive heater combined with water cooling. Additional experimental details are presented in Table 3.2.

The first experiment collected data in the temperature range from 30°C to 215°C, with temperature intervals ranging from 5°C to 15°C. The second experiment ranged from 30°C to 440°C, with temperature intervals of 15°C and 20°C. In both series the powder samples were positioned in a rectangular (1 cm × 1.3 cm) alumina sample holder. During temperature increase, the sample was heated at a rate of 0.1°C s^{-1}. When the set temperature was reached, the temperature was held for 5 minutes to ensure the sample being in thermal equilibrium with the surroundings prior to recording. Then the X-ray recording was conducted for 34 minutes, before next heating cycle began. The setup's temperature offset was not accurately known prior to experiment execution, but was adjusted for in accordance with the temperature calibration.

3.2.3 Monochromatic X-ray diffraction

The monochromatic experiments were performed at room temperature in air. A Siemens D5000 diffractometer using Bragg Brentano-geometry with a $\theta - 2\theta$ setup was used. The samples were scanned in a 2θ range of $10° - 120°$, with a step size of 0.015° and a 4 seconds scan time per step. The setup included a graphite monochromator and a Braun position sensitive detector. The Cu $\mathrm{K}_{\alpha 2}$ radiation was filtered out by the monochromator allowing only Cu $\mathrm{K}_{\alpha 1}$ radiation to reach the sample. The monochromator causes

Table 3.2: Experimental details of the high-temperature X-ray diffraction experiment.

Total temperature ranges	30 – 215°C and 30 – 440°C
Heating rate	$0.1°\mathrm{C\,s^{-1}}$
Holding time prior to recording	5 minutes
Recording time	34 minutes
2θ range	14 – 75°
Step size	0.016°
Holding time per step	0.5 second
Divergence slit	0.2 mm
Anti-scatter slit	11 mm
Detector slit	21 mm
Detector opening	6°
Acceleration voltage	40 kV
Current	40 mA

a general reduction in intensity, compensated for by increased scan time at each step. Additional experimental information is found in Table 3.3.

Table 3.3: Experimental details of the monochromatic X-ray experiments.

2θ range	10 – 120°
Step size	0.015°
Holding time per step	4 seconds
Focus slit	0.2 mm
Aperture slit	1.0 mm
Scatter-radiation slit	24 mm
Detector slit	34 mm
Detector opening	10°
Acceleration voltage	40 kV
Current	50 mA

3.2.4 Pawley fitting

Initial structural investigations were conduced through Pawley fitting with the Bruker AXS Topas 4.2 software. The space group and initial unit cell parameters for each composition were supplied in accordance with the data presented in Table 3.4. Then unit cell parameters were calculated for each sample.

Table 3.4: Space group and initial unit cell parameters supplied to Topas prior to Pawley fitting, as reported by Podlozhenov [24].

Initial a parameter	12.48 – 12.49 Å
Initial c parameter	3.95 – 3.98 Å
Space group	$P4bm$

3.2.5 Rietveld refinement

A full Rietveld refinement of the X-ray data was performed using the Bruker AXS Topas 4.2 software. Table 3.5 presents the structural data for SBN61 as reported by Carrio *et al.* [25]. These data were used at a starting point for the refinement together with the unit cell parameters and space group presented in Table 3.4. The refinement was performed with the symmetry constraints given by the tetragonal space group $P4bm$. The peak shapes were fitted to a TCHZ-type Pseudo-Voigt function, while the background was fitted to a Chebychev polynomial.

Unit cell parameters, atomic positions, site occupancies and isotropic thermal displacement factors were all subject to some degree of relaxation during the refinement. However, prior to the refinement some additional constraints were imposed to the data set. The occupation of strontium and barium at the A1 and A2 sites were conditioned to always add up to the nominal composition of the samples, when the site multiplicity was taken into account. The data set reported by Carrio *et al.* is based on both X-ray and neutron analysis, yielding good structural data for both cations and oxygen ions. The analysis conducted in the present work is based on X-ray experiments only, which gives less reliable data with respect to oxygen ion position and thermal displacement. The thermal displacement factors of oxygen ions were thus not refined upon at all, and were kept constant during the whole refinement. The thermal displacement factor for strontium, barium and niobium were however all refined upon. The symmetry and compositional constrains are presented in Table 3.6, where the bold values were kept fixed during the refinement. The equations represent the values linked by compositional constraints, while the rest were open for refinement. Note that the values in the compositional constraints in Table 3.6 only are valid for SBN50. For SBN40 and SBN30 other constraints, corresponding to the respective compositions, were used. These are presented in Appendix A.

Refinement procedure

The refinement was carried out as stepwise process, where the variables were refined upon in turn. According to the symmetry constrains of the space group, some atomic positions were either set to a fixed position or linked to each other. The values linked to each other were always refined in pairs, while the fixed values never were open for refinement.

The starting values given by Carrio *et al.* [25] are based on SBN61 samples. The refinement was thus begun with SBN50 sintered at 1300°C, assuming that the sample closest in composition also have the most similar atomic positions. The A1 and A2 site occupation and thermal displacement factors were all kept fixed during the first part of the refinement. The atomic positions of the cations were at first refined in turn, before the oxygen anions were given the possibility to relax. At this stage of the refinement, the ions were always refined individually. Due to the lower refinement accuracy related to the oxygen positions, the values were never allowed to drift far off the starting point. After an initial relaxation of all atomic positions, the thermal displacement factors of the cations were allowed to change. These thermal displacement factors were then fixed for the rest of the refinement.

After relaxing the thermal displacement factors, the atomic positions were again refined as before. The site occupations were also allowed to change during the second round of refinement. This refinement procedure was then repeated in order to fine tune the atomic positions and site occupations. During the last part of the refinement, some positions have been relaxed in pairs, e.g. the A1 and A2 sites, and the two niobium positions. It has been important to make sure that no values were drifting far off the starting points. This is however not the case for the A1 and A2 site occupations, which have been allowed change according to the compositional constraints. The values given by negative numbers have been changed to the corresponding positive value by the addition of 1.

Table 3.5: The atom positions, site multiplicity (Mp.), occupation and thermal displacement factor (B_{iso}) for all atoms in the TTB structure of SBN, as reported by Carrio *et al.* *et al.* [25]. The data is, together with the data in Table 3.4, used as a starting point for the Rietveld refinement.

Position	Atom	Mp.	*x*	*y*	*z*	Occ.	B_{iso}
A2	Ba	4	0.17214	0.67214	0.4760	0.04875	4.31
A2	Sr	4	0.17214	0.67214	0.4760	0.3999	3.07
A1	Sr	2	0.0000	0.0000	0.4507	0.7353	3.69
A1	Ba	2	0.0000	0.0000	0.4507	0	-
Nb1	Nb	2	0.5000	0.0000	-0.0176	1	1.70
Nb2	Nb	8	0.07529	0.21097	-0.0187	1	0.73
O1	O1	4	0.2817	0.7817	-0.054	1	0.17
O2	O2	8	0.1413	0.0647	-0.059	1	2.45
O3	O3	8	0.3413	0.0055	-0.054	1	2.41
O4	O4	8	0.2965	0.4175	0.468	1	3.68
O5	O5	2	0.0000	0.5000	0.513	1	4.87

3.2.6 Dielectric spectroscopy

Dielectric measurements were conducted with a Novotherm analyzer at six samples; SBN40 and SBN50, both sintered at 1300°C, 1350°C and 1400°C. The samples' surfaces were polished with fine-grained silicon carbide paper, before rinsed in an ultrasonic bath. Gold electrodes were then sputtered at both surfaces. The samples were heated in synthetic air from 25 to 350°C at a heating rate of 2°C min^{-1}, held at 350°C for 10 minutes before being cooled down at the same rate. During the temperature cycle, dielectric permittivity was measured every 30 seconds, at frequencies ranging from 10^0 Hz to 10^6 Hz with step size of one decade.

Table 3.6: Constraints imposed on samples with 50% strontium by composition and point group symmetry. The values indicated in bold are kept constant during the refinement, while the linked positions is described by equations. The remaining values, marked with the *at* signs, are subject for relaxation during the refinement.

Position	Atom	Mp.	x	y	z	Occ.	B_{iso}
A2	Ba	4	X_{A2}	$X_{A2} + 0.5$	@	$0.625 - 0.5Occ_{Ba,A1}$	@
A2	Sr	4	X_{A2}	$X_{A2} + 0.5$	@	$0.625 - 0.5Occ_{Sr,A1}$	@
A1	Sr	2	**0.0000**	**0.0000**	@	$Occ_{Sr,A1}$	@
A1	Ba	2	**0.0000**	**0.0000**	@	$Occ_{Ba,A1}$	@
Nb1	Nb	2	**0.5000**	**0.0000**	@	**1**	@
Nb2	Nb	8	@	@	@	**1**	@
O1	O1	4	X_{O1}	$X_{O1} + 0.5$	@	**1**	**0.17**
O2	O2	8	@	@	@	**1**	**2.45**
O3	O3	8	@	@	@	**1**	**2.41**
O4	O4	8	@	@	@	**1**	**3.65**
O5	O5	2	**0.0000**	**0.5000**	@	**1**	**4.87**

Chapter 4

Results

4.1 Structural dependency on thermal history

4.1.1 X-ray diffractograms

Peak intensity

X-ray diffractograms of SBN30, SBN40 and SBN50 sintered at 1350°C and 1400°C are presented in Figure 4.1. From the figure it is observed variations in peak intensity between the two temperatures for each composition. The changes in intensity are however not equal for all reflections. This is especially evident for SBN50, where an increase in sintering temperature results in both an increase and a decrease in peak intensity. The peak at approximately $2\theta = 22.5°$ (marked with a black arrow) looses intensity, while the peaks at approximately $2\theta = 27.7°$ and $2\theta = 32.1°$ (marked with red arrows) gains intensity upon increasing sintering temperature. The other peaks (marked with red circles), are barely affected by the temperature increase at all.

These variations are not equally distinct for the two other compositions, but there are some indications of similar behavior for both SBN30 and SBN40 as well. For SBN30, the peaks marked with red circles are neither gaining nor loosing intensity. The peaks marked with black arrows are in contrast loosing intensity as the sintering temperature is increased. The same behavior is found for SBN40 where the peaks at $2\theta = 26.6°$ and $2\theta = 28.5°$ (marked with red circles) are not changing much, while the others (marked with black arrows) are loosing intensity.

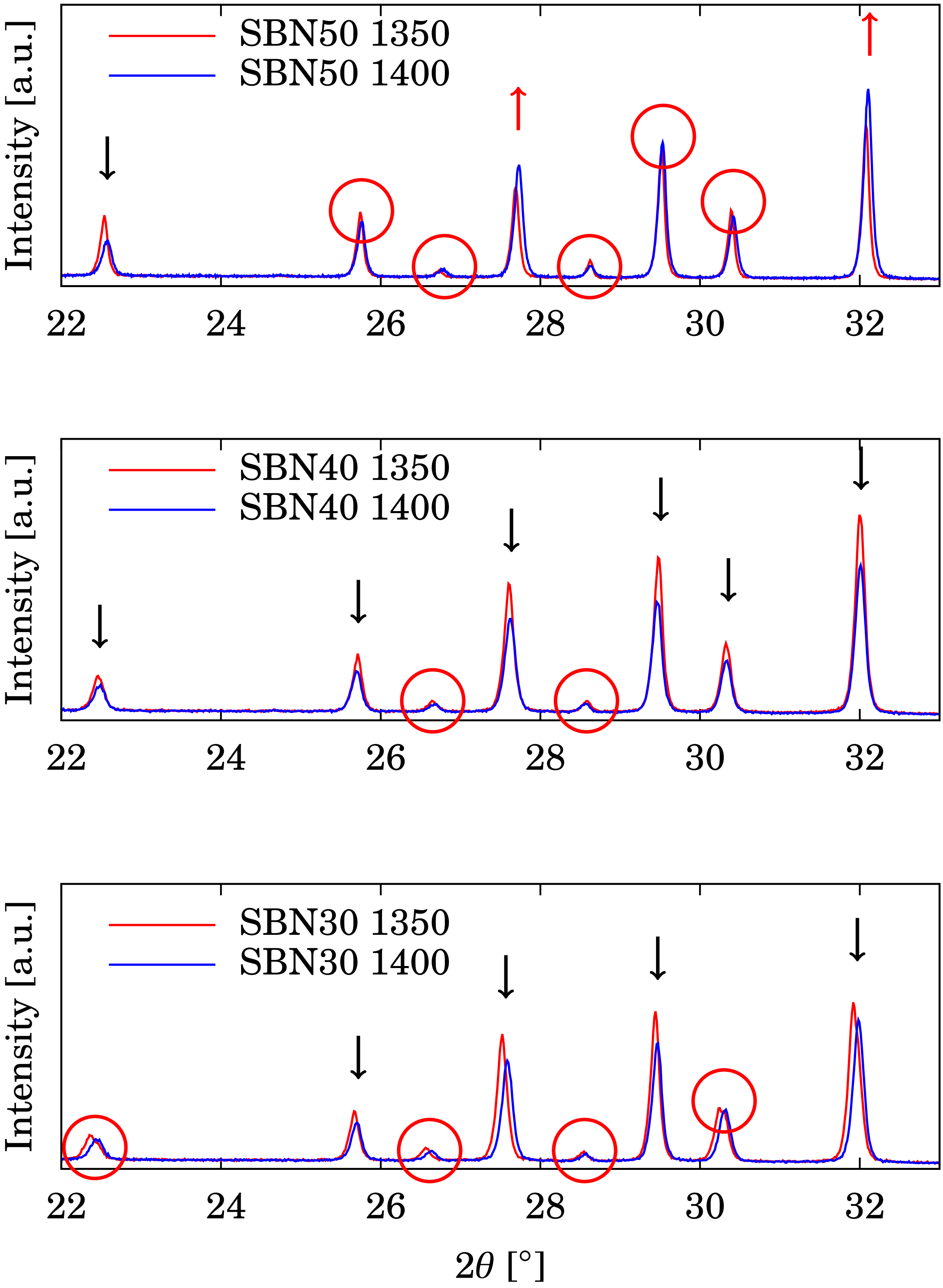

Figure 4.1: X-ray diffractograms of SBN30, SBN40 and SBN50 sintered at 1350°C and 1400°C. The arrows indicate changes in intensity for increasing sintering temperature. The black arrows indicate reduction in intensity while the red arrows indicate increase in intensity. The red circles mark peaks with little or no intensity variations for increasing sintering temperature.

Shift in peak position

Another thing to observe is a shift in peak position as the sintering temperature is increased. This is especially evident for SBN30 as shown in Figure 4.2. The figure show that the peaks are shifted towards higher 2θ values as the sintering temperature increases. These shifts are present in the whole investigated 2θ range, all the way up to $2\theta = 110°$. Some peaks have a more sensitive peak position, undergoing a larger shift than the others. These peaks are indicated with black arrows in Figure 4.2. This could indicate that the shift is having a dependency with respect to certain crystallographic sites in the structure. The peaks in the figure are also labeled with the corresponding *hkl*-values. Some peaks correspond to overlapping reflections, and are thus labeled with two sets for *hkl*-values. It is however difficult to find a clear correlation between *hkl*-values and which of the peaks are being subject to positional shift.

The same tendencies of positional shift are present for SBN50, while being more difficult to observe in the diffractograms of SBN40. The reflections showing the highest degree of peak shift for SBN50 are indicated by arrows in Figure 4.3. These are the same peaks showing the greatest shift for SBN30, supporting the suggestion of a positional shift dependency with respect to crystallographic position in the structure.

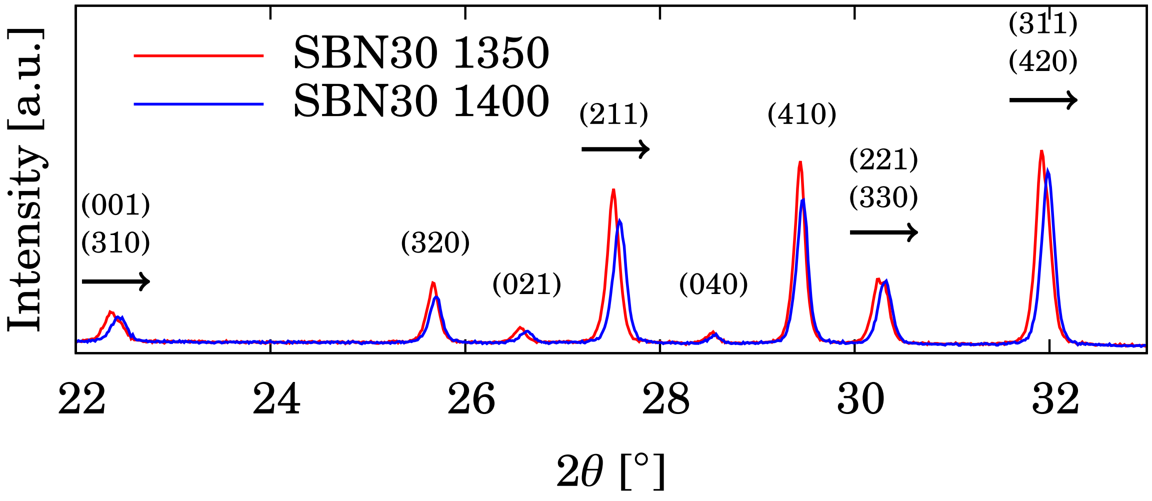

Figure 4.2: X-ray diffractograms for SBN30 sintered at 1350°C and 1400°C. The black arrows mark the peaks shifting position towards higher 2θ values for increasing sintering temperature. Each peak is labeled with the corresponding *hkl*-values. The peaks corresponding to overlapping reflections are labeled with two sets of *hkl*-values.

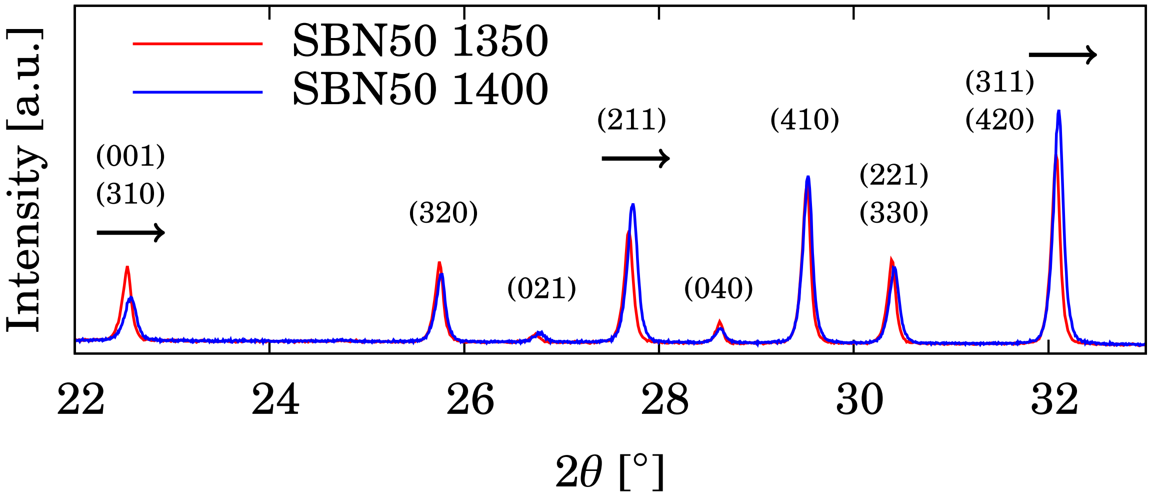

Figure 4.3: X-ray diffractograms for SBN50 sintered at 1350°C and 1400°C. The black arrows mark the peaks shifting position towards higher 2θ values for increasing sintering temperature. Each peak is labeled with the corresponding *hkl*-values. The peaks corresponding to overlapping reflections are labeled with two sets of *hkl*-values.

4.1.2 Unit cell parameters

Unit cell parameters of all compositions were found from the X-ray diffractograms through Pawley fitting in Topas. The calculated values were then compared to a range of reported values and presented in Figures 4.4 to 4.6. The c parameters are highlighted for a shorter range of strontium content in Figure 4.5.

All measured c parameters are smaller than the reported values, while all a parameters are larger. The unit cell parameters are however not constant for all samples, and are dependent on the sintering temperature. A trend is observed for the c parameters, which are decreasing as the sintering temperature increases. Linear trend lines are plotted for each sintering temperature in Figures 4.4 and 4.5, showing nearly the same slopes as for the near-linear trend reported by Podlozhenov [24]. The c parameters are shifted towards lower values, but the dependency with respect to strontium content is still the same. The dependencies for sintering temperature and strontium content do seem to be independent of each other. Another thing to note from Figure 4.5 is the difference in c parameter value between the lowest and highest sintering temperature. For SBN30, this difference is almost twice as large compared to the samples with 50% strontium content. The changes induced by increased sintering temperature are thus larger for samples with lower strontium content.

The variations in a parameter are not equally distinct, and it is difficult to get a equally clear picture of a potential temperature dependency from the data presented in Figure 4.6. However, there are some indications of temperature dependency of the a parameter as well. First of all are all measured values larger than the reported data from Podlozhenov. Secondly are the slopes of the measured data to some extent following the slope of the reported data.

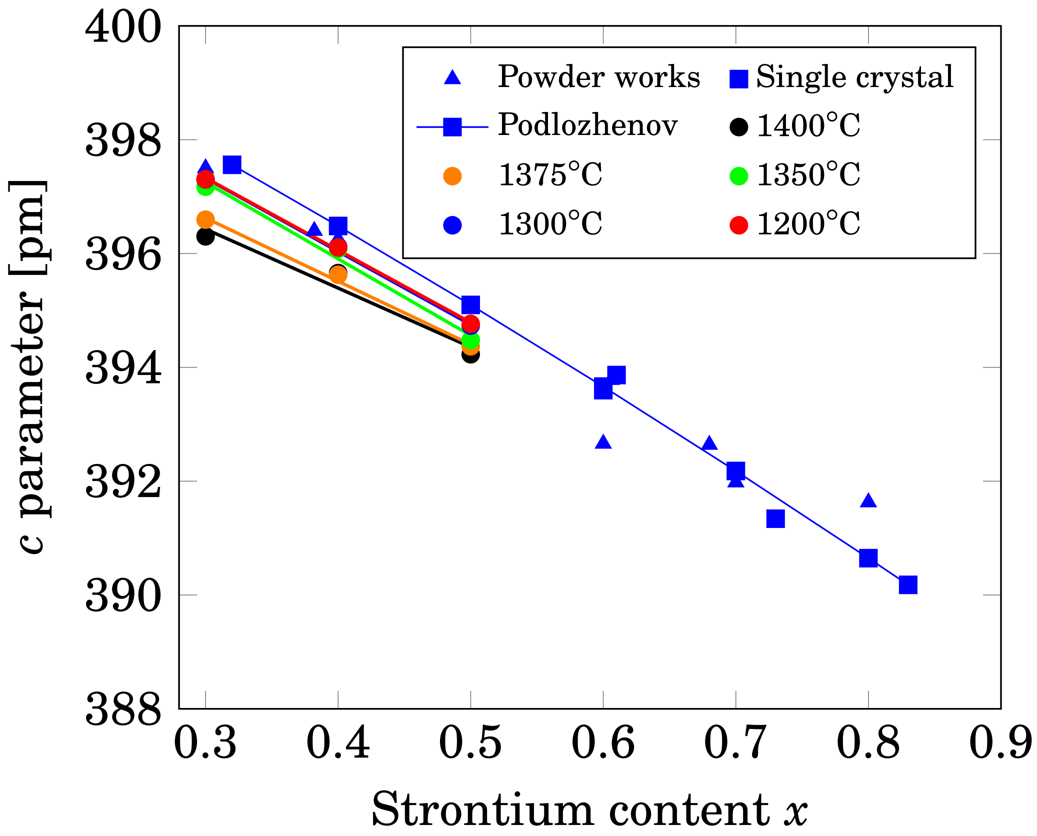

Figure 4.4: Measured c parameters (marked with circles) plotted together with reported unit cell parameters. The reported data are from various sources, with some variations in sample preparation and thermal history. Jamieson, Ballmann & Brown, Podlozhenov, Schefer *et al.* and Oliver & Neurgaonkar [5,24,26,28,29] have used single crystals annealed at 1300-1400°C (marked with squares), while Nikasch & Gobbels and Aamlid [30,31] have used powder samples sintered at 1200°C to 1450°C (marked with triangles). A trend line is added for the data reported by Podlozhenov [24].

The change in unit cell parameters from 1200°C to 1300°C is almost non-existent, and the data points from these two sets of temperatures are difficult to distinct from each other. The response induced by increasing sintering temperature is occurring between 1300°C and 1350°C. A lower limit for this response seems to be within this temperature range.

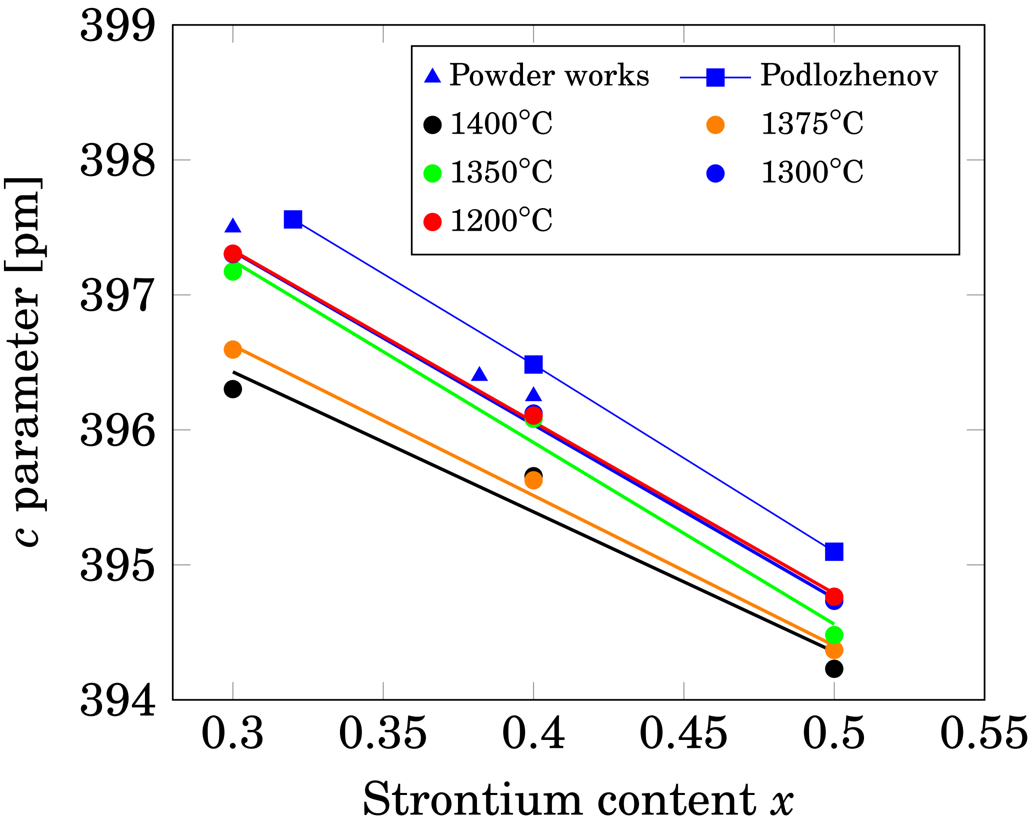

Figure 4.5: Measured c parameters (marked with circles) plotted together with reported unit cell parameters. The data is plotted for a shorter range of strontium content to highlight the variations with respect to sintering temperature. The reported data are from Nikasch & Gobbels, Aamlid and Podlozhenov [24, 30, 31], where a trend line is added for Podlozhenov's data.

4.1.3 Unit cell volume

In Figure 4.7, the unit cell volume for SBN30, SBN40 and SBN50 is presented together with the unit cell parameters for increasing sintering temperature. The volume has been calculated from the unit cell parameters presented in the same figure. Lines serving as guides for the eye are added to the volume plot to illustrate the trends for increasing sintering temperature. The lines show a reduction in volume as the sintering temperature increases. This is especially evident for SBN30, where all data points follow the illustrated trend line. Both SBN40 and SBN50 have a data point

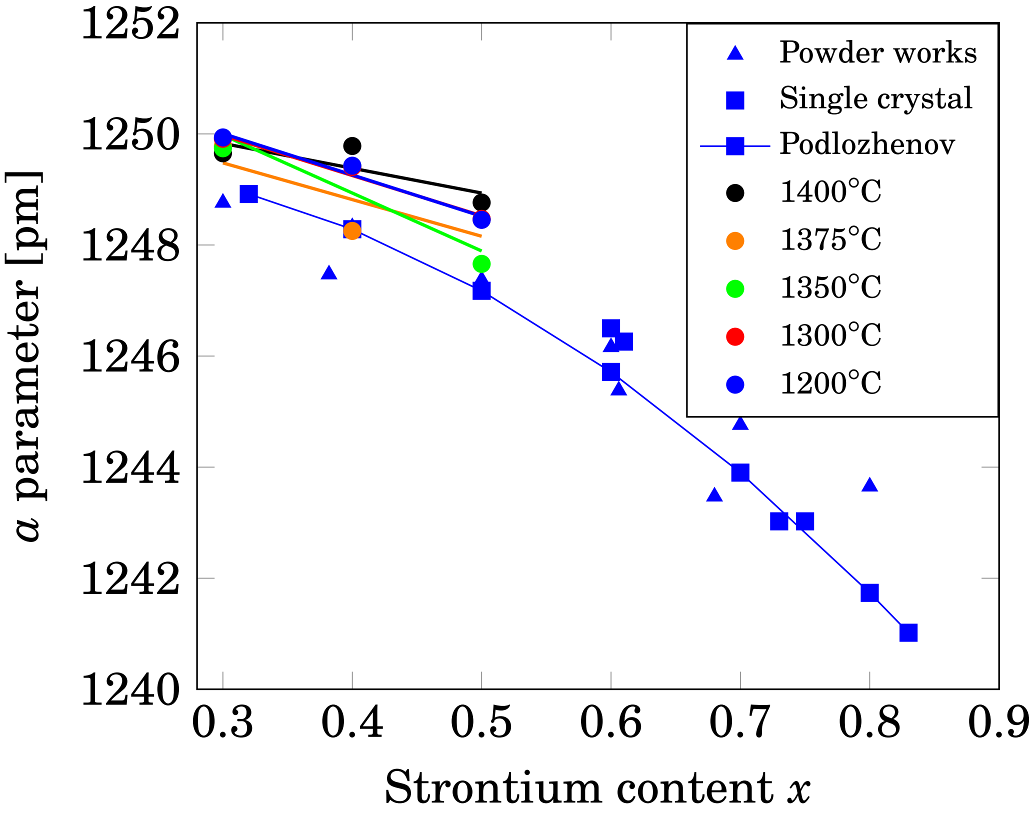

Figure 4.6: Measured a parameters (marked with circles) plotted together with reported unit cell parameters. The reported data are from various sources, with some variations in sample preparation and thermal history. Jamieson, Ballmann & Brown, Podlozhenov, Schefer *et al.* and Oliver & Neurgaonkar [5,24,26,28,29] have used single crystals annealed at 1300-1400°C (marked with squares), while Nikasch & Gobbels and Aamlid [30,31] have used powder samples sintered at 1200°C to 1450°C (marked with triangles). A trend line is added for the data reported by Podlozhenov [24].

laying far off the line, but an overall trend with reduction in unit cell volume could still be suggested. The deviating data points in the volume plot for SBN40 and SBN50 originate from the deviations found in the a parameter for the same samples. Any deviations in the a parameter becomes very pronounced when calculating the unit cell volume. The volume is also decreasing with increasing strontium content. As both the a and c parameter decrease with increasing strontium content, a reduction in unit cell volume is as expected.

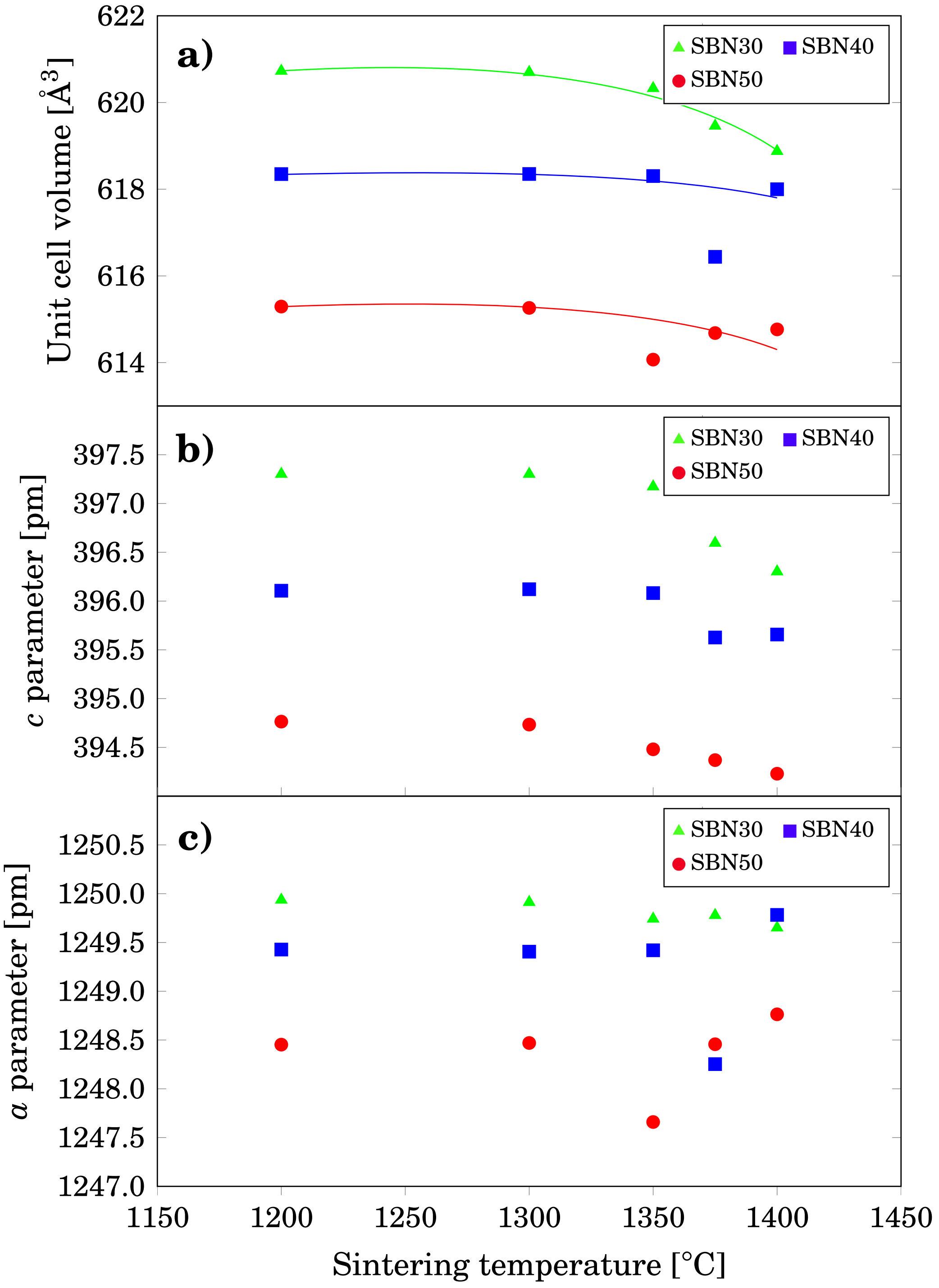

Figure 4.7: a) Unit cell volume for SBN30, SBN40 and SBN50 as a function of sintering temperature. The volume has been calculated based on the a and c parameters plotted in this figure. b) c parameters for SBN30, SBN40 and SBN50, and c) a parameters for SBN30, SBN40 and SBN50, all as a function of sintering temperature.

4.2 The effect of thermal history on dielectric response

4.2.1 Temperature dependency

Figures 4.8 and 4.9 show the real components of the dielectric permittivity of SBN40 and SBN50. The curves in the figures corresponds to samples sintered at 1300°C, 1350°C and 1400°C, recorded with a frequency of 10^2 Hz. The figures show the peak in dielectric permittivity moving towards lower temperatures as the sintering temperature increases. The position of the peak in dielectric permittivity corresponds to the phase transition temperature between the ferroelectric and paraelectric symmetry. The blue curve in Figure 4.8 is corresponding to the sample sintered at 1300°C, and indicates a phase transition at approximately 135°C. This value is in accordance with the reported value of the phase transition temperature of SBN40, as presented in Figure 2.11. The sample sintered at 1350°C has the peak at approximately 95°C, whereas the 1400°C sample indicates a phase transition at approximately 35°C. The phase transition temperature seems to shift 100°C as a result of the increase in sintering temperature. In comparison is the same shift in phase transition temperature found when the strontium content is changed from 40% to 75%. The temperature induced shift in Curie temperature is thus quite substantial.

The same behavior, although not as distinct, is found for SBN50 and presented in Figure 4.9. The blue line in the figure indicate a phase transition at approximately 90°C, which is in accordance with the Curie temperature reported in the literature. As the sintering temperature is increased from 1300°C, the Curie temperature shifts towards lower temperatures. The peak in dielectric permittivity is located at approximately 50°C and 70°C for the samples sintered at 1350°C and 1400°C respectively. The phase transition temperature is not changing as consistently as for SBN40, but there is nevertheless some effect of the sintering temperature.

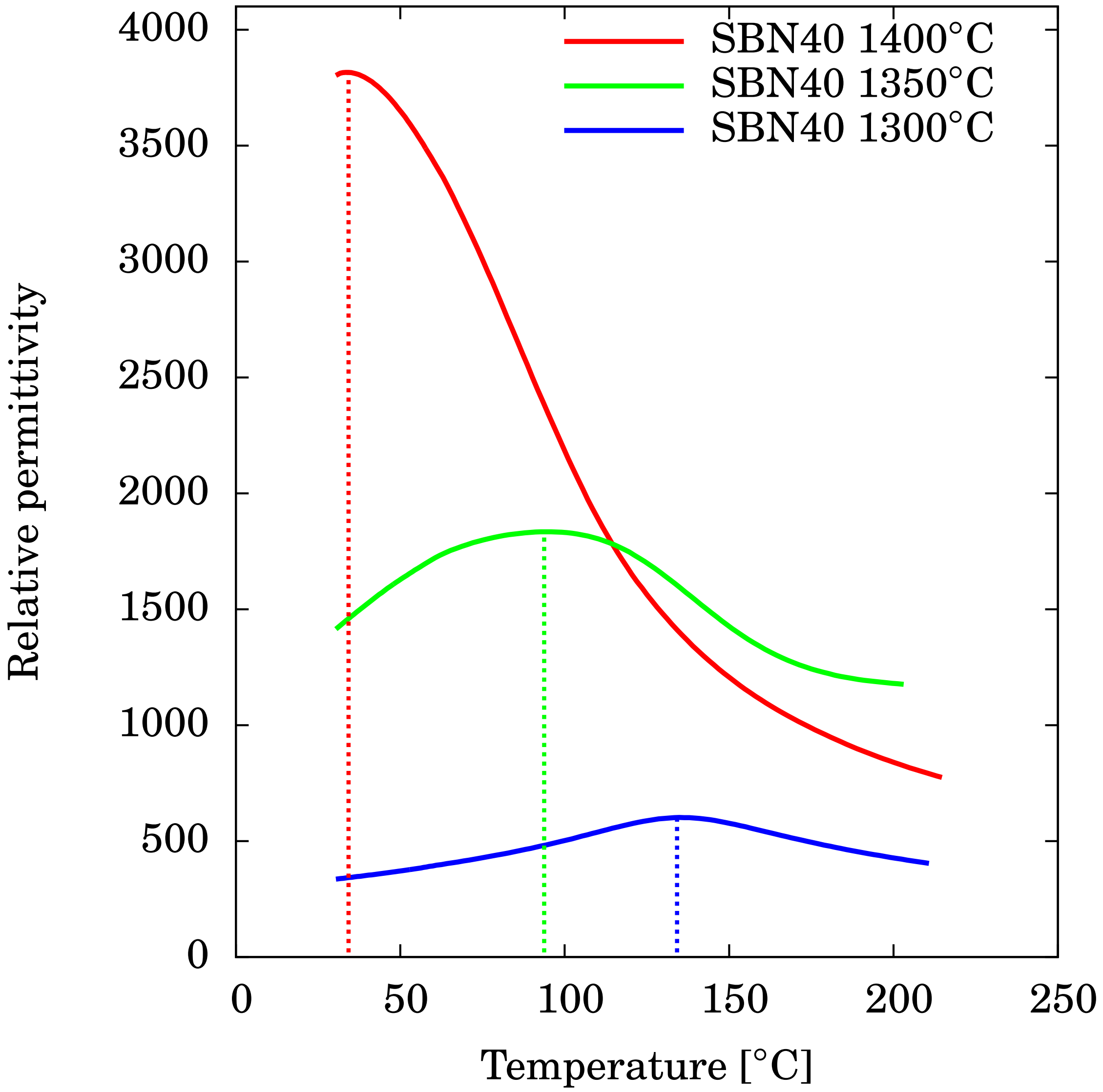

Figure 4.8: Relative dielectric permittivity for SBN40 sintered at 1300°C, 1350°C and 1400°C. The figure show the real permittivity measured during cooling with a frequency of 10^2 Hz. A heating/cooling rate of $2^\circ\,\mathrm{min}^{-1}$ combined with dielectric recordings every 30 seconds yielded results with very good resolution.

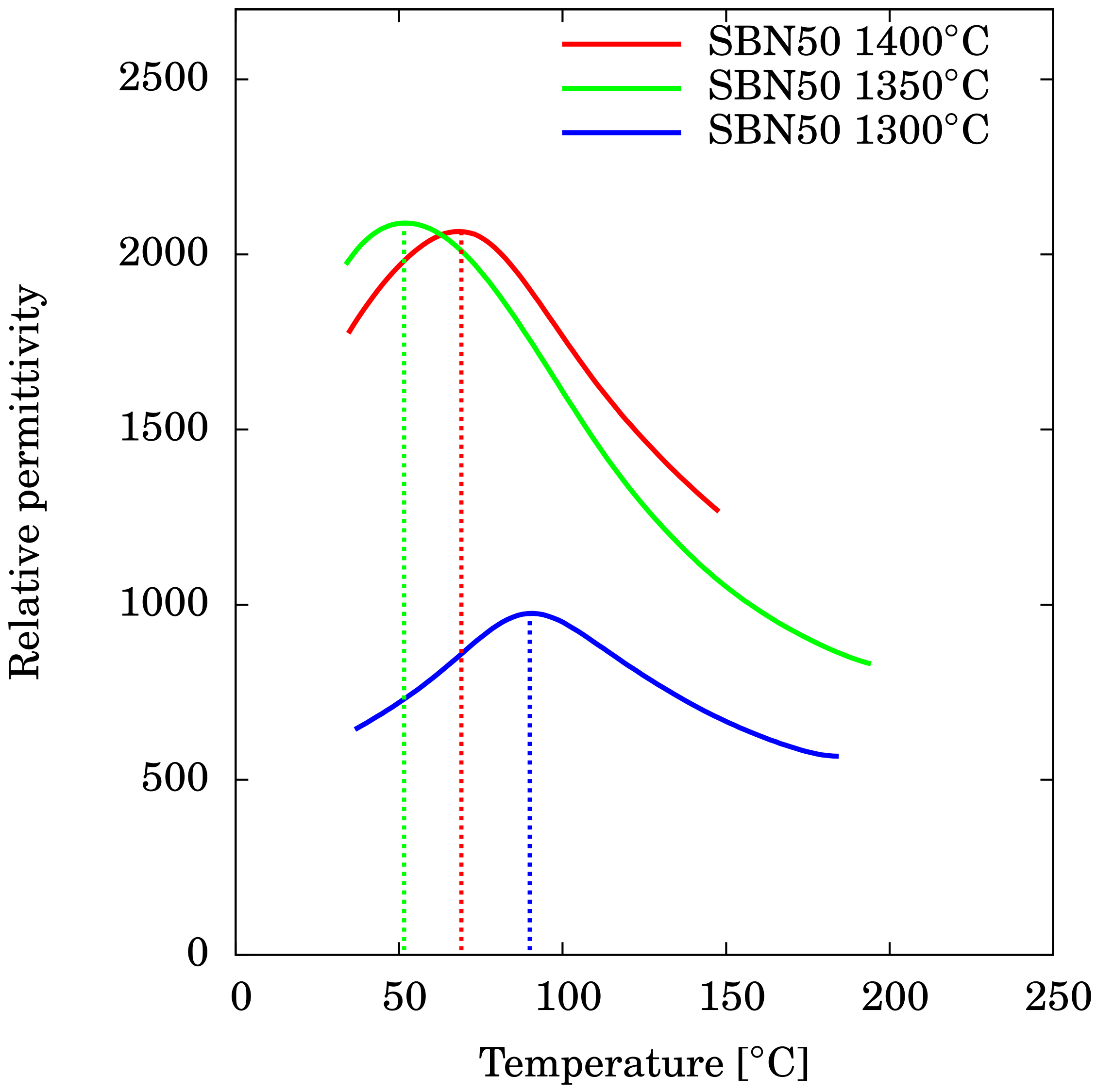

Figure 4.9: Relative dielectric permittivity for SBN50 sintered at 1300°C, 1350°C and 1400°C. The figure show the real permittivity measured during heating with a frequency of 10^2 Hz. A heating/cooling rate of $2° \min^{-1}$ combined with dielectric recordings every 30 seconds yielded results with very good resolution.

4.2.2 Frequency dependency

Figures 4.10 to 4.15 show the dielectric response for SBN40 and SBN50 sintered at 1300°C, 1350°C and 1400°C. The figures show the real component of the dielectric permittivity and the dielectric loss (tan(δ)) recorded in the frequency range of 10^0 to 10^6 Hz. The position of the peak in dielectric permittivity is for some samples showing frequential dependency. Figure 4.10 presents the dielectric response for SBN40 sintered at 1300°C. The two lowest frequencies, 10^0Hz and 10^1Hz, are omitted due to noisy measurements, but the remaining data show no significant dispersion of the dielectric permittivities.This is normal ferroelectric behavior as expected for SBN with 40% strontium. The dielectric response of SBN40 sintered at 1350°C is presented in Figure 4.11, showing measured permittivities dispersed over a range of values. The peak in permittivity is also shifted towards higher temperatures as the frequency increases. Similar behavior is also found for SBN40 sintered at 1400°C, as presented in Figure 4.12.

The dispersion of permittivities and the shift in peak position with increasing frequency is characteristic behavior for relaxor materials. SBN is however not reported to have relaxor properties for the investigated compositions. The shift from normal ferroelectric to relaxor behavior is reported to occur at strontium content of approximately 61% [20]. The investigated samples should thus, according to the literature, behave as normal ferroelectrics and not possess relaxor properties. Nevertheless, the data indicate that a transition from normal to relaxor behavior occur for increasing sintering temperature. This shift in dielectric behavior is also present for SBN50, presented in Figures 4.13 to 4.15. The sample sintered at 1300°C show normal ferroelectric behavior. As the sintering temperature increases, relaxor behavior occurs.

The dielectric loss is expected to be highest for the highest frequencies, and decrease with the frequency. The opposite is expected for the dielectric permittivity, which should be lowest for the highest frequencies, and then increase with decreasing frequency [18]. This is the observed trends for most of the samples. The most significant deviations from such behavior are present for the samples sintered at 1300°C. The deviation described for SBN40 sintered at 1300°C is also present for SBN50 sintered at the same temperature. The two lowest frequencies give a very high dielectric loss for both samples.

The dielectric loss for SBN40 sintered at 1400°C was not measured correctly and has been omitted from the plot in Figure 4.12.

SBN40 sintered at 1300°C

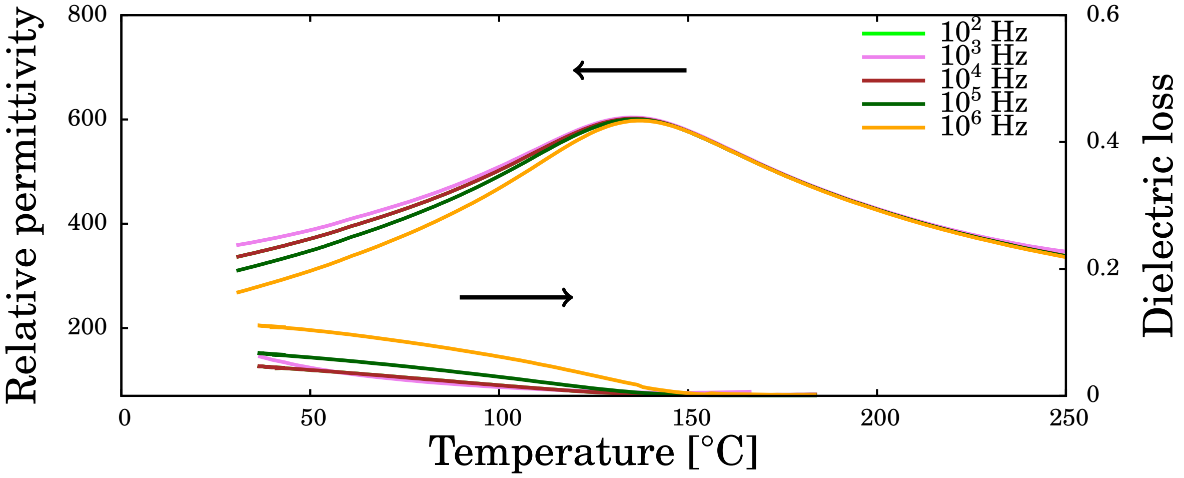

Figure 4.10: Dielectric response of SBN40 sintered at 1300°C. The upper set of curves is the dielectric permittivity. The lowest set of curves is the dielectric loss. Some frequencies have been omitted due to noisy measurements, and some curves have been cut for plotting convenience.

SBN40 sintered at 1350°C

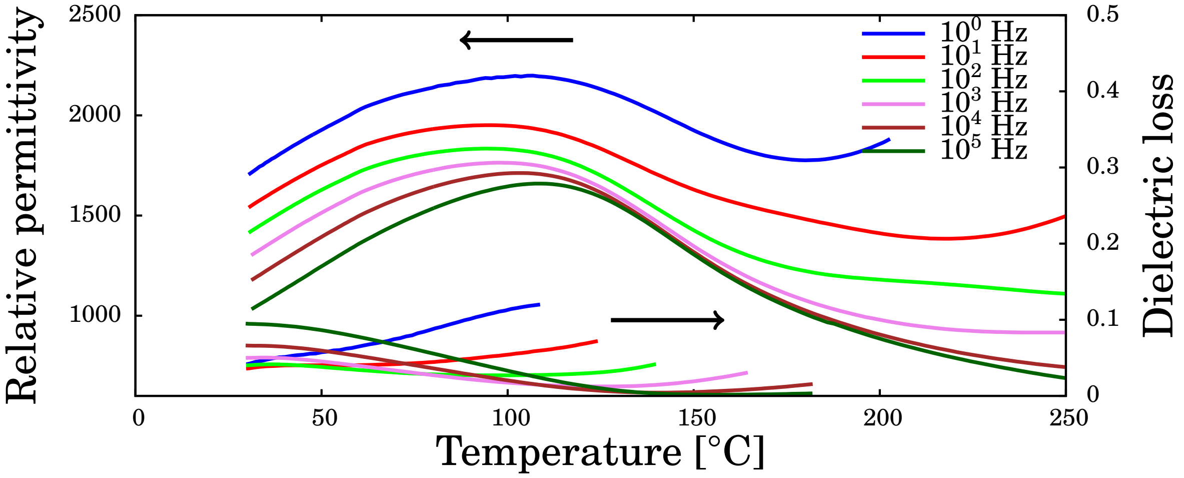

Figure 4.11: Dielectric response of SBN40 sintered at 1350°C. The upper set of curves is the dielectric permittivity. The lowest set of curves is the dielectric loss. The curve corresponding to 10^6Hz has been omitted due to noisy measurements. Some of the curves have been cut for plotting convenience.

SBN40 sintered at 1400°C

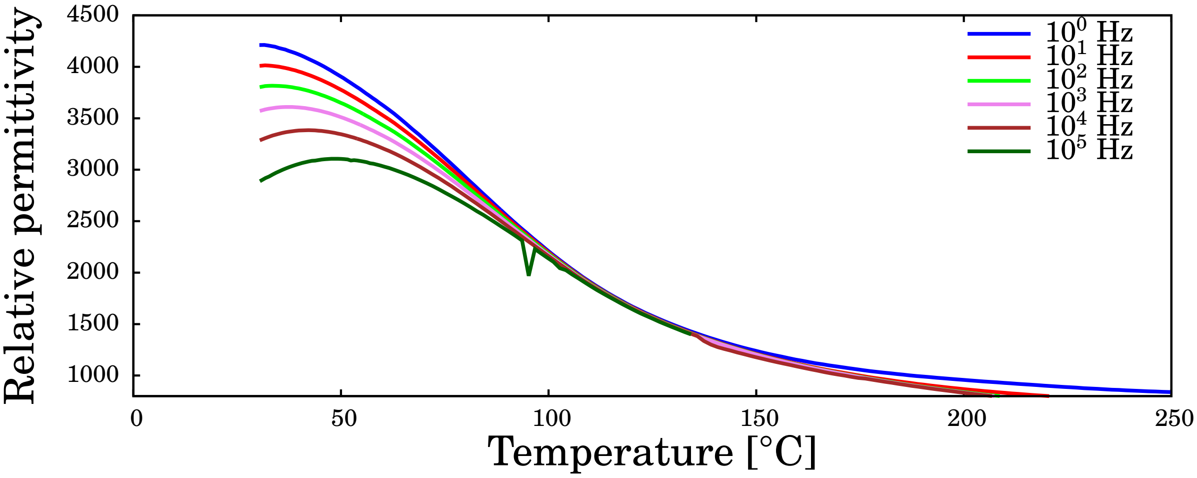

Figure 4.12: Dielectric response of SBN40 sintered at 1400°C. The plotted set of curves is the dielectric permittivity. The dielectric loss is omitted from the figure due to poor and noisy measurement. The dielectric permittivity for 10^6Hz has been omitted for the same reason.

SBN50 sintered at 1300°C

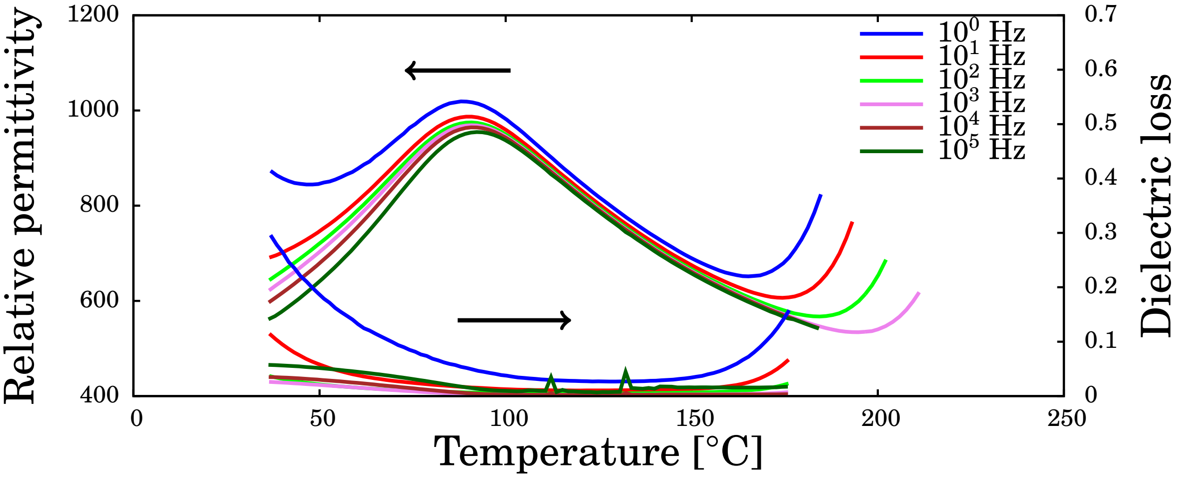

Figure 4.13: Dielectric response of SBN50 sintered at 1300°C. The upper set of curves is the dielectric permittivity. The lowest set of curves is the dielectric loss. The curves corresponding to 10^6Hz has been omitted due to noisy measurements. Some of the curves have been cut for plotting convenience.

SBN50 sintered at 1350°C

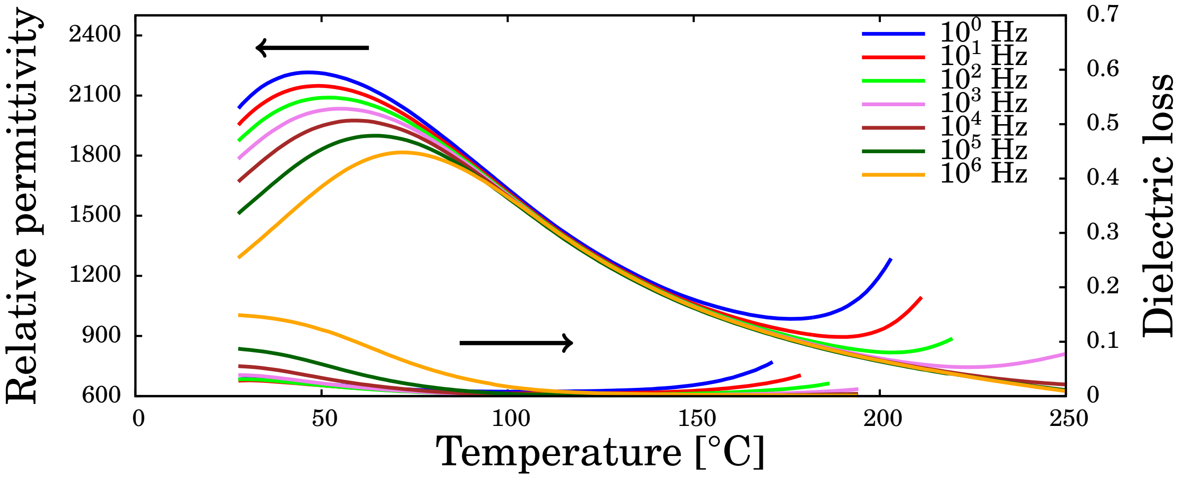

Figure 4.14: Dielectric response of SBN50 sintered at 1350°C. The upper set of curves is the dielectric permittivity. The lowest set of curves is the dielectric loss. Some of the curves have been cut for plotting convenience.

SBN50 sintered at 1400°C

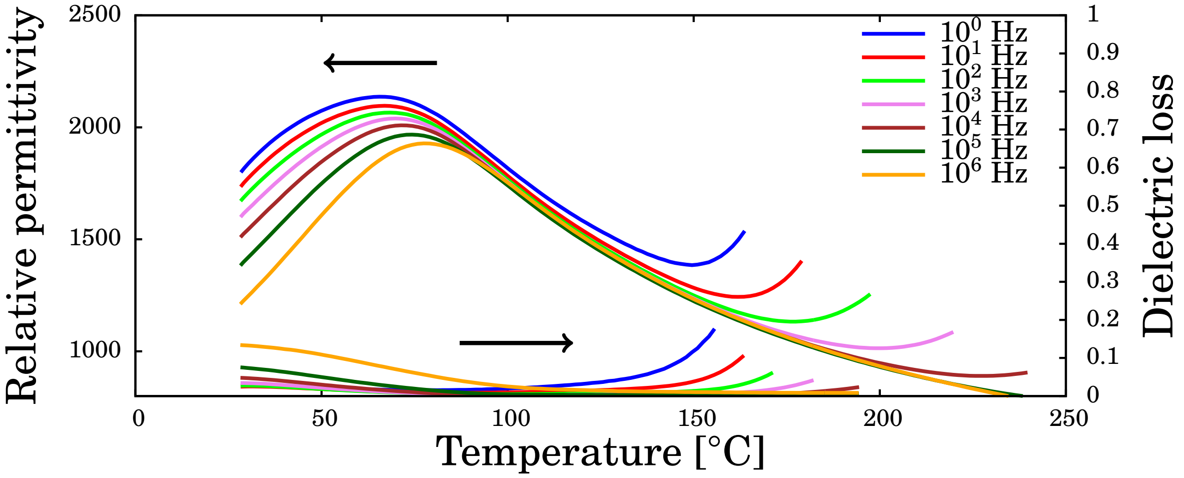

Figure 4.15: Dielectric response of SBN50 sintered at 1400°C. The upper set of curves is the dielectric permittivity. The lowest set of curves is the dielectric loss. Some of the curves have been cut for plotting convenience.

4.3 Temperature dependency of crystal structure

4.3.1 Changes with sintering temperature

SBN30 sintered at 1300°C and 1350°C were analyzed through HT-XRD in the temperature range of 30°C to 440°C. Based on the diffractograms the unit cell parameters were found through Pawley fitting in Topas. The variation in unit cell parameters as a function of temperature is presented in Figures 4.16 and 4.17. The reported Curie temperature for SBN30 is indicated with a vertical, dotted line in Figure 4.16, and seems to be coinciding with the phase transition temperature indicated by the samples. As the temperature is approaching the Curie temperature the c parameter decreases. This is expected behavior during the phase transition as the polarization is lost causing the polar c axis to contract. When the phase transition is complete, the c parameter is increasing due to thermal expansion. The characteristic behavior measured for both samples coincide with reported data for the phase transition [26].

There are two points to note from the c parameter plotted in Figure 4.16. At temperatures below 100°C, the c parameter is flattening out at different values for the two samples. The two levels are indicated with horizontal, dotted lines in Figure 4.16. The measured c parameter is for the sample sintered at 1350°C mostly smaller compared to the sample sintered at 1300°C. This coincides trend coincides with the measurement presented in Figure 4.4, with decreasing c parameter for increasing sintering temperature. The c parameter associated with the sample sintered at 1350°C is also shifted to the left during the c axis' contraction. This indicates a shift in phase transition temperature towards lower temperatures for the sample sintered at 1350°C. Both the HT-XRD experiments and the dielectric spectroscopy are thus indicating a shift towards lower Curie temperature as the sintering temperature increases.

4.3.2 Compositional dependency

SBN30, SBN40 and SBN50, all sintered at 1400°C, were analyzed in the temperature range between 30°C and 215°C. The results from the sample with 30% strontium was not satisfactory, and has been replaced by the sample sintered at 1350°C from the first HT-XRD experiment. The unit cell parameters were found through Pawley fitting in Topas and presented in Figures 4.18 and 4.19 together with literature values. In Fig-

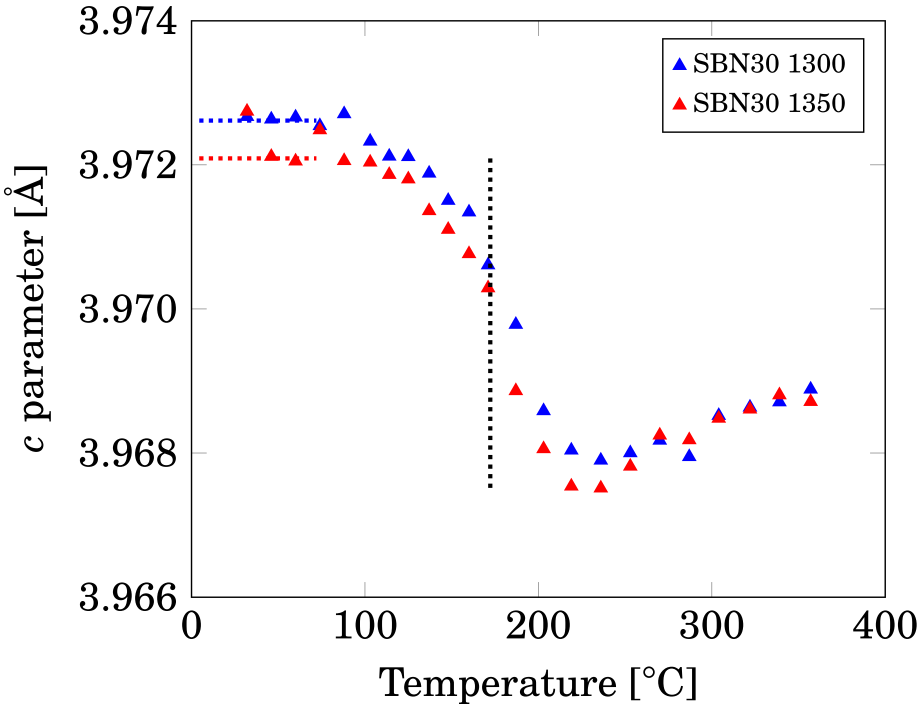

Figure 4.16: Comparison of c parameter of SBN30 sintered at 1300°C and 1350°C

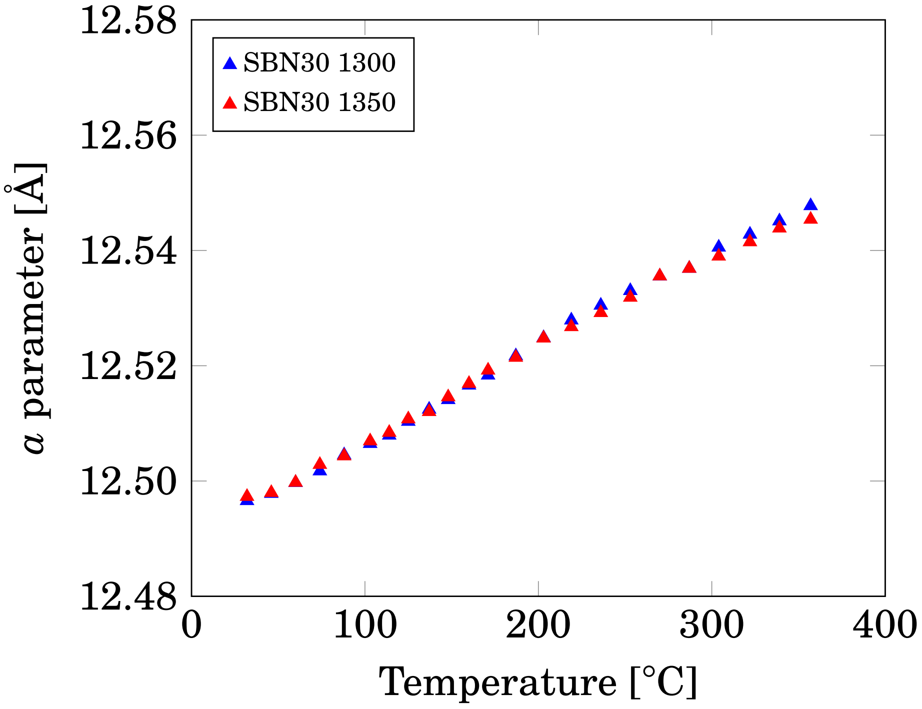

Figure 4.17: Comparison of a parameter of SBN30 sintered at 1300°C and 1350°C

ure 4.19, the reported Curie temperatures are indicated by vertical, dotted lines for each composition. The unit cell parameters for SBN are very dependent of the strontium content of the sample, as seen by the shift between each sample. The measured unit cell parameters are in accordance the reported values for each composition [24].

The compositional dependency of the unit cell parameters is to some degree linear with respect to strontium content as shown in Figure 2.10. For strontium content in the range of $20\% - 40\%$, a deviation from linearity occur. Between each series of unit cell parameters, a shift reflects the changes in strontium content between the samples. The shift in c parameters should be more or less the same between all samples, i.e. the shift from SBN61 to SBN50 should be equal to the shift from SBN50 to SBN40 [24]. This is as expected. The deviation from linearity results in smaller shifts in a parameters as the strontium content is reduced. This is in accordance with the observed shifts in Figure 4.18. The measured unit cell parameters are within reasonable range of reported values. The dependencies with respect to temperature and composition are also as expected.

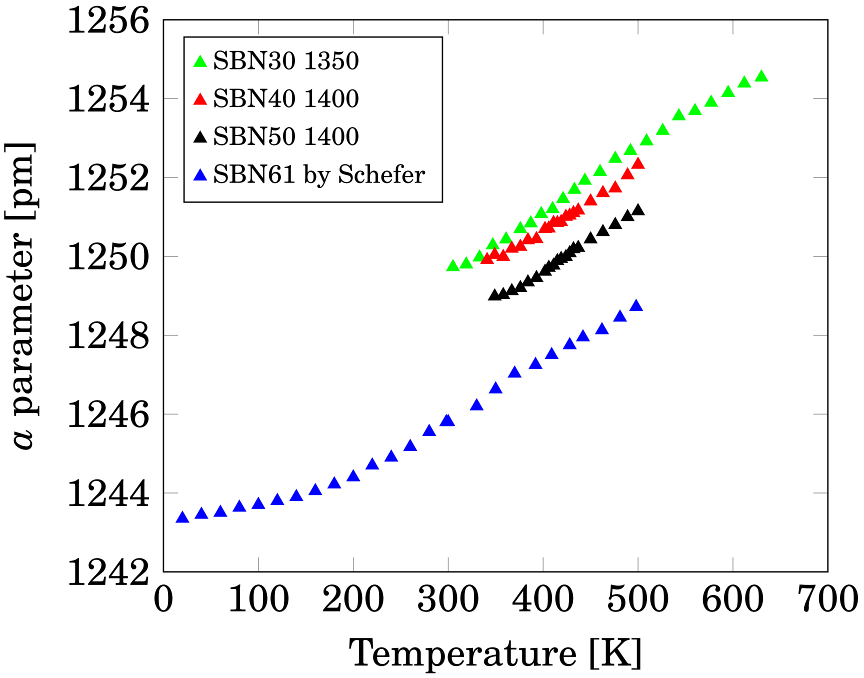

Figure 4.18: The a parameter for SBN30 sintered at 1350°C, and SBN40 and SBN50 sintered at 1400°C plotted together with data reported by Schefer *et al.* [26].

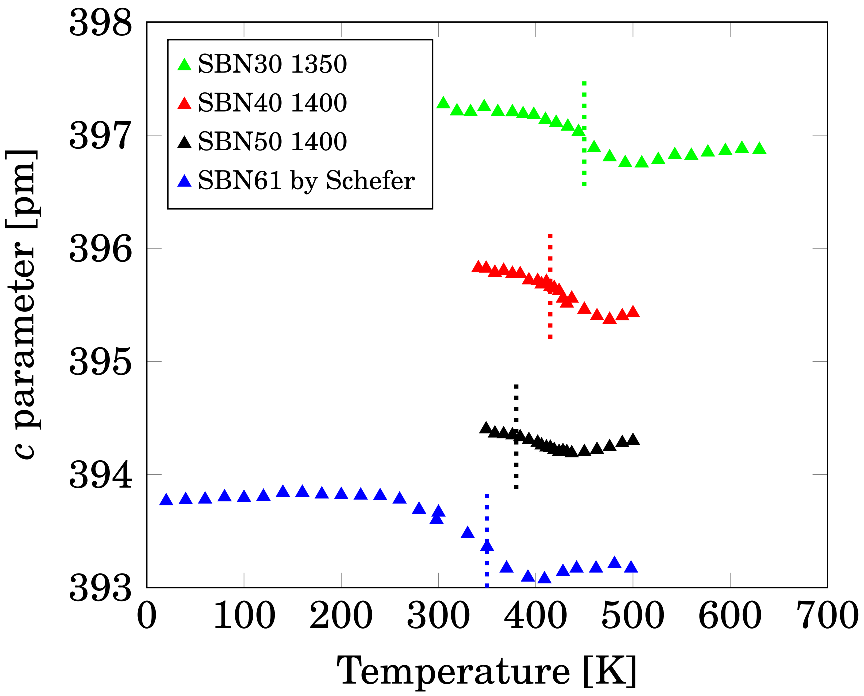

Figure 4.19: The *c* parameter for SBN30 sintered at 1350°C, and SBN40 and SBN50 sintered at 1400°C plotted together with data reported by Schefer *et al.* [26].

4.4 Structural refinement

4.4.1 Resolving the structure

The Rietveld refinements were performed as described in the methods section. The refined results for SBN30 sintered at 1300°C are presented in Table 4.2 and Figure 4.20. The rest of the refined results are found in Appendix B. Figure 4.20 show observed and calculated intensities, in addition to the calculated differences. Table 4.2 present the crystallographic information obtained for the refined structure. It was possible to obtain suitable fits for all samples, except for SBN50 sintered at 1350°C. This sample is therefore omitted from the results. All other samples resulted in refinements with corresponding Rwp values ranging from 8.5 to 9.5, as presented in Table 4.1.

Table 4.1: Rwp values for the Rietveld refinements performed in Topas.

Sample	Sintering temperature [°C]	Rwp value
SBN30	1300	8.719
SBN30	1350	9.353
SBN30	1400	9.455
SBN40	1300	8.417
SBN40	1350	8.461
SBN40	1400	9.272
SBN50	1300	8.482
SBN50	1400	8.889

4.4.2 SBN30 sintered at 1300°C

Table 4.2: Structural data for SBN30 sintered at 1300°C found through Rietveld refinement in Topas.

Position	Atom	Mp.	x	y	z	Occ.	B_{iso}
A2	Ba	4	0.1725	0.6725	0.4539	0.8731	1.454
A2	Sr	4	0.1725	0.6725	0.4539	0.0287	2.140
A1	Sr	2	0	0.0	0.4909	0.6926	0.5593
A1	Ba	2	0	0.0	0.4909	0.0039	1.050
Nb1	Nb	2	0	0.5	0.9803	1	0.7278
Nb2	Nb	8	0.0739	0.2108	0.9699	1	0.6703
O1	O	4	0.2826	0.7826	0.0238	1	0.17
O2	O	8	0.1417	0.0674	0.9103	1	2.45
O3	O	8	0.3399	0.0060	0.9025	1	2.41
O4	O	8	0.2929	0.4269	0.4623	1	3.65
O5	O	2	0	0.5	0.4744	1	4.87

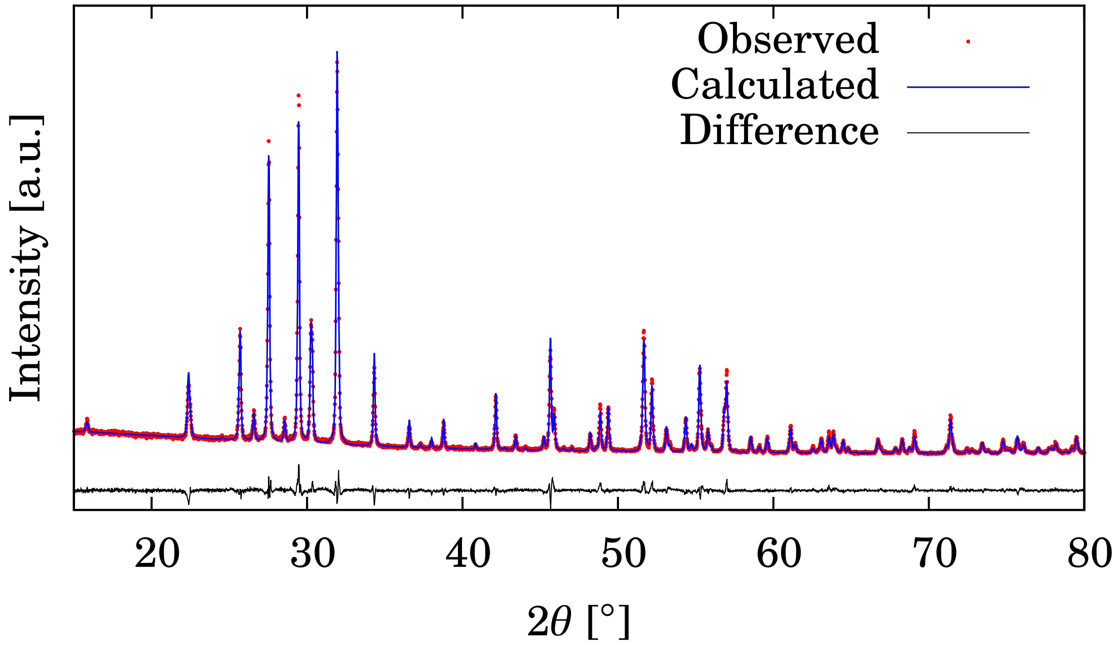

Figure 4.20: Results from Rietveld refinement of SBN30 sintered at 1300°C. The calculated pattern was fitted to the observed diffractogram with a Rwp value of 8.719.

4.4.3 Cation occupation at A1 and A2

The occupancy of strontium and barium at the A1 and A2 sites have also been extracted from the Rietveld refinements. The data are presented in Figures 4.21 to 4.23. The absolute values of the site occupancies show some variations with respect to sintering temperature. However, the error bars associated with the data points are significantly larger than the variations between the samples. It is therefore difficult, based only on these refinements alone, to infer how the site occupancies of strontium and barium changes with respect to sintering temperature. During the refinements some samples showed no sign of barium occupancy at the A1 sites. The occupancy was therefore fixed to zero and not refined upon during the rest of the refinement. As a result has the barium occupancy at A1 for some samples either been plotted without error bars (SBN40) or omitted completely (SBN50).

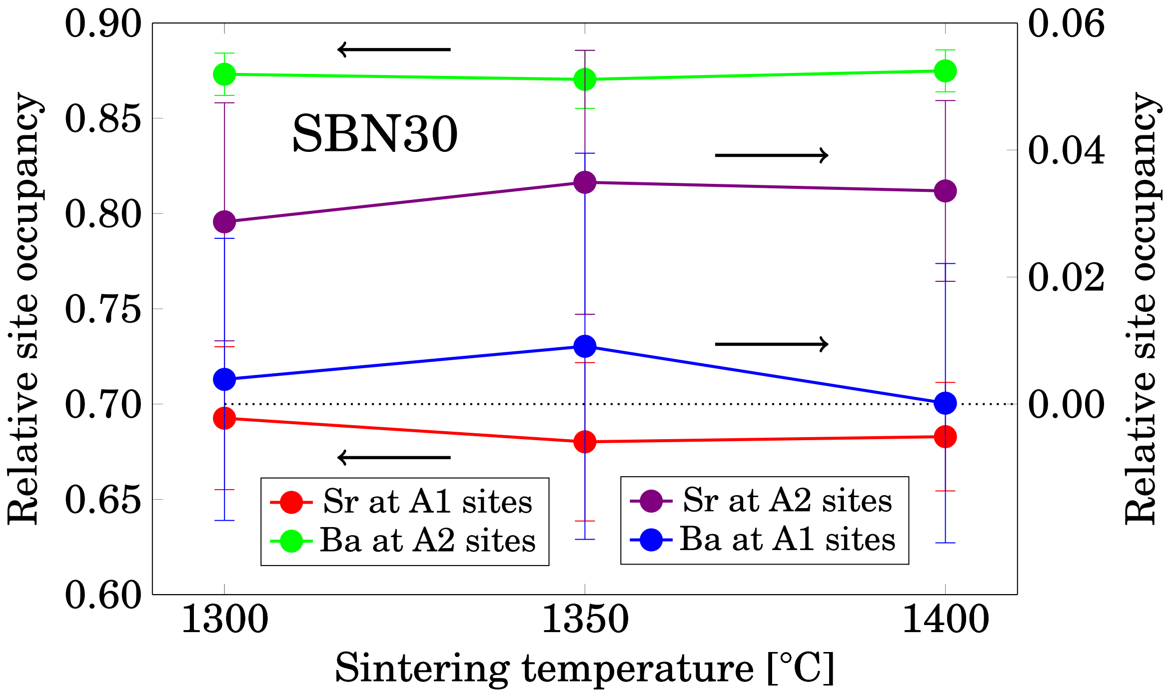

Figure 4.21: Site occupancies of strontium and barium at A1 and A2 sites for SBN30.

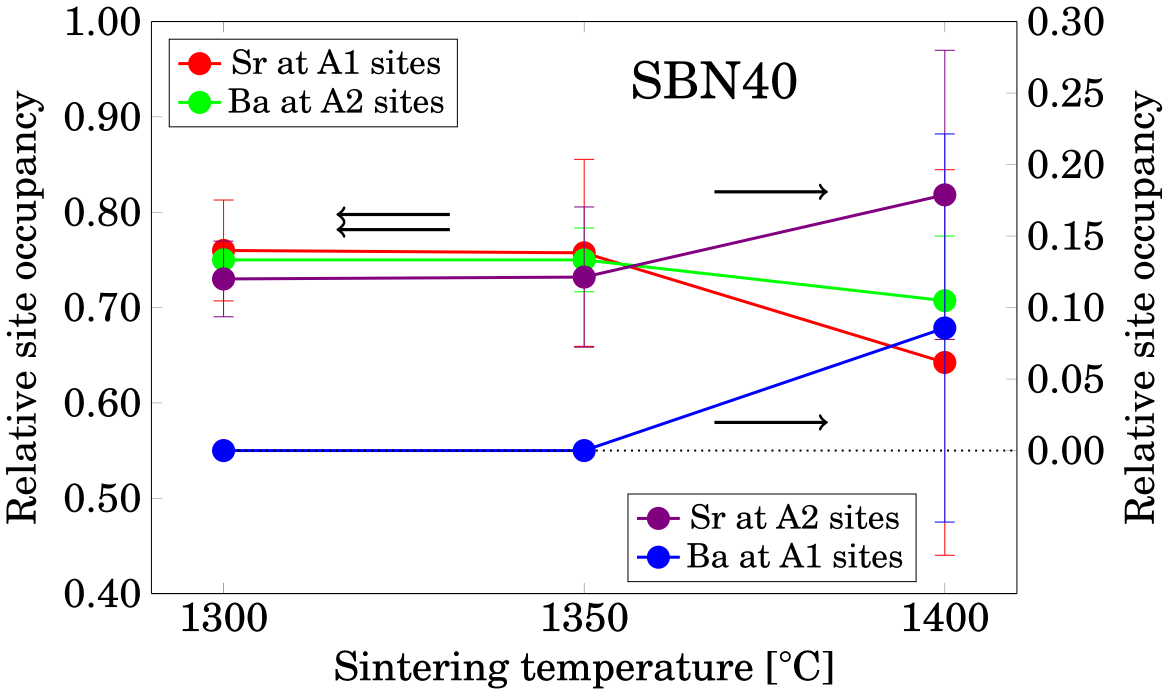

Figure 4.22: Site occupancies of strontium and barium at A1 and A2 sites for SBN40.

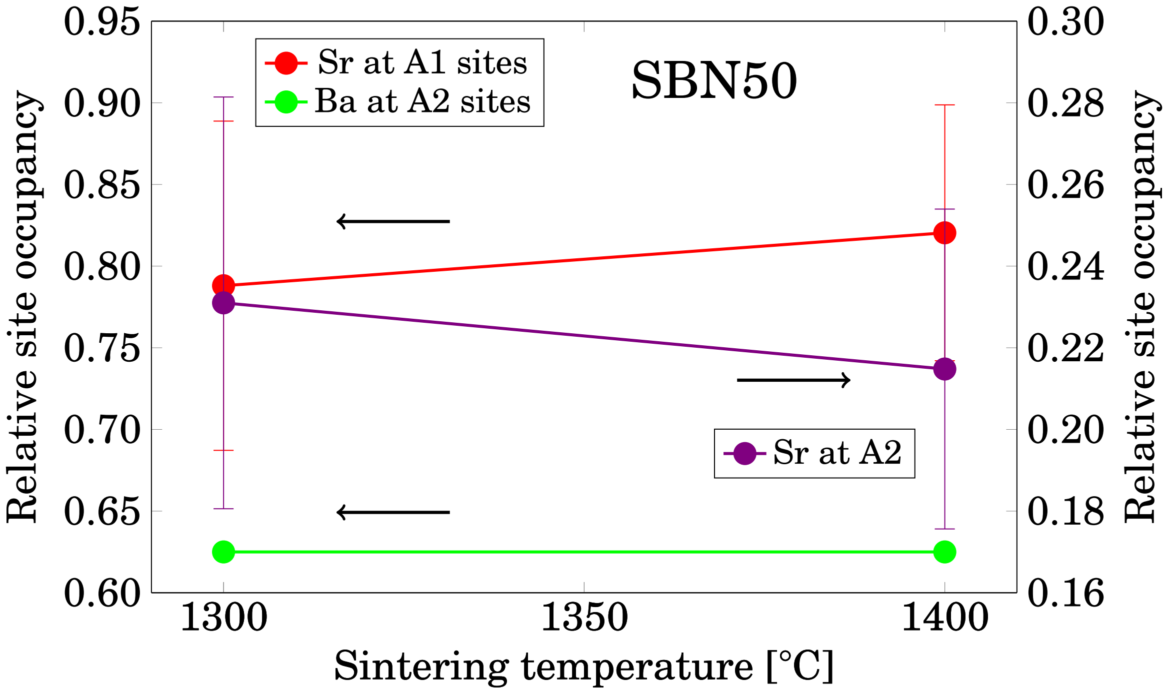

Figure 4.23: Site occupancies of strontium and barium at A1 and A2 sites for SBN50.

4.5 Density measurements

Prior to dielectric measurements, the densities of the samples were measured. Table 4.3 presents the relative density of the samples. The samples sintered at 1350°C and 1400°C are within the range of 96 to 98%. The lowest sintering temperature did not result in samples with equally high density. This could be related to low mass transport kinetics within the sample at reduced temperatures.

Table 4.3: Relative densities for the samples used in the dielectric measurements.

Sample	Sintering temperature [°C]	Relative density [%]
SBN40	1300	68.0
SBN40	1350	97.0
SBN40	1400	98.1
SBN50	1300	73.9
SBN50	1350	96.3
SBN50	1400	97.3

Chapter 5

Discussion

5.1 Structural dependency on thermal history

5.1.1 X-ray intensities

Figure 4.1 show X-ray diffractograms for SBN30, SBN40 and SBN50 sintered at various temperatures. Some peaks show a dependency of thermal history, while others are not affected at all. This is especially evident for SBN50 in Figure 4.1, showing that the intensity variations are clearly not equal for all reflections. The fact that some reflections are gaining while others are loosing intensity, suggests a more site or cation specific change. The structure factors governing peak intensity in the diffractogram are very dependent on the mass of the cation occupying the site [47]. If a cation is moving from one site to another, switching place with a vacancy, it should be possible to observe the interchange in the X-ray diffractograms. Since some reflections clearly are gaining intensity, it could be related to a cation taking the place of a vacancy. This process would increase the reflecting properties of the related site, and thus cause the intensity to increase. At the other site, where a vacancy is replacing a cation, a corresponding reduction in intensity would be expected. The peak behavior as a function of sintering temperature could thus be explained by cation/vacancy interchanges within the crystal structure. Whether it is barium or strontium causing these variations is difficult to infer based on these results alone. However, variations caused by barium moving from A2 to A1, as shown in Figure 2.13, is expected to increase with reducing strontium content. This compositional dependency is not found. The intensity variations observed in Figure 4.1 are greatest for SBN50 and not very pronounced for SBN30 and SBN40.

Another thing to observe is the apparent overall reduction in peak intensity with increasing temperature, especially for SBN30 and SBN40. A possible reason for this behavior is a variation in crystallite size from sample to sample. The higher the sintering temperature is, the harder the samples become, making them more difficult to crush into fine grained powder. The crystallites are most likely larger in size and fewer in number for the samples sintered at 1400°C. This results in less reflected X-rays and less intensity for a given peak, compared to the samples sintered at 1350°C.

5.1.2 Shift in peak position

In addition to the changes in peak intensity, some peaks show a shift in peak position for increasing sintering temperature. The degree of shift in peak position is however not constant for all peaks. Some peaks show a significant shift towards higher 2θ values for increasing sintering temperature, while others do not shift at all. For SBN30, the shift is most apparent for the peaks indicated with black arrows in Figure 4.2. The same behavior is observed for SBN50 shown in Figure 4.3. It is more or less the same peaks shifting for both compositions. This is also the same peaks showing significant change in intensity for the samples with 50% strontium content. Changes in 2θ position for a given peak are only affected by variations in unit cell parameters. The fact that the degree of positional shift is not equal for all peaks, suggests that the various peaks are not equally dependent on the a and c parameter. The c parameter undergoes a clear decrease for increasing sintering temperature, while the a parameter increases but not with the same clear thermal dependency. The shifts in peak position are thus a reflection of the changes observed for the unit cell parameters for increasing sintering temperature. The observed shifts suggests that the shifted peaks are more dependent on the c parameter than the other peaks.

The degree of positional shift is not equal for the two compositions, where the peaks related to SBN30 are shifted more compared to those of SBN50. For SBN30 in Figure 4.2, all peaks are subject for some degree of positional shift. The arrows are only indicating the peaks shifting the most. The samples with 50% strontium do however not show a general shift for all peaks, but only for the ones indicated with arrows. This compositional dependency suggests that the barium to strontium ratio in the samples affects the degree of positional shift. As discussed above, the probability of barium moving from A2 to A1 should be dependent on the amount of barium in the structure. Barium inversion could thus be a possible explanation for the observed shifts in peak position.

Another possible source of shift in peak position is sample displacement, caused by improper sample preparation. A shift caused by sample displacement is proportional to cos(θ) [48]. The shift should thus be highest at low angles and steadily decrease as the angle increases. The shift is however present for all 2θ values in the investigated range, and not diminishing for higher 2θ values. The degree of rightward shift is also changing from peak to peak, indicated by arrows in Figures 4.2 and 4.3, and not steadily decreasing with the angle. The variations in peak position could thus not be explained by sample displacement, but instead support the suggestion of changes in crystal structure.

5.1.3 Unit cell parameters

Dependency on thermal history

Figures 4.4 to 4.6 show the variation in unit cell parameters as a function of increasing sintering temperature. The measured c parameter is clearly affected by the thermal history, showing a distinct decrease as the sintering temperature increases. The measured a parameter is larger than the reported values. Figure 4.6 shows a tendency for increasing a parameter for increasing sintering temperature, but the dependency is not as distinct as for the c parameter. Increasing sintering temperature causes the unit cell to contract along the c axis while it expands within the ab plane.

The decrease in c parameter is however not equal for all three compositions. As presented in Figure 5.1, the samples with lower strontium content are subject to a greater change in c parameter than the two other compositions. The c parameter for SBN30 decreases approximately 0.01 Å during an increase in sintering temperature from 1300°C to 1400°C. The samples with 50% strontium are in comparison decreasing approximately 0.006 Å for the same temperature increase. Again is the degree of change caused by variations in thermal history dependent on the strontium content of the sample. These observations coincide with the hypothesis of temperature induced barium inversion.

Cation movement

The unit cell parameters are also changing with respect to strontium content, as reported in the literature and shown in Figure 2.10. When the amount of strontium in the solid solution is increased, the barium content is decreasing correspondingly.

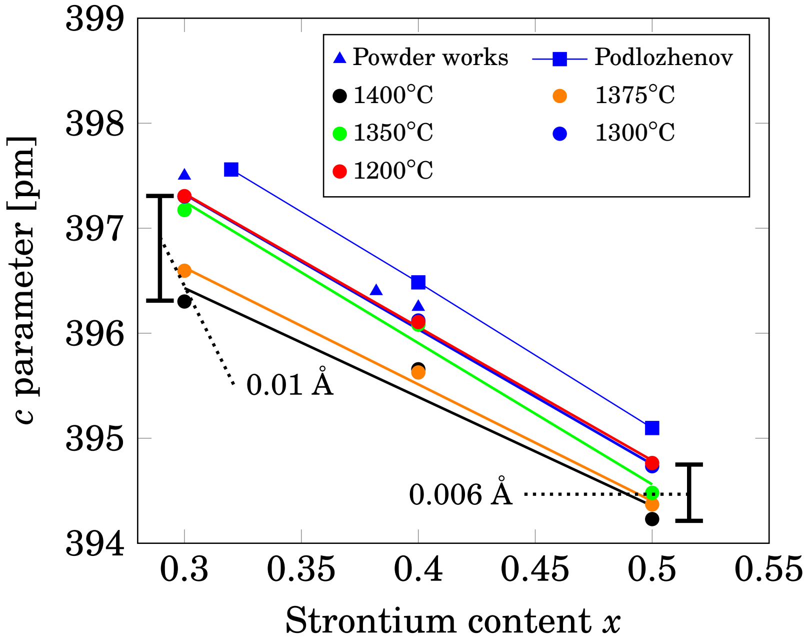

Figure 5.1: Measured c parameters as presented in Figure 4.4. The decrease in c parameter induced by increased sintering temperature are indicated for SBN30 and SBN50.

The interchange of barium with strontium cations is mostly affecting the relative occupancy of the A2 sites, as illustrated in Figure 2.9. As the strontium content is increased, the relative occupancy of strontium at the A2 sites is increasing, at the expense of the barium occupancy at the same site. Due to the difference in ionic radii between the two cations, both a and c parameters are decreasing as the strontium content increases. These changes in both a and c parameters are approximately 0.10 Å within the range of 30% to 80% strontium content, as seen in Figure 2.10. The variation in c parameter induced by increased sintering temperature is approximately 10% of the decrease caused by increasing strontium content. The compositional dependency of the unit cell parameters does not seem to be changing as the sintering temperature is increased. The trend lines in Figure 4.5 are very similar for all sintering temperatures. The size reducing mechanism of strontium replacing barium in the structure seems to be unaffected of the structural changes induced by an increase in sintering temperature.

One significant difference between the composition and temperature dependent changes in unit cell parameters, is the direction of the change in a parameter. The a parameter is reduced as the strontium content is increased. On the other hand is the a parameter increased when the sintering temperature increases. The mechanism behind the temperature dependent change in unit cell parameters seems to differ from the rather straightforward replacement of barium with strontium at the A2 site. Figure 2.9 shows the relative occupancies of the A1 and A2 sites as a function of strontium content. The relative occupancy of strontium at the A1 sites is not very dependent on the overall strontium content. The change of unit cell parameters as a function of strontium content is thus only involving cation replacement at the A2 site.

Two scenarios could be used to explain the changes induced by increasing sintering temperature. 1) The barium cations are still fixed to the A2 sites while the strontium distribution between the A1 and A2 sites is changed, or 2) the barium cations are allowed to move between the A2 and A1 sites along with the strontium cations. Both scenarios involve cation movement to or from the A1 site. Cations moving from A2 to A1, whether it is barium or strontium, would leave a vacancy at the A2 site. This process is similar to the replacement of barium with strontium, in the sense that there is a reduction in occupied space at the site. The vacancy occupies obviously less space than the cation, causing the site to contract. Based on the similarities with the mechanism behind the compositional dependency, this process alone should cause both parameters to decrease. The a parameter is however not decreasing, suggesting another mechanism being effective. The cation leaving the A2 site is not disappearing from the structure and has to enter the A1 site. The vacancy formerly located at the A1 sites is now replaced with a strontium or barium cation. This should, based on the same arguments as above, cause the site to expand. An expansion of the A1 site seems to mostly affect the a parameter. If the c parameter is affected, the impact is still much less than for the a parameter. The involvement of the A1 sites could thus be a possible explanation for the contradicting behavior of the a parameter. Why the A1 sites has a greater impact on the a parameter is however not easily explained. Which of the cations moving from the A2 to A1 sites in this process is also difficult to determine based on these results alone. The increasing change with reducing strontium content could however be used to support the suggestion of barium inversion.

5.1.4 Unit cell volume

Unit cell volume for SBN30, SBN40 and SBN50 has been calculated from the unit cell parameters and are presented in Figure 4.7. For increasing sintering temperature the volume seem to be decreasing for all three compositions, being especially evident for SBN30. Compounds evaporating from the structure could cause a change in unit cell volume. This is however not very likely due to the very low volatility of BaO and SrO at sintering conditions [34]. Nb_2O_5 is more volatile than the two other oxides but is still assumed not to evaporate from the structure during synthesis. A more possible explanation for the reduction in volume is a cation rearrangement within the unit cell, as discussed above. The reduction in unit cell volume is more pronounced for SBN30 compared to the two other compositions. The unit cell volume is calculated from the measured unit cell parameters. Any major deviations in the parameters could thus be found in the calculated volume. As shown in Figure 4.7, some of the measured a parameters are very low compared to the other values of the same composition. This is the case for SBN40 sintered at 1400°C and SBN50 sintered at 1350°C, and reflected in the corresponding unit cell volume. The compositional dependent response in unit cell volume reflects the trend found for the unit cell parameters. As the strontium content decreases, the observed effect from changes in thermal history increases in magnitude and becomes clearer.

5.1.5 Cation occupation

Figures 4.21 to 4.23 show the change in cation occupancy at the A1 and A2 sites. The figures show some variations in occupancy as the sintering temperature increases. The error bars are however much larger than the variations from sample to sample, and it is difficult based on these results alone to comment on whether the change is real or not. However, supported by the X-ray diffractograms and the unit cell parameters the variations become much more reliable. The main point to note from these results is the occupation of barium at the A1 site. SBN50 presented in Figure 4.23, show no sign of barium at the A1 site. However, as the strontium content decreases the trend changes. Samples of SBN40 sintered at 1400°C indicate a possibility of having barium at the A1 site. This is not the case for the SBN40 samples sintered at 1300°C and 1350°C. By reducing the strontium content even more, SBN30 show that barium could be present at the A1 site for all three sintering temperatures. The barium occupancy at A1 for the sample sintered at 1400°C is however too low to be visible in Figure 4.21. The barium occupation at the A1 site could be found in Table B.2.

5.1.6 Structural change – a summary

The combined results from X-ray diffractograms, unit cell parameters and unit cell volume suggest a systematic change in crystal structure as the sintering temperature is increasing. The degree of structural change is dependent on the strontium content in the structure. Both the unit cell parameters, unit cell volume and shift in peak position show larger variations for samples with lower strontium content. The results from the structural investigations indicate that a cation rearrangement is occurring for increasing sintering temperature. Combined with the results from structural refinements is the suggestion of barium inversion at elevated sintering temperatures also supported.

5.2 Thermal dependency of phase transition

5.2.1 Change in transition temperature

The dielectric response for SBN40 and SBN50 has been measured over a range of temperatures, and the results for SBN40 are presented in Figure 5.2. The phase transition from ferroelectric to paraelectric symmetry upon increasing temperature is normally identified with the peak in dielectric permittivity [20]. The observed peaks in dielectric permittivity are not located at the same temperature for all samples with the same composition. The blue line in Figure 5.2, corresponding to the sample sintered at 1300°C, indicates a phase transition temperature of approximately 135°C. This is in accordance with the reported Curie temperature for SBN40 [20, 23]. However, as the sintering temperature increases, the Curie temperature for SBN40 shifts towards lower temperatures. SBN40 sintered at 1350°C has the peak in dielectric permittivity located at approximately 95°C. The peak for SBN40 sintered at 1400°C is located at 35°C. The Curie temperature shifts approximately 100°C by increasing the sintering temperature from 1300°C to 1400°C, as illustrated in Figure 5.2. Similar behavior is found for SBN50 sintered at the same temperatures, presented in Figure 4.9. The increase in sintering temperature induces shift in peak position towards lower temperatures. The shift in peak position as a function of sintering temperature is not equally clear as for SBN40, but the response is nevertheless evident. The dielectric measurements clearly indicate the Curie temperature being dependent on the thermal history of the ceramic sample. Such behavior is to the author's knowledge not previously been reported for this material system.

The height of the peaks in Figure 5.2 are not equal for all three samples. It has been difficult to synthesis samples with equally high density at all sintering temperatures, resulting in lower density for the samples sintered at 1300°C. The low density could thus explain the low permittivity associated with these samples. The density of SBN40 sintered at 1350°C and 1400°C is however almost the same, and the density argument could thus not be used for the difference in permittivity between these two samples.

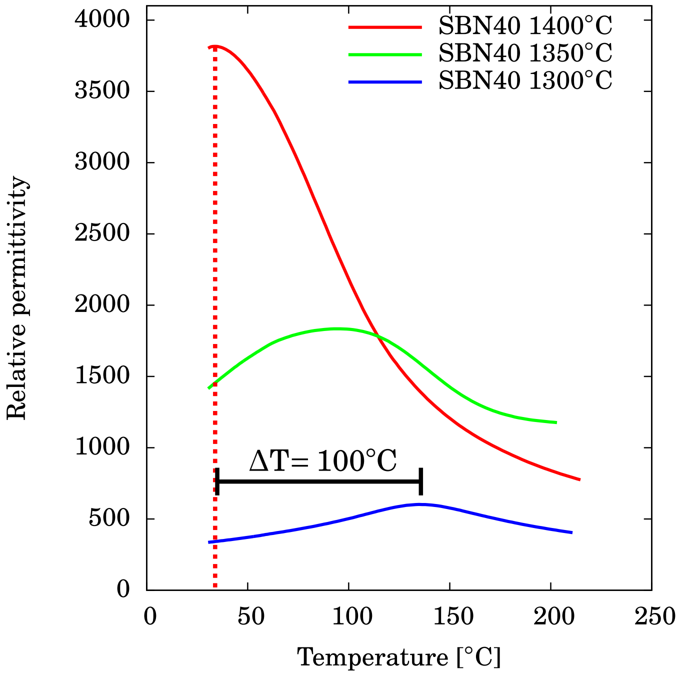

Figure 5.2: Dielectric permittivity for SBN40 sintered at 1300°C, 1350°C and 1400°C. The values are the real permittivity measured with a frequency of 10^2 Hz. A heating/cooling rate of $2° \min^{-1}$ combined with dielectric recordings every 30 seconds yielded results with very good resolution. The observed difference in peak position between the samples sintered at 1300°C and 1400°C is indicated with a bar.

5.2.2 Thermally induced relaxor behavior

The dielectric response of SBN40 sintered at 1300°C is presented in Figure 4.10. The figure shows the dielectric permittivity and dielectric loss recorded for a range of frequencies. There is no pronounced dispersion of dielectric response for the various frequencies. For temperatures higher than the peak's location all are curves overlapping, while there is some dispersion for lower temperatures. The sample behaves as a normal ferroelectric material, in accordance with Lukasiewicz' [20] results presented in Figure 2.6. The only deviation is the peak shape, which for a first order transition should be sharp and distinct [20]. The flattening of the peak could be a result of the lower density of the samples sintered at 1300°C. As the sintering temperature is increased the frequency independent behavior is lost. The dielectric response for SBN40 sintered at 1350°C and 1400°C is presented in Figures 4.11 and 4.12. The dielectric response for the various frequencies are now clearly dispersed, both with respect to peak position and measured permittivity. The dielectric permittivity is decreasing as the frequency increases, while the peak position is moving towards higher temperatures. This frequency dependent behavior is characteristic for relaxor materials [18, 49]. The transition from normal ferroelectric to relaxor behavior is for SBN reported to occur around 60% strontium content [20]. Above this limit the relaxor properties occur. All investigated compositions in the present work are below this limit and are thus expected to behave as normal ferroelectrics. The results indicate that the increased sintering temperature has caused a transition from normal ferroelectric to relaxor behavior. SBN50 sintered 1300, 1350°C and 1400°C is presented in Figures 4.13 to 4.15. The sample sintered at 1300°C show no frequential dispersion, and the peak in dielectric permittivity corresponds to the reported data for the Curie temperature. The samples sintered at 1350°C and 1400°C show a clear dispersion in permittivity both with respect to measured value and peak position. The same transition from normal ferroelectric to relaxor behavior is thus observed for SBN50.

A prerequisite for relaxor behavior is the ability for multiple cations to accommodate the same interstitial site in the crystal structure and thus causing structural disorder. The reported transition from normal ferroelectric to relaxor behavior is caused by increased strontium content [20]. As the strontium content increases, the structural disorder increases along with it. A sample with 20% strontium would, according to the literature, have all A2 sites filled up with barium, and strontium distributed at the A1 sites along with a vacancy. It would be no room for multiple cations at either of the sites in the structure, and the only disorder would be introduced by the strontium and vacancy at the A1 sites. As the strontium content increases, the barium to strontium ratio at the A2 sites is reduced. This would cause the overall disorder in the structure to increase, and at some point become high enough for the structure to adopt relaxor behavior. The transition is thus a result of increased disorder in the structure, usually induced by increased strontium content. In the present work, a similar transition from normal ferroelectric to relaxor behavior is observed. However, not caused by increased strontium content, but as a function of increasing sintering temperature. Structural disorder is still needed for relaxor behavior to occur, implying that increased sintering temperature has introduced increased disorder in the structure.

5.2.3 Temperature dependency of crystal structure

Unit cell measurements from SBN30 sintered at 1300°C and 1350°C are presented in Figures 4.16 and 4.17. The c parameter presented in Figure 4.16 show the characteristic behavior related to the loss of polarization at the phase transition temperature. Both sets of parameters indicate a phase transition temperature around 160-180°C, corresponding to the reported phase transition temperature for SBN30. Below 100°C, the c parameter related to the sample sintered at 1350°C flattens out at a lower value compared to the 1300°C sample. The increase in sintering temperature has decreased the value of the c parameter. This is in accordance with the unit cell parameters' temperature dependence discussed earlier. During the phase transition, there is a small shift in the c parameters of the two samples. The c parameter related to the sample sintered at 1350°C is shifted towards lower temperatures compared to the 1300°C sample. This could indicate a shift in phase transition temperature towards lower temperatures, which is in accordance with the dielectric measurements. The crystallographic response observed from the HT-XRD experiments is however not as pronounced as the dielectric response discussed earlier. It is difficult to explain why the shift of 100°C observed by dielectric spectroscopy is not observed to the same degree in the crystallographic response. As discussed earlier, the phase transition becomes more diffuse as the sintering temperature increases. The peak in permittivity is normally regarded as the temperature where the phase transition occurs. SBN below 60% strontium content is reported to undergo a first order transition [36]. As the sintering temperature increases, the phase transition becomes more diffuse and the resemblance to a first order transition becomes less clear. Hence, the correlation between the peak position and the phase transition temperature is also less clear. The increasing diffusivity of the phase transition could have different effect on the crystallographic and dielectric response, being a possible explanation for the different observations.

Unit cell values for SBN30, SBN40 and SBN50 are presented together with literature data in Figures 4.18 and 4.19. The sets of a parameters are increasing almost linearly with the decrease in strontium content. As the strontium content increases, the increase in c parameter is however decreasing in accordance with the deviation from Vegard's law. The reported phase transition temperatures are indicated by the dotted line for each composition in Figure 4.19. The decrease in c parameter upon increasing temperature, indicating where the actual phase transition occurs, coincides with the reported temperature.

The samples used in these investigations are as expected both with respect to absolute value, and temperature and composition dependent behavior. The high-temperature X-ray experiments can thus be used to strengthen the reliability of the other measurements conducted during the present work.

Chapter 6

Concluding remarks and further work

The purpose of this work has been to investigate how functional properties change with variations in thermal treatment. Samples of SBN with various compositions has been heat treated at various temperatures and characterized with X-ray diffraction and dielectric spectroscopy. Both the dielectric properties and the crystal structure have shown clear dependencies of the sintering temperature. Significant changes in X-ray diffraction patterns and crystal structure have been observed down to temperature differences as small as 50°C. According to the literature, all investigated samples should possess normal ferroelectric behavior. A transition from normal ferroelectric to relaxor behavior has however been induced by increasing sintering temperature. The unit cell has also shown a clear dependency of the thermal history. The c parameter is decreasing and the a parameter is increasing with increasing sintering temperature. The unit cell volume is decreasing as the sintering temperature is increasing.

The occupation of strontium and barium at the A1 and A2 sites has not been accurately determined during the present work. Since the structural disorder seemingly is increasing with the sintering temperature, it would be interesting to determine this dependency to a greater detail. A more detailed Rietveld analysis with focus on the cation occupancy over a larger range of temperatures could thus conducted. The temperature dependency of the dielectric response is very evident from the results presented in this work. This dependency should further be studied with respect to sintering temperature and sample composition. The dielectric and crystallographic response caused by the increase in sintering temperature are however not equal in magnitude. The dielectric response to the increased sintering temperature is measured to be much larger compared to the crystallographic response. Further investigations on the phase transition would be interesting to in order to determine the reason for the significantly difference in response.

Bibliography

[1] T. Brandvik. *Ferroelectric oxides with tetragonal tungsten bronze structure*. Spesialization project, Norwegian University of Science and Technology, 2014.

[2] T. Takenaka and H. Nagata. Current status and prospects of lead-free piezoelectric ceramics. *J. Eur. Ceram. Soc.*, 25(12):2693–2700, January 2005.

[3] E. Ringgaard and T. Wurlitzer. Lead-free piezoceramics based on alkali niobates. *J. Eur. Ceram. Soc.*, 25(12):2701–2706, January 2005.

[4] G. H. Haertling. Ferroelectric Ceramics: History and Technology. *J. Am. Ceram. Soc.*, 82(4):797–818, 1999.

[5] P. B. Jamieson. Ferroelectric Tungsten Bronze-Type Crystal Structures. I. Barium Strontium Niobate $Ba_{0.27}Sr_{0.75}Nb_2O_{5.78}$. *J. Chem. Phys.*, 48(11):5048, 1968.

[6] G. A. Rakuljic and A. Yariv. Photorefractive properties of undoped, cerium-doped and iron-doped single-crystal $Sr_{0.4}Ba_{0.6}Nb_2O_6$. *Opt. Eng.*, 25(11):1212–1216, 1986.

[7] C. David, T. Granzow, A. Tunyagi, M. Wöhlecke, T. Woike, K. Betzler, M. Ulex, M. Imlau, and R. Pankrath. Composition dependence of the phase transition temperature in $Sr_xBa_{1-x}Nb_2O_6$. *Phys. Status Solidi A*, 201(8):R49–R52, June 2004.

[8] J. R. Carruthers and M. Grasso. Phase Equilibria Relations in the Ternary System BaO-SrO-Nb_2O. *J. Electrchem. Soc.*, 518(1968):1426–1430, 1970.

[9] Q. Huang, P. Wang, Y. Cheng, and D. Yan. XRD analysis of formation of strontium barium niobate phase. *Mater. Lett.*, 56(6):915–920, 2002.

[10] G. H. Olsen, S. M. Selbach, and T. Grande. On the energetics of cation ordering in tungsten-bronze-type oxides. *To be published*.

[11] P. Labbe. Tungsten oxides, tungsten bronzes and tungsten bronze-type structures. *Key Eng. Mat.*, 68:293–339, 1992.

[12] Richard J.D. Tilley. *Understanding Solids*. Wiley & Sons, 2nd edition, 2013.

[13] A. R. West. *Basic Solid State Chemistry*. John Wiley & Sons, 1999.

[14] M. E. Lines and A. M. Glass. *Principles and applications of ferroelectrics and related materials*. 1977.

[15] V. V. Shvartsman and D. C. Lupascu. Lead-Free Relaxor Ferroelectrics. *J. Am. Ceram. Soc.*, 95(1):1–26, January 2012.

[16] R. A. Cowley, S. N. Gvasaliya, S. G. Lushnikov, B. Roessli, and G. M. Rotaru. Relaxing with relaxors: A review of relaxor ferroelectrics. *Adv. Phys.*, 60(2):229–327, April 2011.

[17] V. V. Shvartsman, J. Dec, S. Miga, T. Lukasiewicz, and W. Kleemann. Ferroelectric Domains in $Sr_{1-x}Ba_xNb_2O_6$ Single Crystals ($0.4 \leq x \leq 0.75$). *Ferroelectrics*, 376(1):1–8, 2008.

[18] A. A. Bokov and Z. G. Ye. Recent progress in relaxor ferroelectrics with perovskite structure. *J. Mater. Sci.*, 41(1):31–52, 2006.

[19] V. Hornebecq, C. Elissalde, F. Weill, A. Villesuzanne, M. Menetrier, and J. Ravez. Study of disorder in a tetragonal tungsten bronze ferroelectric relaxor: A structural approach. *J. Appl. Crystallogr.*, 33(4):1037–1045, 2000.

[20] T. Lukasiewicz, M. A. Swirkowicz, J. Dec, W. Hofman, and W. Szyrski. Strontium-barium niobate single crystals, growth and ferroelectric properties. *J. Cryst. Growth*, 310(7-9):1464–1469, April 2008.

[21] G. Burns and F. H. Dacol. Glassy polarization behavior in ferroelectric compounds $Pb(Mg_{0.33}Nb_{0.67})O_3$ and $Pb(Zn_{0.33}Nb_{0.67})O_3$. *Solid State Commun.*, 48(10):853–856, 1983.

[22] M. Ulex, R. Pankrath, and K. Betzler. Growth of strontium barium niobate: The liquidus-solidus phase diagram. *J. Cryst. Growth*, 271(1-2):128–133, October 2004.

[23] A. M. Glass. Investigation of the Electrical Properties of $Sr_{1-x}Ba_xNb_2O_6$ with Special Reference to Pyroelectric Detection. *J. Appl. Phys.*, 40(12):4699, 1969.

[24] S. Podlozhenov, H. A. Graetsch, J. Schneider, M. Ulex, M. Wöhlecke, and K. Betzler. Structure of strontium barium niobate $Sr_xBa_{1-x}Nb_2O_6$ (SBN) in the composition range $0.32 \leq x \leq 0.82$. *Acta Crystallogr. B.*, 62(6):960–965, December 2006.

[25] J. G. Carrio, Y. P. Mascarenhas, W. Yelon, I. A. Santos, D. Garcia, and J. A. Eiras. Structure Refinement of (Sr,Ba)Nb_2O_6 Ceramic Powder from Neutron and X-Rays Diffraction Data. *Mater. Res.*, 5(1):57–62, 2002.

[26] J. Schefer, D. Schaniel, V. Pomjakushin, U. Stuhr, V. Petricek, T. Woike, M. Wohlecke, and M. Imlau. Structural properties in $Sr_{0.61}Ba_{0.39}Nb_2O_6$ in the temperature range 10 K to 500 K investigated by high-resolution neutron powder diffraction and specific heat measurements. *Phys. Rev. B*, 74(13):1–9, 2006.

[27] T. Woike, V. Petricek, M. Dušek, N. K. Hansen, P. Fertey, C. Lecomte, A. Arakcheeva, G. Chapuis, M. Imlau, and R. Pankrath. The modulated structure of $Ba_{0.39}Sr_{0.61}Nb_2O_6$. I. Harmonic solution. *Acta Crystallogr. Sect. B Struct. Sci.*, 59(1):28–35, 2003.

[28] A. A. Ballman and H. Brown. The growth and properties of strontium barium metaniobate, $Sr_{1-x}Ba_xNb_2O_6$, a tungsten bronze ferroelectric. *J. Cryst. Growth*, 1(5):311–314, 1967.

[29] J. R. Oliver, R. R. Neurgaonkar, and L. E. Cross. A thermodynamic phenomenology for ferroelectric tungsten bronze $Sr_{0.6}Ba_{0.4}Nb_2O_6$ (SBN:60). *J. Appl. Phys.*, 64(1):37, 1988.

[30] C. Nikasch and M. Gobbels. Phase relations and lattice parameters in the system SrO-BaO-Nb_2O_5 focusing on SBN ($Sr_xBa_{1-x}Nb_2O_6$). *J. Cryst. Growth*, 269(2-4):324–332, September 2004.

[31] S. Aamlid. Rapport fra sommerprosjekt Syntese og karakterisering av $Sr_{1-x}Ba_xNb_2O_6$. Technical Report August, Department of Material Science, NTNU, 2014.

[32] A. R. Denton and N. W. Ashcroft. Vegard's Law. *Phys. Rev. A*, 43(6):3161–3164, 1991.

[33] L. Vegard. Die Konstitution der Mischkristalle und die Raumfüllung der Atome. *Zeitschrift für Phys.*, 5(1):17–26, 1921.

[34] G. Aylward and T. Findlay. *SI Chemical Data 6th edition*. John Wiley & Sons, Australia, 2008.

[35] H. A. Graetsch. Changes of the crystal structure at the relaxor ferroelectric phase transition of strontium barium niobate (SBN53). *Cryst. Res. Technol.*, 49(1):63–69, 2014.

[36] R. Guo, A. S. Bhalla, G. Burns, and F. H. Dacol. Studies on annealing and quenching of strontium barium niobate (SBN) single crystals: A-site cation ordering-disordering effect. *Ferroelectrics*, 93(1):397–405, 1989.

[37] X. Zhu, M. Fu, M. C. Stennett, P. M. Vilarinho, I. Levin, C. A. Randall, J. Gardner, F. D. Morrison, and I. M. Reaney. A Crystal-Chemical Framework for Relaxor versus Normal Ferroelectric Behavior in Tetragonal Tungsten Bronzes. *Chem. Mater.*, 27(9):3250–3261, 2015.

[38] P. B. Jamieson. Ferroelectric Tungsten Bronze-Type Crystal Structures. II. Barium Sodium Niobate $Ba_{4+x}Na_{2-2x}Nb_{10}O_{30}$. *J. Chem. Phys.*, 50(1969):4352, 1969.

[39] M. G. Sahini, T. Grande, B. Fraygola, A. Biancoli, D. Damjanovic, and N. Setter. Solid solutions of lead metaniobate-stabilization of the ferroelectric polymorph and the effect on the lattice parameters, dielectric, ferroelectric, and piezoelectric properties. *J. Am. Ceram. Soc.*, 97(1):220–227, 2014.

[40] G. H. Olsen, M. H. Sørby, B. C. Hauback, S. M. Selbach, and T. Grande. Revisiting the Crystal Structure of Rhombohedral Lead Metaniobate. *Inorg. Chem*, 53(18):9715–9721, 2014.

[41] H. S. C. O'Neill and A. Navrotsky. Binary Spinel Solid Solutions. *Am. Mineral.*, 69:733–753, 1984.

[42] K. Mocala and A. Navrotsky. Structural and thermodymnamic variations in nickel aluminate spinel. *J. Am. Ceram. Soc.*, 72(5):826–832, 1989.

[43] H. S. C. O'Neill, W. A. Dollase, and C. R. Ross. Temperature dependence of the cation distribution in nickel aluminate ($NiAl_2O_4$) spinel: a powder XRD study. *Phys. Chem. Miner.*, 18(5):302–319, 1991.

[44] H. S. C. O'Neill and A. Navrotsky. Simple spinels: crystallographic parameters, cation radii, lattice energies, and cation distribution. *Am. Mineral.*, 68(1-2):181–194, 1983.

[45] D. W. Richerson. *Modern Ceramic Engineering*. Taylor & Francis group CRC Press, 2005.

[46] G. W. Stinton and J. S. O. Evans. Parametric Rietveld refinement. *J. Appl. Crystallogr.*, 40(1):87–95, 2007.

[47] C. Kittel. *Introduction to Solid State Physics*. John Wiley & Sons, 2005.

[48] B. E. Warren. *X-ray Diffraction*. Courier Corporation, 1969.

[49] L. E. Cross. Relaxor ferroelectrics: An overview. *Ferroelectrics*, 151:305–320, 1994.

Appendix A

Constraints used during Rietveld refinements

A.1 Constraints used for SBN40

Table A.1: Constraints imposed on samples with 40% strontium by composition and point group symmetry. The values indicated in bold are kept constant during the refinement, while the linked positions is described by equations. The remaining values are subject for relaxation during the refinement.

Position	Atom	Mp.	x	y	z	Occ.	B_{iso}
A2	Ba	4	X_{A2}	$X_{\text{A2}}+0.5$	@	$0.75-0.5Occ_{\text{Ba,A1}}$	@
A2	Sr	4	X_{A2}	$X_{\text{A2}}+0.5$	@	$0.50-0.5Occ_{\text{Sr,A1}}$	@
A1	Sr	2	**0.0000**	**0.0000**	@	$Occ_{\text{Sr,A1}}$	@
A1	Ba	2	**0.0000**	**0.0000**	@	$Occ_{\text{Ba,A1}}$	@
Nb1	Nb	2	**0.5000**	**0.0000**	@	**1**	@
Nb2	Nb	8	@	@	@	**1**	@
O1	O1	4	X_{O1}	$X_{\text{O1}}+0.5$	@	**1**	**0.17**
O2	O2	8	@	@	@	**1**	**2.45**
O3	O3	8	@	@	@	**1**	**2.41**
O4	O4	8	@	@	@	**1**	**3.65**
O5	O5	2	**0.0000**	**0.5000**	@	**1**	**4.87**

A.2 Constraints used for SBN30

Table A.2: Constraints imposed on samples with 30% strontium by composition and point group symmetry. The values indicated in bold are kept constant during the refinement, while the linked positions is described by equations. The remaining values, marked with the *at* signs, are subject for relaxation during the refinement.

Position	Atom	Mp.	x	y	z	Occ.	B_{iso}
A2	Ba	4	X_{A2}	$X_{A2}+0.5$	@	$0.875-0.5Occ_{Ba,A1}$	@
A2	Sr	4	X_{A2}	$X_{A2}+0.5$	@	$0.375-0.5Occ_{Sr,A1}$	@
A1	Sr	2	**0.0000**	**0.0000**	@	$Occ_{Sr,A1}$	@
A1	Ba	2	**0.0000**	**0.0000**	@	$Occ_{Ba,A1}$	@
Nb1	Nb	2	**0.5000**	**0.0000**	@	**1**	@
Nb2	Nb	8	@	@	@	**1**	@
O1	O1	4	X_{O1}	$X_{O1}+0.5$	@	**1**	**0.17**
O2	O2	8	@	@	@	**1**	**2.45**
O3	O3	8	@	@	@	**1**	**2.41**
O4	O4	8	@	@	@	**1**	**3.65**
O5	O5	2	**0.0000**	**0.5000**	@	**1**	**4.87**

Appendix B

Crystal data from Rietveld refinements

B.1 SBN30 sintered at 1350°C

Table B.1: Structural data for SBN30 sintered at 1350°C found through Rietveld refinement in Topas.

Position	Atom	Mp.	x	y	z	Occ.	B_{iso}
A2	Ba	4	0.1724	0.6724	0.4524	0.8704	1.327
A2	Sr	4	0.1724	0.6724	0.4524	0.0349	1.183
A1	Sr	2	0	0	0.4943	0.6802	0.4477
A1	Ba	2	0	0	0.4943	0.0092	2.511
Nb1	Nb	2	0	0.5	0.9704	1	0.7032
Nb2	Nb	8	0.0738	0.2109	0.9689	1	0.6141
O1	O	4	0.2830	0.7830	0.0212	1	0.17
O2	O	8	0.1417	0.0668	0.9145	1	2.45
O3	O	8	0.3399	0.0055	0.9075	1	2.41
O4	O	8	0.2947	0.4272	0.4609	1	3.65
O5	O	2	0	0.5	0.4625	1	4.87

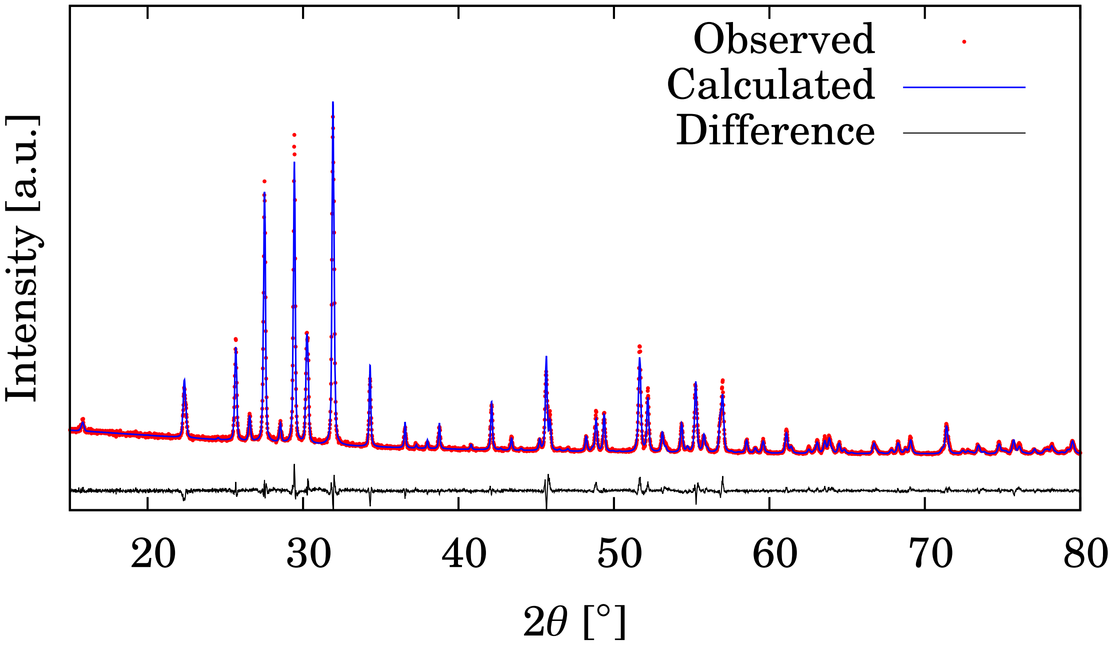

Figure B.1: Results from Rietveld refinement of SBN30 sintered at 1350°C. The calculated pattern was fitted to the observed diffractogram with a Rwp value of 9.353.

B.2 SBN30 sintered at 1400°C

Table B.2: Structural data for SBN30 sintered at 1400°C found through Rietveld refinement in Topas.

Position	Atom	Mp.	x	y	z	Occ.	B_{iso}
A2	Ba	4	0.1722	0.6722	0.4468	0.8749	1.047
A2	Sr	4	0.1722	0.6722	0.4468	0.0336	1.232
A1	Sr	2	0	0	0.4829	0.6829	0.2883
A1	Ba	2	0	0	0.4829	0.0001	3.657
Nb1	Nb	2	0	0.5	0.9833	1	0.5948
Nb2	Nb	8	0.0738	0.2107	0.9687	1	0.3119
O1	O	4	0.2832	0.7832	0.0259	1	0.17
O2	O	8	0.1411	0.0652	0.9091	1	2.45
O3	O	8	0.3413	0.0051	0.8929	1	2.41
O4	O	8	0.2947	0.4248	0.4721	1	3.65
O5	O	2	0	0.5	0.4781	1	4.87

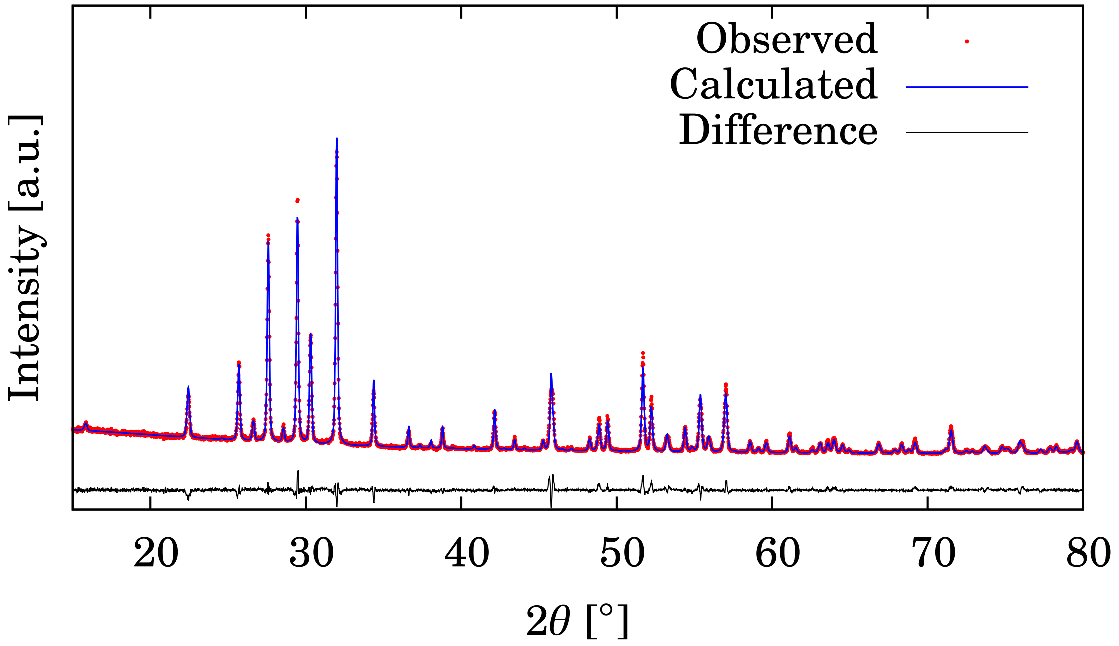

Figure B.2: Results from Rietveld refinement of SBN30 sintered at 1400°C. The calculated pattern was fitted to the observed diffractogram with a Rwp value of 9.455.

B.3 SBN40 sintered at 1300°C

Table B.3: Structural data for SBN40 sintered at 1300°C found through Rietveld refinement in Topas.

Position	Atom	Mp.	x	y	z	Occ.	B_{iso}
A2	Ba	4	0.1723	0.6723	0.4522	0.7500	1.642
A2	Sr	4	0.1723	0.6723	0.4522	0.1202	1.493
A1	Sr	2	0	0	0.4609	0.7596	1.058
A1	Ba	2	0	0	0.4609	0.0000	0
Nb1	Nb	2	0	0.5	0.9717	1	0.9221
Nb2	Nb	8	0.0742	0.2111	0.9720	1	0.7413
O1	O	4	0.2812	0.7812	0.0331	1	0.17
O2	O	8	0.1389	0.0664	0.9101	1	2.45
O3	O	8	0.3422	0.0034	0.8892	1	2.41
O4	O	8	0.2942	0.4249	0.4703	1	3.65
O5	O	2	0	0.5	0.4815	1	4.87

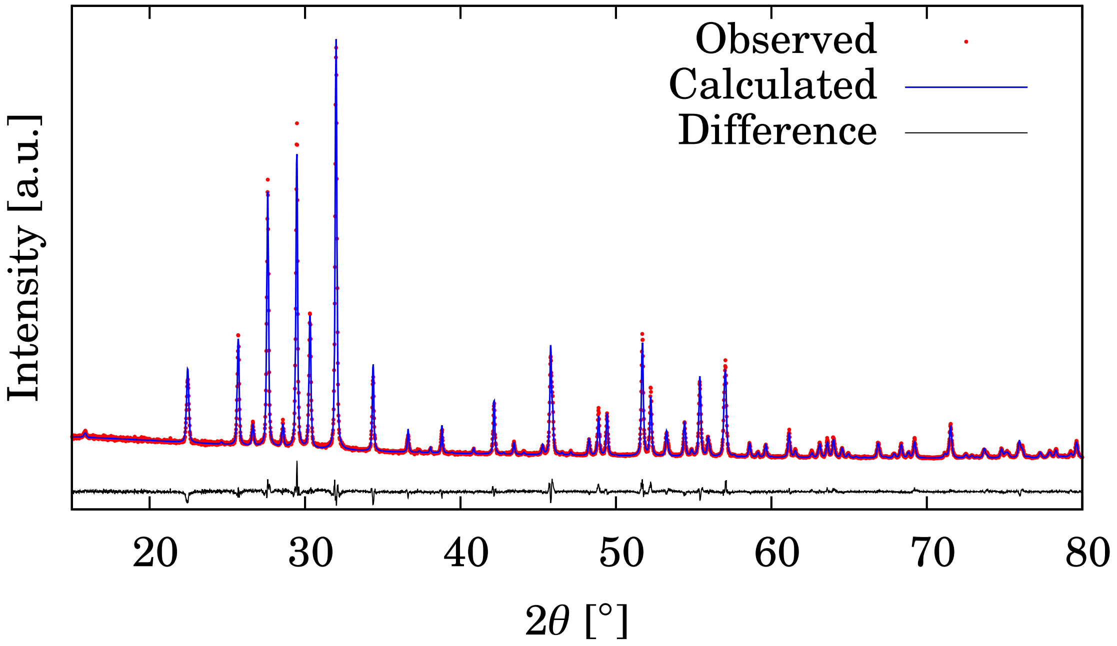

Figure B.3: Results from Rietveld refinement of SBN40 sintered at 1300°C. The calculated pattern was fitted to the observed diffractogram with a Rwp value of 8.417.

B.4 SBN40 sintered at 1350°C

Table B.4: Structural data for SBN40 sintered at 1350°C found through Rietveld refinement in Topas.

Position	Atom	Mp.	x	y	z	Occ.	B_{iso}
A2	Ba	4	0.1723	0.6723	0.4488	0.75	1.517
A2	Sr	4	0.1723	0.6723	0.4488	0.1213	1.689
A1	Sr	2	0	0	0.4554	0.7574	0.9287
A1	Ba	2	0	0	0.4554	0	1.5
Nb1	Nb	2	0	0.5	0.9752	1	0.7528
Nb2	Nb	8	0.0742	0.2110	0.9696	1	0.6765
O1	O	4	0.2801	0.7801	0.0235	1	0.17
O2	O	8	0.1405	0.0662	0.9096	1	2.45
O3	O	8	0.3417	0.0051	0.8878	1	2.41
O4	O	8	0.2944	0.4250	0.4693	1	3.65
O5	O	2	0	0.5	0.4858	1	4.87

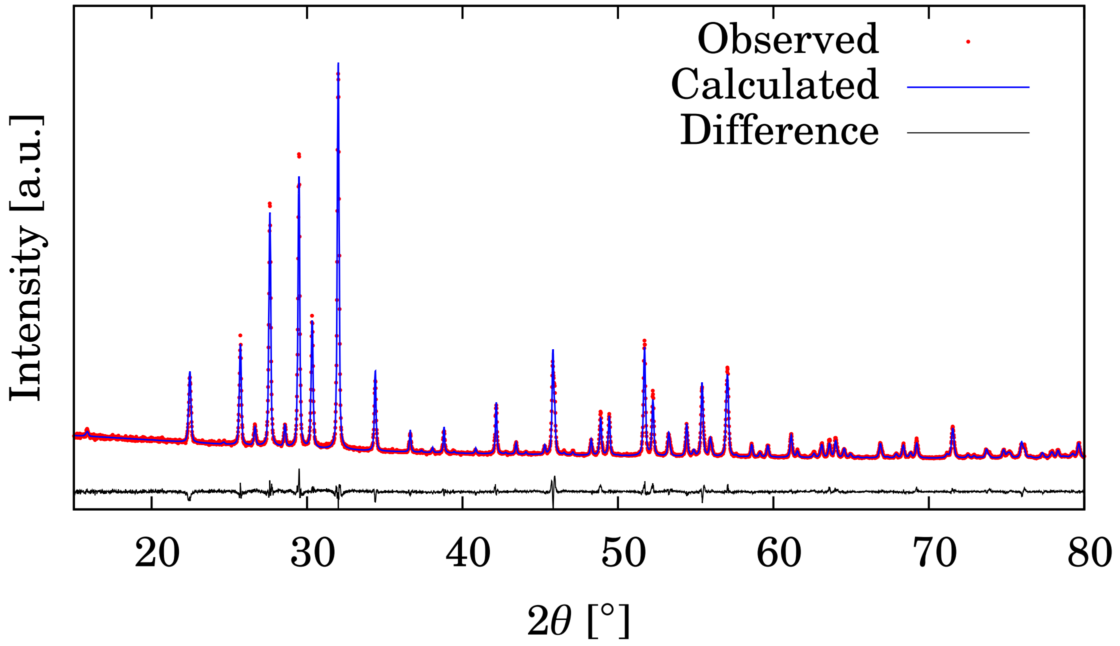

Figure B.4: Results from Rietveld refinement of SBN40 sintered at 1350°C. The calculated pattern was fitted to the observed diffractogram with a Rwp value of 8.461.

B.5 SBN40 sintered at 1400°C

Table B.5: Structural data for SBN40 sintered at 1400°C found through Rietveld refinement in Topas.

Position	Atom	Mp.	*x*	*y*	*z*	Occ.	B_{iso}
A2	Ba	4	0.1722	0.6722	0.4434	0.7072	0.9992
A2	Sr	4	0.1722	0.6722	0.4434	0.1788	1.127
A1	Sr	2	0	0	0.4723	0.6424	0.6278
A1	Ba	2	0	0	0.4723	0.0856	0.8467
Nb1	Nb	2	0	0.5	0.9679	1	0.3707
Nb2	Nb	8	0.0739	0.2112	0.9683	1	0.1810
O1	O	4	0.2811	0.7811	0.0226	1	0.17
O2	O	8	0.1385	0.0651	0.9047	1	2.45
O3	O	8	0.3411	0.0035	0.8921	1	2.41
O4	O	8	0.2966	0.4238	0.4706	1	3.65
O5	O	2	0	0.5	0.4794	1	4.87

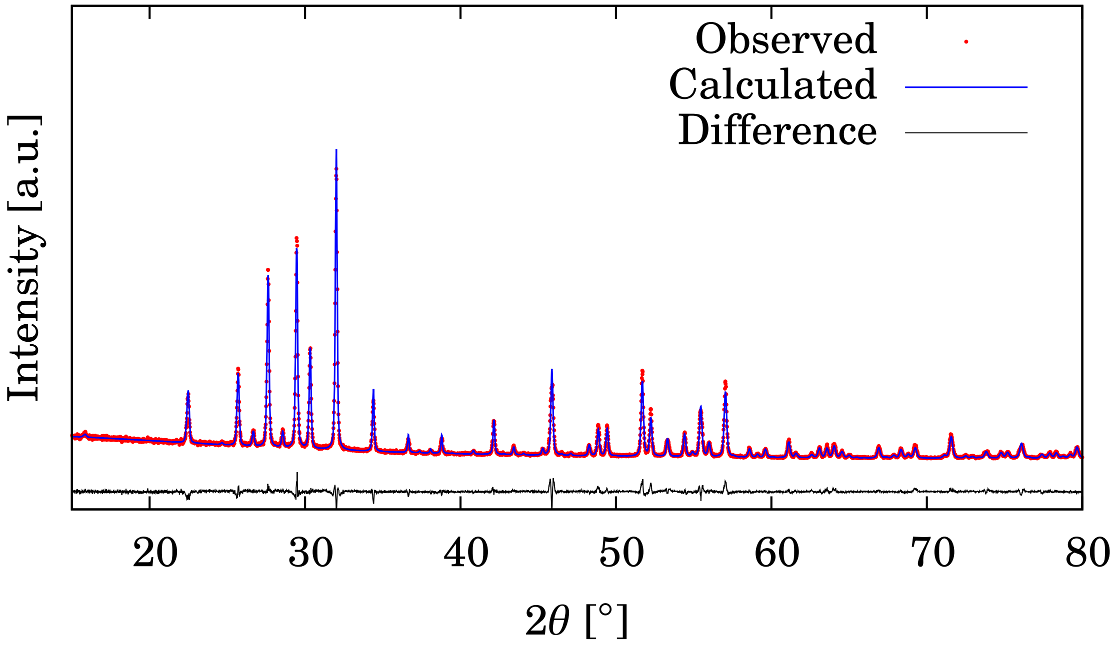

Figure B.5: Results from Rietveld refinement of SBN40 sintered at 1400°C. The calculated pattern was fitted to the observed diffractogram with a Rwp value of 9.272.

B.6 SBN50 sintered at 1300°C

Table B.6: Structural data for SBN50 sintered at 1300°C found through Rietveld refinement in Topas.

Position	Atom	Mp.	x	y	z	Occ.	B_{iso}
A2	Ba	4	0.1729	0.6729	0.4536	0.625	2.623
A2	Sr	4	0.1729	0.6729	0.4536	0.2310	2.467
A1	Sr	2	0	0	0.4454	0.7880	2.322
A1	Ba	2	0	0	0.4454	0	1.626
Nb1	Nb	2	0.5	0	0.9798	1	2.098
Nb2	Nb	8	0.0739	0.2119	0.9746	1	1.701
O1	O	4	0.2779	0.7779	0.0030	1	0.17
O2	O	8	0.1429	0.0680	0.8946	1	2.45
O3	O	8	0.3444	0.0084	0.8570	1	2.41
O4	O	8	0.2936	0.4195	0.4835	1	3.65
O5	O	2	0	0.5	0.5111	1	4.87

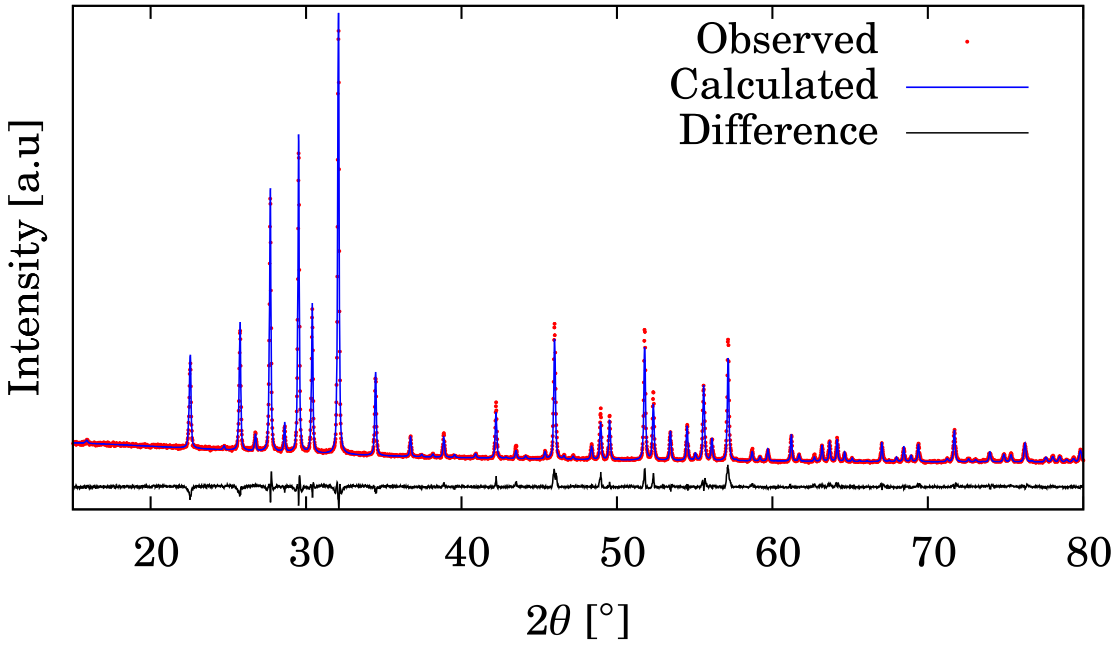

Figure B.6: Results from Rietveld refinement of SBN50 sintered at 1300°C. The calculated pattern was fitted to the observed diffractogram with a Rwp value of 8.482.

B.7 SBN50 sintered at 1400°C

Table B.7: Structural data for SBN50 sintered at 1400°C found through Rietveld refinement in Topas. The Mp. column indicates the multiplicity of the sites.

Position	Atom	Mp.	x	y	z	Occ.	B_{iso}
A2	Ba	4	0.1724	0.6724	0.4567	0.625	2.112
A2	Sr	4	0.1724	0.6724	0.4567	0.2148	1.952
A1	Sr	2	0	0	0.4559	0.8204	2.388
A1	Ba	2	0	0	0.4559	0	1.626
Nb1	Nb	2	0	0.5	0.9740	1	1.745
Nb2	Nb	8	0.0740	0.2119	0.9752	1	1.176
O1	O	4	0.2773	0.7773	0.0366	1	0.17
O2	O	8	0.1417	0.0674	0.8961	1	2.45
O3	O	8	0.3450	0.0071	0.8765	1	2.41
O4	O	8	0.2948	0.4179	0.4668	1	3.65
O5	O	2	0	0.5	0.4806	1	4.87

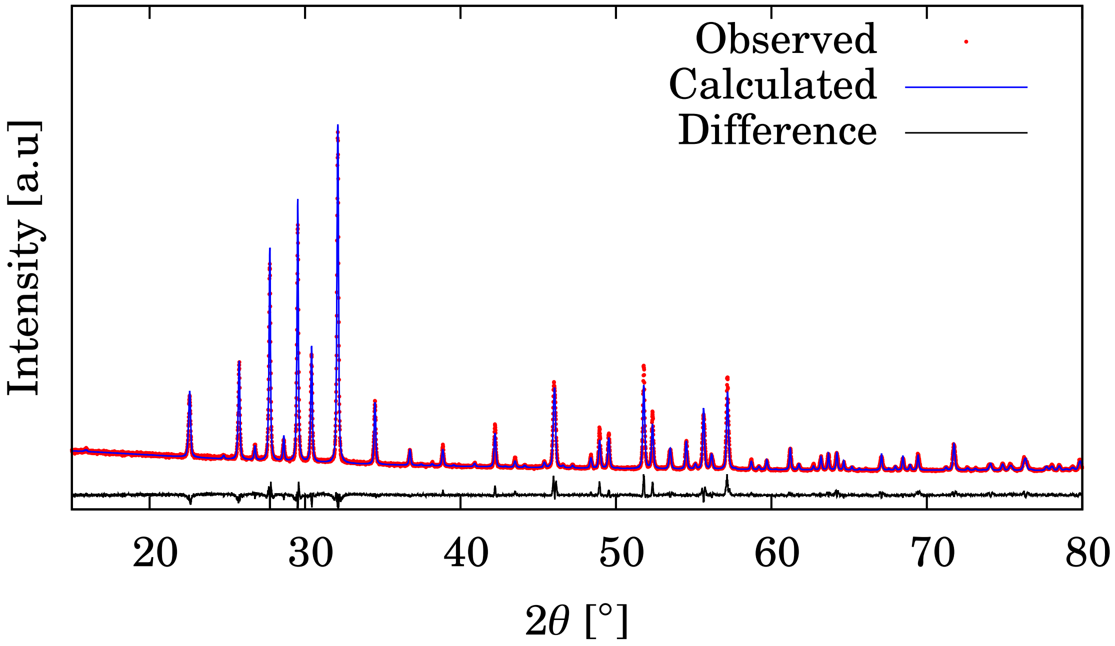

Figure B.7: Results from Rietveld refinement of SBN50 sintered at 1400°C. The calculated pattern was fitted to the observed diffractogram with a Rwp value of 8.889.

Appendix C

Temperature calibration

Two experiments were performed with high-temperature X-ray diffraction. A temperature calibration was conducted for prior to both experiments. The results of the temperature calibrations are presented in Tables C.1 and C.2.

Table C.1: Set temperatures, measured temperatures and the corresponding offset for the first HT-XRD experiment. The Offset decreases linearly as the set temperature increases, and reaches zero at 315°C.

Set temperature [°C]	Actual temperature [°C]	Offset [°C]
30	68	38
40	76	36
50	85	35
60	94	34
70	103	33
80	111	31
90	120	30
100	129	29
105	133	28
110	138	28
115	142	27
120	146	26
125	151	26
130	155	25
135	159	24
140	164	24
155	177	22
170	190	20
185	203	18
200	216	16
215	229	14

Table C.2: Set temperatures, measured temperatures and the corresponding offset for the second HT-XRD experiment.

Set temperature [°C]	Actual temperature [°C]	Offset [°C]
30	32	2
50	46	-4
70	60	-10
90	74	-16
110	88	-22
130	103	-27
145	114	-31
160	125	-35
175	137	-38
190	148	-42
205	160	-45
220	171	-49
240	187	-53
260	203	-57
280	219	-61
300	236	-64
320	253	-67
340	270	-70
360	287	-73
380	304	-76
400	322	-78
420	339	-81
440	357	-83